Entropy Removal and Coherence with Lasers

by

Jarrod Reilly

A thesis submitted to the Faculty of the
University of Colorado in partial fulfillment
of the requirements for the degree of
Bachelor of Arts
Department of Physics
2020

This thesis entitled:
Entropy Removal and Coherence with Lasers
written by Jarrod Reilly
has been approved for the Department of Physics

Murray Holland

Prof. Jun Ye

Prof. Magdalena Czubak

Date

The final copy of this thesis has been examined by the signatories, and we find that both the content and the form meet acceptable presentation standards of scholarly work in the above mentioned discipline.

Reilly, Jarrod (B.A., Physics)

Entropy Removal and Coherence with Lasers

Thesis directed by Prof. Murray Holland

The creation of low entropy states is crucial to modern atomic and molecular physics as particle cooling has opened the way for the creation of ultracold superfluid, quantum simulators, and increasing the precision of atomic clocks. However, it is often unclear how the particle ensemble's entropy is redistributed to other subsystems during the cooling process. Furthermore, experimental control of quantum systems during its interaction with laser fields is often impaired by incoherent, spontaneous processes that may transfer particles to unwanted states.

With these points in mind, my honors thesis focuses on protocols that create low entropy states as well as schemes that increase coherent control in quantum evolution. First, we present a method for creating high impulse laser slowing protocols that mitigate the effects of incoherent jumps by evolving the system with an adiabatic shortcut. Once the particles are slowed, they are often cooled using laser fields. This is the process under investigation next as we demonstrate that the laser fields themselves can absorb atomic entropy during their coherent dynamics. We then dedicate our study to the steady-state superradiance model in the weak pumping regime. Here, we investigate the properties of the subradiant state and the appearance of an "enhancement threshold" where the subradiant state may be extracted for high atom numbers in an experimental setting. These states are insensitive to spontaneous emission and can therefore protect the evolution of a system during a quantum metrological process on atomic platforms.

Dedication

To Sandra Bichefsky.

Contents

Chapter

Appendix

Tables

Table

Figures

Figure

Chapter 1

Introduction and Motivation

The creation of ultra-low temperature particle ensembles through cooling techniques has been at the forefront of contemporary atomic and molecular physics since the 1970's. In such experiments, cooling occurs when phase space is compressed as the entropy of the ensemble is transferred to other subsytems of the universe. This entropy exchange is governed by the second law of thermodynamics, a law so fundamental in our current understanding of physics that Albert Einstein believed [69]:

> It is the only physical theory of universal content concerning which [he is] convinced that within the framework of the applicability of its basic concepts, it will never be overthrow.

However, the fact that only the total entropy of the universe must increase often makes it unclear how the entropy is redistributed during the cooling process. It is often assumed that this removal relies of the irreversibly of incoherent processes. Yet, the spontaneity of incoherent quantum jumps may lead to poor control in experimental settings, as well as the loss of particles to undesired states. Similar undesirable dynamics occurs in many techniques in the ever growing field of quantum metrology. Here, incoherent processes can severely impact the precision of measurements and therefore mitigate the enhancement achieved by the exploitation of quantum effects.

It is thus desirable to increase coherent control of the system under study to reduce the reliance and occurrence of spontaneous processes. In doing so, one may ask the question if the system preforming the coherent dynamics, typically a laser field, may also absorb some of the initial entropy in the particle ensemble during the cooling process. Furthermore, increased control over the system dynamics may open the pathway for metrological techniques that can sustain many-body systems for long periods of operation. In this spirit, we identify three major themes that we address throughout the duration of this thesis to advance the cooling of quantum states:

(1) Presenting novel techniques that minimize spontaneous events and instead rely to a greater extent on coherent dynamics,

(2) The creation of low entropy states through an ensemble's interaction with laser fields,

(3) Studying the transfer of entropy from an atomic gas to the laser fields during laser cooling.

In this thesis, we present our contributions to the study of coherent control in creating and maintaining quantum systems. We begin with an introduction to the interaction of a particle with a classical laser field in Chapter 2. In this, we will discuss the field of adiabatic shortcuts, where coherent dynamics can be achieved in prodigious evolution times. In Chapter 3, we exploit the advantages of adiabatic shortcuts to create a novel particle slowing protocol. This falls into the first theme as open dynamics with scattered photon counts on the order of unity may be achieved. We then turn our attention to the second and third themes in Chapter 4 as we directly study the exchange of entropy during a laser cooling gedanken experiment. Here, we find that the laser field can indeed remove entropy from the atomic gas during the cooling process. We present another proposal for creating low entropy quantum states in Chapter 5 using the model for steady-state superradiance. This again falls under the second theme. While a low-entropic system is the result of our investigation, this chapter is primarily motivated by the first theme as the procedure enhances population in subradiant states that are insensitive to spontaneous emission. These states are then extracted and may be used for quantum metrological purposes to mitigate the effects of incoherent processes. We conclude in Chapter 6 with a brief summary of our work.

Chapter 2

Atom-Laser Interaction Background

I begin with one of the crucial problems in theoretical quantum optics, describing the interaction of a two-level particle with a classical field. The applicability of the model extends much further than what we cover here, as it is also useful to describe phenomena ranging from qubits to Bragg diffraction to neutrino oscillations [70, 59, 54]. I narrow my focus in this thesis to its application to particle-laser interactions that results in population transfer from one internal electronic state to another. In particular, I first look at systems that have a decreased reliance on incoherent, irreversible spontaneous emission compared to traditional schemes that are ubiquitously employed throughout the state of the art. Therefore, the focus of this background chapter is the coherent dynamics resulting for a particle's interaction with a classical laser field which drives stimulated absorption and stimulated emission between internal states. I switch my analysis in Chapter 4 to a particle's interaction with a laser when the latter is also treated quantum mechanically. I follow this by considering an ensemble of N two-level particles in Chapter 5, where collective incoherent processes can emerge by way of symmetry properties and interatomic coherence [46, 133, 63].

First demonstrated in Einstein's seminal paper on the quantum theory of radiation [48], stimulated emission offers many advantages over the randomness of spontaneous emission in the field of laser slowing and cooling, as well as elsewhere. As we shall see in Chapter 3, time-ordering of stimulated emission and absorption events driven by counterpropagating lasers has the potential to generate very large forces without reliance on the relaxation of the particle to return to the ground state manifold, leading to a nearly coherent slowing scheme that has a small associated slowing distance. We study coherent dynamics in a somewhat deeper manner in Chapter 4, where we analyze entropy production in the laser fields during laser cooling. Before this, however, I offer background information on the coherent dynamics of a two-level particle interacting with a classical field.

I begin this chapter by presenting an introduction to the adiabatic approximation. This is followed by studying the approximation's application to a two-level particle dressed by a laser. We then show how these processes can be sped up using adiabatic shortcuts: processes that achieve the same dynamics as ideal, adiabatic dynamics, but in much less time. I present both the counterdiabatic driving and Lewis-Riesenfeld invaniant (LRI) shortcuts, the latter of which is used in the context of laser slowing in Chapter 3. This chapter exclusively studies coherent dynamics.

2.1 Adiabatic Approximation

In this section, I offer a brief description of the adiabatic approximation, following Sakurai's explanation in [121, Chapter 5, § 6]. This is the the foundation of adiabatic passage between internal states, as demonstrated in the next section. Assuming no degeneracy, the instantaneous energy eigenvalue equation,

$$\hat{H}(t)\left|n(t)\right\rangle = E_n(t)\left|n(t)\right\rangle, \tag{2.1}$$

implies that a general solution to the time-dependent Schrödinger equation,

$$i\hbar\partial_t\left|\Psi(t)\right\rangle = \hat{H}(t)\left|\Psi(t)\right\rangle, \tag{2.2}$$

can be written in the energy basis as

$$\left|\Psi(t)\right\rangle = \sum_n \left|\psi_n(t)\right\rangle = \sum_n c_n(t)e^{i\theta_n(t)}\left|n(t)\right\rangle, \tag{2.3}$$

where $\theta_n(t) = -\frac{1}{\hbar}\int_{t_0}^{t} E_n(t')dt'$. Plugging this into the Schrödinger equation and taking the inner product with $\langle m(t)|$, we find

$$\dot{c}_m(t) = -\sum_n e^{i\theta_n(t)-i\theta_m(t)}\left\langle m(t)\right|\frac{\partial}{\partial t}\left|n(t)\right\rangle. \tag{2.4}$$

By differentiating the instantaneous energy eigenvalue equation Eq. (2.1), we arrive at

$$\dot{c}_m(t) = -c_m(t)\left\langle m(t)|\partial_t m(t)\right\rangle - \sum_{n\neq m} c_n(t)e^{i(\theta_n(t)-\theta_m(t))}\frac{\left\langle m(t)\right|\partial_t\hat{H}\left|n(t)\right\rangle}{E_n - E_m}, \tag{2.5}$$

where the dot denotes a derivative with respect to time. It is clear that, for time-dependent Hamiltonians, the second term of Eq. (2.5) will cause mixing between the $|m(t)\rangle$ and $|n(t)\rangle$ states when $m \neq n$. By assuming

$$\frac{\left\langle m(t)\right|\partial_t\hat{H}\left|n(t)\right\rangle}{(E_n - E_m)} \ll \left\langle m(t)|\partial_t m(t)\right\rangle, \tag{2.6}$$

the adiabatic approximation removes this eigenstate mixing:

$$\dot{c}_m(t) \approx -c_m\left\langle m(t)|\partial_t m(t)\right\rangle. \tag{2.7}$$

Furthermore, it can be shown that the n^{th} state vector takes the form

$$\left|\psi_n(t)\right\rangle = e^{-\int_0^t\langle n(t')|\partial_t n(t')\rangle dt'}e^{i\theta_n(t)}\left|n(t)\right\rangle. \tag{2.8}$$

Thus, the adiabatic approximation Eq. (2.6) implies that a system can be driven in its instantaneous eigenstates, up to a phase, under the condition that the Hamiltonian changes gradually.

The adiabatic approximation has led to revolutionary discoveries such as Berry's phase [18] and the Aharonov-Bohm effect [5] which have changed our understanding of the quantum phase. I focus on its application to the time-dependent two-level particle Hamiltonian to derive a condition that defines a regime where eigenstate mixing is limited.

2.2 Two-Level Atom Hamiltonian

We now model a particle as a two-level system consisting of a single internal ground state and a single internal excited state separated by atomic frequency ω_a, as depicted in Fig. 2.1. An example of this system is the ${}^1S_0 \to {}^3P_1$ transition in ^{88}Sr. We investigate the Hamiltonian of a two-level particle driven by a classical field that is varying in time. The Hamiltonian, after the rotating-wave and dipole approximations, is given by

$$\hat{H} = \frac{\hbar\omega_a}{2}\left(|e\rangle\langle e| - |g\rangle\langle g|\right) + \frac{\hbar\Omega(t)}{2}\left(|g\rangle\langle e|\, e^{i\int_{t_0}^t\omega(t')dt'} + \mathrm{H.c.}\right), \tag{2.9}$$

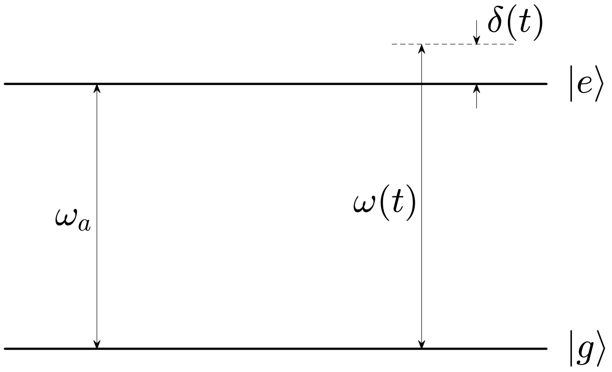

Figure 2.1: Frequency diagram of a two-level particle interacting with a classical field. The particle has two internal states $|e\rangle$ and $|g\rangle$ representing an excited state and long-lived ground state, respectively, separated by the transition frequency ω_a. The laser has time-dependent frequency $\omega(t)$ that is detuned from resonance by $\delta(t) = \omega(t) - \omega_a$.

where $\omega(t)$ is the laser's frequency, $\hbar$ is Planck's reduced constant with units $[\hbar] = \mathrm{J}\cdot\mathrm{s}$, H.c. stands for Hermitian conjugate, and I have defined $E = 0$ to be halfway between the electronic states. The laser's Rabi frequency $\mathit{\Omega}(t)$ is related to its intensity $\mathit{\Omega} \propto \sqrt{I}$ [see Eq.(3.49)] and given by Eq. (A.20). The first two outer products in Eq. (2.9) represent the bare energies of the internal states. The terms proportional to the Rabi frequency represent stimulated emission $|g\rangle\langle e|$ and stimulated absorption $|e\rangle\langle g|$ of a photon due to the particle's interaction with the laser field. The detailed derivation of Eq. (2.9) is provided in Appendix A.

We next move into a rotating frame by defining an interaction picture:

$$\hat{H}_0 = \frac{\hbar\omega(t)}{2}\left(|e\rangle\langle e| - |g\rangle\langle g|\right). \tag{2.10}$$

This gives, as shown in Appendix B.2,

$$\tilde{\hat{H}} = \frac{\hbar\delta(t)}{2}\left(|g\rangle\langle g| - |e\rangle\langle e|\right) + \frac{\hbar\mathit{\Omega}(t)}{2}\left(|g\rangle\langle e| + |e\rangle\langle g|\right), \tag{2.11}$$

where we have defined the time-dependent laser detuning $\delta(t) = \omega(t) - \omega_a$. Eq. (2.11) can be written in matrix form as

$$\tilde{\hat{H}} = \frac{\hbar}{2}\begin{pmatrix} -\delta(t) & \mathit{\Omega}(t) \\ \mathit{\Omega}(t) & \delta(t) \end{pmatrix}, \tag{2.12}$$

where $|g\rangle = \binom{0}{1}$ and $|e\rangle = \binom{1}{0}$ are the ground and excited states, respectively.

Due to the interaction with the classical field, the bare states $|g\rangle$ and $|e\rangle$ are no longer the eigenvectors of the system's Hamiltonian. We now find the new eigenstates that diagonalize Eq. (2.11). The instantaneous energy eigenvalues are proportional to the generalized Rabi frequency $\tilde{\mathit{\Omega}} = \sqrt{\delta^2 + \mathit{\Omega}^2}$:

$$E_\pm(t) = \pm\frac{\hbar\tilde{\mathit{\Omega}}(t)}{2}. \tag{2.13}$$

We note that

$$\tilde{\mathit{\Omega}}^2(t) = \delta^2(t) + \mathit{\Omega}^2(t) \longrightarrow 1 = \left(\frac{\delta(t)}{\tilde{\mathit{\Omega}}(t)}\right)^2 + \left(\frac{\mathit{\Omega}(t)}{\tilde{\mathit{\Omega}}(t)}\right)^2, \tag{2.14}$$

which motivates the definition of the Stückelberg angle,

$$\chi(t) \equiv \arccos\left(\frac{\delta(t)}{\tilde{\mathit{\Omega}}(t)}\right), \tag{2.15}$$

in deriving the system's instantaneous eigenvectors, named the dressed states [130]:

$$\begin{aligned} |+(t)\rangle &= \cos\left(\frac{\chi(t)}{2}\right)|e\rangle + \sin\left(\frac{\chi(t)}{2}\right)|g\rangle\,, \\ |-(t)\rangle &= \sin\left(\frac{\chi(t)}{2}\right)|e\rangle - \cos\left(\frac{\chi(t)}{2}\right)|g\rangle\,. \end{aligned} \tag{2.16}$$

We will see that the instantaneous eigenvectors of the system will give a good amount of insight on effectively transferring population between two electronic quantum states.

2.3 Rapid Adiabatic Passage

The goal of this section is to achieve population transfer between internal states via the particle's interaction with a classical field. The most basic way to achieve such a transfer between two quantum states is to apply a resonant ($\delta(t) = 0$) light pulse with an "area" of π, [1]

$$\int_{t_0}^{t_f} \Omega(t')dt' = \pi, \tag{2.17}$$

with initial and final times t_0 and t_f. While this Rabi-flopping "π-pulse" method, in theory, completely transfers population, it is not robust to small errors in Ω, the frequency ω of the light source, or coupling to other states outside of the two-level manifold. These are important considerations when the goal of the process is to transfer a wide distribution of momentum states, as is the goal consider in the next chapter.

To overcome these problems, one can instead chirp the laser frequency from well below resonance to well above resonance. We see from Eq. (2.16) that transfer from one bare state to the other can be accomplished by driving the particle in one of its dressed states, which Eq. (2.6) states is possible if the time-dependent perturbation applied to the system varies slowly, and changing $\chi(t)$ by π. The transfer between bare states becomes apparent in the avoided crossing depicted in Fig. 2.2, where a frequency gap in the eigenvalue spectrum causes an exchange of the uncoupled bare eigenstates. This process, when satisfying the adiabatic approximation, is called *adiabatic passage*.

---

[1] This is seen from Eq. (2.19), with $\delta(t) = 0$, by decoupling through differentiation and noting the normalization condition when solving the acquired second-order differential equations.

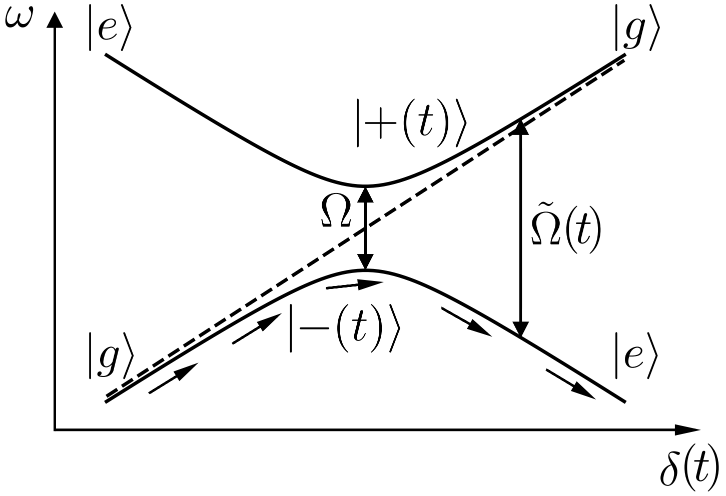

Figure 2.2: Eigenfrequency diagram for a linear sweep $\delta(t) = \alpha t$ and constant Rabi frequency Ω over resonance. The bare states ($|g\rangle$ and $|e\rangle$, dashed line) exchange identities in the dressed eigenstate ($|+\rangle, |-\rangle$, solid lines with parabolic shape) picture. Driving the system in the lower eigenstate is shown by the path of arrows. The eigenstates are split by the generalized Rabi frequency $\tilde{\Omega}(t)$ which becomes Ω at resonance. Therefore, eigenstate mixing decreases as Ω increases.

One can then ask how much population is lost if the frequency is swept too quickly so that Eq. (2.6) is not satisfied. This problem can be solved analytically, as first shown by Landau and Zener [153], and is often called the *Landau-Zener crossing problem.* Let us define the atomic state vector as $|\psi(t)\rangle = c_g(t)\,|g\rangle + c_e(t)\,|e\rangle$, where we note the normalization condition for the complex amplitudes of the state vector: $\sum_i |c_i|^2 = 1$. The time-dependent Schrödinger equation Eq. (2.2) using the Hamiltonian given in Eq. (2.11) then reads

$$i\hbar\left(\frac{\partial c_g}{\partial t}\,|g\rangle + \frac{\partial c_e}{\partial t}\,|e\rangle\right) = \frac{\hbar\delta(t)}{2}\left(c_g\,|g\rangle - c_e\,|e\rangle\right) + \frac{\hbar\Omega(t)}{2}\left(c_e\,|g\rangle + c_g\,|e\rangle\right). \tag{2.18}$$

Projecting with $\langle g|$ and $\langle e|$, the equations of motion of the bare state amplitudes are

$$\begin{aligned} \dot{c}_g &= -\frac{i\delta(t)}{2}c_g - \frac{i\Omega(t)}{2}c_e, \\ \dot{c}_e &= \frac{i\delta(t)}{2}c_e - \frac{i\Omega(t)}{2}c_g, \end{aligned} \tag{2.19}$$

which we can now solve for the atomic evolution by decoupling by differentiation. The resulting second-order equations take the form of Weber's equation,

$$\left(\partial_t^2 + \nu + \frac{1}{2} - \frac{z^2t^2}{4}\right) f = 0, \tag{2.20}$$

and can be solved analytically (see [130, Chapter 5, § 3]). The resulting Landau-Zener equation gives the probability of ending the sweep in the excited state, $P_e(t\to\infty) = |\langle e|\psi(t\to\infty)\rangle|^2$, for a given sweep slope. Assuming a real and constant Rabi frequency, as well as the particle beginning the sweep in the ground state, it is given by

$$P_e(t\to\infty) = |c_e|^2 = 1 - \exp\left(-\frac{\pi\Omega^2}{2\left|\dot{\delta}(t)\right|}\right) = 1 - \exp\left(-\frac{\pi\kappa}{2}\right). \tag{2.21}$$

Here, we have defined the adiabaticity parameter κ, and we see that the adiabatic approximation for transfer in the dressed states of the system is given by $\kappa \gg 1$. Eq. (2.21) demonstrates that in the regime of very large laser detuning slope, $\left|\dot{\delta}(t)\right| \gg \Omega^2$, the excited state population decreases substantially as a result of tunneling across the energy gap in Fig. 2.2. This causes the particle to end the sweep in the opposite dressed state, and thus the same bare state, in which it began the sweep as Eq. (2.6) is not satisfied. This is illustrated in Fig. 2.3 for a linear detuning sweep.

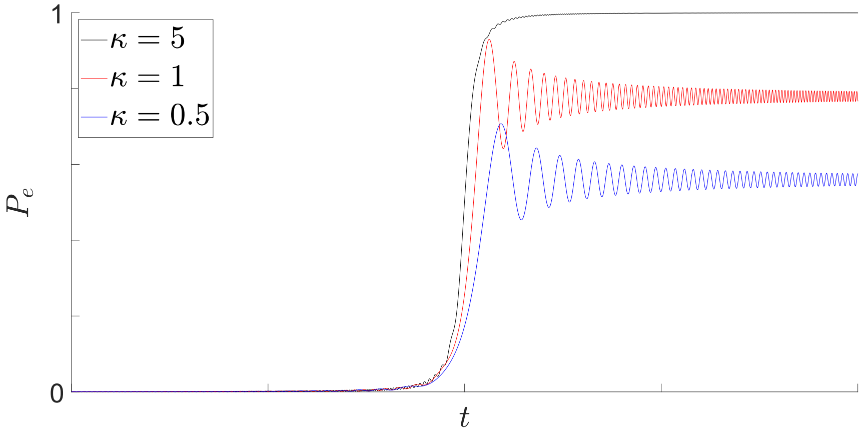

Figure 2.3: Stimulated evolution of the excited state population P_e for a linear sweep with constant Rabi frequency. Here, the final excited state populations for the 3 sweep rates are 0.9996 ($\kappa = 5$, black line), 0.7921 ($\kappa = 1$, red line), and 0.5441 ($\kappa = 0.5$,blue line). Numerical calculations employed the fouth-order Runge-Kutta integration method.

We have thus found a solution to stimulate absorption and emission with a classical laser field that is robust to many of the problems encountered when preforming π-pulses. We have so far omitted the incoherent effects of spontaneous emission that will cause the excited state to decay down to the ground state at the natural decay rate Γ of the atomic state. This omission is justified in a process called *rapid adiabatic passage* by requiring that the chirp must be fast compared to the decay rate of $|e\rangle$. Additionally, the field must be strong enough so that the dressed states are well resolved in the presence of the homogeneous broadening of the energy levels.

The velocity-independent feature of rapid adiabtic passage motivated the development of sawtooth-wave adiabatic passage (SWAP) cooling [108, 14, 62, 13, 127, 104], which coherently transfers a particle between quantum states via periodic Landau-Zener chirps in order to reduce the momentum of the system. However, the requirement to satisfy Eq. (2.6) may cause long evolution times and the process can be sensitive to the laser's phase. Furthermore, in the neighborhood of the atomic resonance, there are significant oscillations in the populations that result from the precession of the Bloch vector as it travels along the Bloch sphere [52, 147], which can complicate the amount of population transfer. As I shall show, an alternative scheme for coherent transfer by use of adiabatic shortcuts ameliorates the issues that have been described for π-pulses and adiabatic passage.

2.4 Adiabatic Shortcuts

Over the past decade, there has been a rapid development and growth of interest in *shortcuts to adiabaticity*. These are processes with the same outcome as ideal, infinitely long adiabatic processes, but in a much quicker time. A variety of techniques have been proposed and experimentally demonstrated: transitionless quantum driving [45, 19, 31, 16], inverse engineering based on Lewis-Riesenfeld invariants [80, 32, 31, 78, 33, 65], optimal control bang-bang type [146, 27, 12, 38], fast-forward techniques for Schrödinger [87, 88, 142] and Dirac dynamics [44], "environment" assisted methods [89], fast quasiadiabatic dynamics (FAQUAD) [85], and using the properties of Lie algebras [123, 86, 141, 112]. So far, these adiabatic shortcut techniques have been employed in frictionless cooling in harmonic traps [31], in Penning traps [38], in cavity quantum electrodynamics [33], in suppressing pair production [44], in atom interferometry [47], in implementing the Allen-Eberly scheme [31], in STIRAP demonstrations [31, 89, 81, 103], in quantum simulators [12, 11], in quantum computing [135], and even in quantum gaming [125]. A review of the growing shortcut research field is presented in [64]. In this section, we focus on shortcut techniques that employ inverse engineering. In Chapter 3, we demonstrate how coherent particle slowing processes can be sped up using adiabatic shortcuts.

2.4.1 Berry's Transitionless Quantum Driving Algorithm

The idea of counteradiabatic driving was first developed in the early 2000's [45], but grew in popularity significantly after it was rediscovered by Michael Berry in [19] and when it was applied to two- and three-level atoms in [30]. Berry called his procedure the transitionless quantum driving (TQD) algorithm and it is based on the idea of inverse engineering. Rather than finding the state of the system for a known time-dependent Hamiltonian, inverse engineering prescribes that the driving Hamiltonian is determined from the desired state evolution.

Our desired evolution is obtained, in ansatz to Eq. (2.8), by defining the unitary time-evolution operator $|\Psi(t)\rangle = \hat{U}(t)\,|\Psi(0)\rangle$ as [19]

$$\hat{U}(t) = \sum_n e^{-\int_0^t \langle n(t')|\partial_t n(t')\rangle dt'} e^{i\theta_n(t)}\,|n(t)\rangle\langle n(0)|\,. \tag{2.22}$$

It can be shown [93, Chapter 8, § 8] that the time-evolution operator satisfies

$$i\hbar\frac{\partial\hat{U}(t)}{\partial t} = \hat{H}(t)\hat{U}(t), \tag{2.23}$$

and the instantaneous Hamiltonian can therefore be written as

$$\hat{H}(t) = i\hbar\frac{\partial\hat{U}}{\partial t}\hat{U}^{\dagger}. \tag{2.24}$$

Plugging in Eq. (2.22), we find that the driving Hamiltonian can be written as

$$\hat{H}(t) = \hat{H}_0 + \hat{H}_1 = \hat{H}_0 + i\hbar\sum_{m\neq n}\sum\frac{|m(t)\rangle\langle m(t)|\,\partial_t\hat{H}_0\,|n(t)\rangle\langle n(t)|}{E_n - E_m}, \tag{2.25}$$

where $\hat{H}_0 = \sum_n E_n(t)\, |n(t)\rangle\langle n(t)|$ is the original Hamiltonian in its instantaneous eigenbasis. Note the similarity of the counteradiabatic term $\hat{H}_1$ to Eq. (2.5). Performing the unitary transformation on the initial state ket $|\psi(0)\rangle$, we find the state evolution is

$$|\psi(t)\rangle = \hat{U}(t)\, |\psi(0)\rangle = \sum_n c_n(0) e^{-\int_0^t \langle n(t')|\partial_t n(t')\rangle dt'} e^{i\theta_n(t)}\, |n(t)\rangle \, . \tag{2.26}$$

Thus, the system will now be driven exactly in the instantaneous eigenstates with no state mixing, as the adiabatic approximation becomes exact [see Eq. (2.8)]. In other words, we have found a nearby Hamiltonian with the property that the transition amplitudes between any eigenstates of the original Hamiltonian are exactly zero for any speed.

The simplest counterdiabatic Hamiltonian is given by

$$\hat{H}_1 = i\hbar \sum_n |\partial_t n\rangle\langle n| \, . \tag{2.27}$$

For the Landau-Zener scheme with a linear detuning, $\delta(t) = \alpha t + t_0$, and constant Rabi frequency $\Omega(t) = \Omega$, this gives [64]

$$\hat{H}_1 = \frac{\hbar}{2} \begin{pmatrix} 0 & -i\Omega'(t) \\ i\Omega'(t) & 0 \end{pmatrix} , \tag{2.28}$$

where $\Omega'(t) = \dot{\delta}(t)\Omega/\tilde{\Omega}^2(t)$. Noting that $\dot{\delta}(t)$ is a constant, we see that $\Omega'(t)$ has a Lorentzian profile. Taking the same physical interpretation of the counterdiabatic term presented in [30], we see that $\hat{H}_1$ amounts to adding a second laser 90° out of phase from the first (note $i = \exp[i\pi/2]$) with a Lorentzian Rabi frequency profile. This extra laser will exactly cancel out any eigenstate mixing that would take place.

While this is the simplest counteradiabatic Hamiltonian, an infinate number of driving Hamiltonians are possible (see [16], for example). A nearby solution is given by a Gaussian Rabi frequency profile on the auxiliary laser,

$$\Omega'(t) = \mu\Omega \exp\left[\frac{t^2}{2\tau^2}\right] , \tag{2.29}$$

where I have set $t_0 = -t_f$, $\delta(0) = 0$, defined the dimensionless parameter μ, and defined the parameter τ with dimensions of time. To visualize the speed up of the adiabatic process, I take advantage of the pseudo-spin $\frac{1}{2}$ nature of the system to examine the dynamics on the Bloch sphere in the so-called Feynman-Vernon-Hellwarth representation [52]. Assuming a pure state, the density operator $\hat{\rho}$ is given by

$$\hat{\rho}(t) = |\psi(t)\rangle\langle\psi(t)| = \begin{pmatrix} \rho_{ee} & \rho_{ge} \\ \rho_{eg} & \rho_{gg} \end{pmatrix}, \tag{2.30}$$

where $\rho_{ij} = \langle i|\,\hat{\rho}\,|j\rangle = c_i c_j^*$. Note the normalization condition now reads $\mathrm{Tr}[\hat{\rho}] = 1$, where $\mathrm{Tr}[\cdot]$ is the trace. We can map this to a 3D representation via the expectation values of the three Pauli matrices,

$$\begin{aligned} \langle\hat{\sigma}_x\rangle &= \langle\hat{\sigma}^-\rangle + \langle\hat{\sigma}^+\rangle = \rho_{eg} + \rho_{ge}, \\ \langle\hat{\sigma}_y\rangle &= i\langle\hat{\sigma}^-\rangle - i\langle\hat{\sigma}^+\rangle = i\rho_{eg} - i\rho_{ge}, \\ \langle\hat{\sigma}_z\rangle &= \langle\hat{\sigma}^+\hat{\sigma}\rangle^- - \langle\hat{\sigma}^-\hat{\sigma}^+\rangle = \rho_{ee} - \rho_{gg}, \end{aligned} \tag{2.31}$$

where $\hat{\sigma}^- = |g\rangle\langle e|$ ($\hat{\sigma}^+ = |e\rangle\langle g|$) is the lowering (raising) operator and we have used the cyclic property of the trace in the expectation value equation [121, Chapter 3, §4]

$$\langle\hat{A}\rangle = \mathrm{Tr}\left[\hat{A}\hat{\rho}\right]. \tag{2.32}$$

The Bloch vector

$$\langle\boldsymbol{\sigma}\rangle = \langle\hat{\sigma}_x\rangle\hat{\boldsymbol{\imath}} + \langle\hat{\sigma}_y\rangle\hat{\boldsymbol{\jmath}} + \langle\hat{\sigma}_z\rangle\hat{\boldsymbol{k}}, \tag{2.33}$$

is plotted in Fig. 2.4 for the adiabatic process, as well as for shortcuts to adiabatic passage (SHAPE) with the Lorentzian and Gaussian schemes. We can see from Eq. (2.31) that the south pole of the Bloch sphere corresponds to an unexcited particle, while the north pole is a completely excited particle. Fig. 2.4 demonstrates that, for a particular value of κ, the adiabatic process has significant loss [$P_e(t \to \infty) \approx 0.8$], but both shortcut schemes reach the north pole along two different, but nearby, paths on the Bloch sphere.

While the transitionless quantum driving algorithm drives the system perfectly in the dressed states of the system, the question that arises is about a trade-off between speed and energetic resources for applying the shortcut. In other words, at what value of κ does the amount of auxiliary laser power needed to drive the system via TQD become so great that simply increasing the original

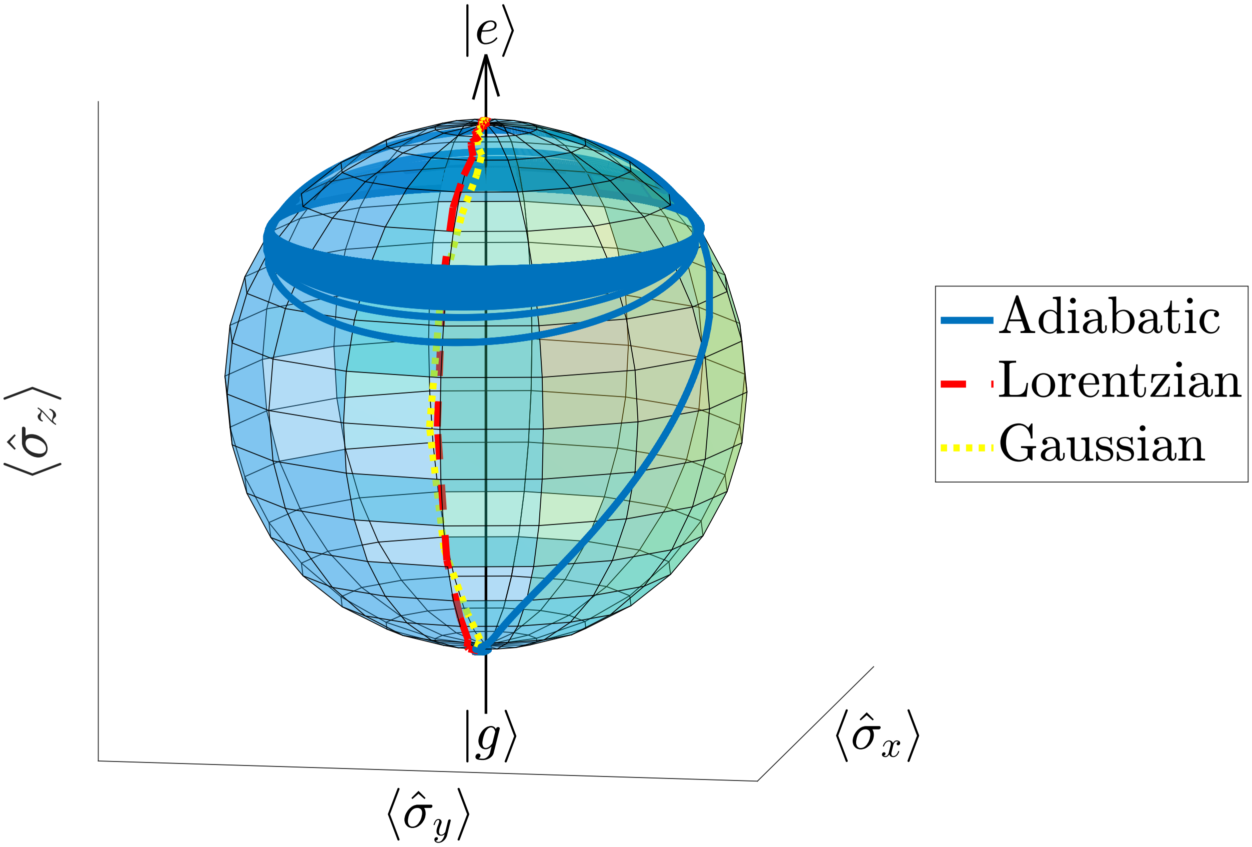

Figure 2.4: Path of the Bloch vector (thick curves) in the laser's rotating frame for regular adiabatic passage (blue, solid curve), SHAPE with a Lorentzian profile (red, dashed curve), and SHAPE with a Gaussian profile (yellow, dotted curve) with parameters $\mu = 0.8761$ and $\tau = \frac{1}{\Omega}$. Here, $\kappa = 1$ and thus, the adiabatic condition is not satisfied.

laser power by that amount would satisfy that new adiabatic condition? The concept of an energetic cost for implementing adiabatic shortcuts and the intrinsic relationship between this cost and shortcut speed has been rigorously studied for Berry's TQD algorithm [26], various other shortcuts [1], and in its applications to quantum computing [41]. The study of multiple shortcuts in [1] suggests that counteradiabatic driving schemes (such as TQD) are, in general, more energetically costly than other shortcut protocols such as the bang-bang shortcut and inverse engineering based on Lewis-Riesenfeld invariant theory. This motivates the use of the latter as the shortcut protocol to speed up particle slowing. I will now briefly introduce the Lewis-Riesenfeld invariant shortcut protocol, followed by its application to particle slowing in Chapter 3. More on this concept of the energetic cost to implement a shortcut scheme will be discussed in Section 3.3.

2.4.2 Inverse Engineering Based on Lewis-Riesenfeld Invariants

The theory of Lewis-Riesenfeld invariants (LRI) was developed in the late 1960's to derive the solutions of the Schrödinger equation for explicitly time-dependent Hamiltonians [80]. Lewis and Riesenfeld derived a simple relationship between the eigenstates of the Hamiltonian and a dynamical invariant of the system. They then demonstrated how to track the evolution of a state in the time-dependent harmonic oscillator potential and to describe a charged particle in a time-dependent electromagnetic field using this protocol.

A dynamical invariant $\hat{I}(t)$ is a Hermitian operator with a time-independent expectation value, i.e.,

$$\langle \hat{I} \rangle = \langle \Psi(t)| \hat{I}(t) |\Psi(t)\rangle = \text{const}, \tag{2.34}$$

where $|\Psi(t)\rangle$ is the state vector evolved by the Hamiltonian $\hat{H}(t)$. This satisfies

$$i\hbar \frac{\partial \hat{I}(t)}{\partial t} - [\hat{H}(t), \hat{I}(t)] = 0 \tag{2.35}$$

in the Schrödinger picture [80], where $[A, B] = AB - BA$ is the commutator. The states $|\psi_n(t)\rangle$, defined by a gauge transformation

$$|\psi_n(t)\rangle = e^{i\alpha_n(t)} |\phi_n(t)\rangle \tag{2.36}$$

of the eigenbasis $\hat{I}(t)\left|\phi_n(t)\right\rangle = \lambda_n\left|\phi_n(t)\right\rangle$ are each a solution to the time-dependent Schrödinger equation, and it can be shown that $\dot{\lambda}_n = 0$. In Eq. (2.36), the "Lewis-Riesenfeld phases" $\alpha_n(t)$ are defined as

$$\alpha_n(t) = \frac{1}{\hbar}\int_{t_0}^{t}\left\langle\phi_n(t')\right| i\hbar\frac{\partial}{\partial t'} - \hat{H}(t')\left|\phi_n(t')\right\rangle dt'. \tag{2.37}$$

It follows that a general solution $\left|\Psi(t)\right\rangle$ to the Schrödinger equation can be decomposed as

$$\left|\Psi(t)\right\rangle = \sum_n c_n\left|\psi_n(t)\right\rangle = \sum_n c_n e^{i\alpha_n(t)}\left|\phi_n(t)\right\rangle, \tag{2.38}$$

where c_n are time-independent amplitudes. Thus, the unitary time-evolution operator can be written as

$$\hat{U}(t) = \sum_n e^{i\alpha_n(t)}\left|\phi_n(t)\middle\rangle\middle\langle\phi_n(t_0)\right|, \tag{2.39}$$

and the evolution of the system can now be tracked in the invariant basis.

Lewis and Riesenfeld originally used this definition of the time evolution operator with the goal of finding the unknown time-evolution of the state given some known time-dependent Hamiltonian. However, interest in Lewis-Riesenfeld invariants grew immensely decades later when the concept of inverse engineering was applied [31]. Here, the desired time-evolution of the system is given, and one uses Eq. (2.39) along with Eq. (2.24) to explicitly solve for the driving Hamiltonian,

$$\hat{H}(t) = -\hbar\sum_n \dot{\alpha}_n\left|\phi_n(t)\middle\rangle\middle\langle\phi_n(t)\right| + i\hbar\sum_n\left|\partial_t\phi_n(t)\middle\rangle\middle\langle\phi_n(t)\right|. \tag{2.40}$$

Equating the Hamiltonian in the invariant basis to the original Hamiltonian creates a map between the physical parameters and the auxiliary parameters that define the invariant operator. We use this procedure in the next chapter to derive laser detuning and Rabi frequency profiles that drive a system perfectly from its initial state to a final target state. In particular, if $\hat{H}(t)$ and $\hat{I}(t)$ are designed to commute at t_0 and t_f, i.e.,

$$\left[\hat{H}(t_0), \hat{I}(t_0)\right] = \left[\hat{H}(t_f), \hat{I}(t_f)\right] = 0, \tag{2.41}$$

then the final state $\left|\Psi(t_f)\right\rangle$ will maintain the initial populations for each eigenstate [32, 64] as the operators will be simultaneously diagonalizable. A way of visualizing this is a similar avoided crossing picture as in Fig. 2.2, but now in the invariant basis. Here, the eigenvalues are constant $\dot{\lambda}_n = 0$ which results in a constant energy splitting so that tunneling between eigenstates does not occur. We will therefore recover the results of an adiabatic process without the requirement of slow time-evolution. I note in passing the possible connection between inverse engineering using Berry's algorithm and Lewis-Riesenfeld invariants [32, 64]. In the next chapter, I apply the adiabatic shortcut to a velocity-selective particle slowing scheme, affording us with the robustness of an adiabatic slowing scheme, but with a smaller slowing time and associated slowing distance. This is the first step in creating low entropy quantum states by way of laser cooling.

Chapter 3

Speeding Up Particle Slowing Using Shortcuts to Adiabaticity

For decades, laser cooling atoms and molecules to near absolute zero has been at the forefront of research into the interactions of light and matter [35, 114, 37, 96]. Ultracold ensembles provide testbeds for exploring fundamental physics [120], can create low-temperature superfluids such as Bose-Einstein and fermionic condensates [8, 117], and can be used as platforms for quantum simulators [73]. A typical design of a laser cooling scheme for a thermal beam of particles emerging from a particle source, such as an oven or supersonic nozzle, is depicted schematically in Fig. 3.1(a). Since atom and molecule sources produce particle beams with a high average velocity, it is common to first preform a precursor slowing stage that generates a large classical force against the particle's motion [see Fig. 3.1(a)] to remove a substantial fraction of the particle's kinetic energy [see Fig. 3.1(b)]. An assortment of particle slowing methods have been developed for this precursor stage, including Stark and Zeeman decelerators [105, 67, 6, 113], centrifuge decelerators [34], electrostatic trapping methods [21], frequency-chirped laser slowing [144], white light slowing [39, 66], and angled slowing [84], among others. Once slowed, the particles may possess sufficiently low kinetic energy that they can be efficiently loaded into a finite-depth electromagnetic trap [96], such as a magneto-optical trap (MOT), and then be cooled using light [132, 145, 13], cooled through evaporation that redistributes energy through two-body collisions [134], or sympathetically cooled with another species [49]. These basic steps have been the key to opening up the world of quantum gases to many modern applications of atomic and molecular physics in quantum science and engineering.

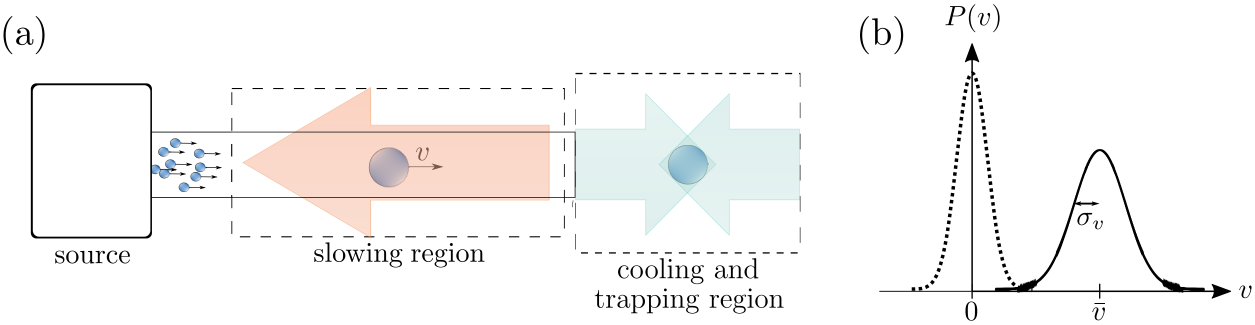

Figure 3.1: One-dimensional schematic of a generalized laser cooling experiment. (a) A thermal particle beam exits a particle source and enters a slowing region where a large classical force is applied opposite to the particles motion (orange arrow). Once the particles have sufficiently small kinetic energy, they are are then trapped and cooled by causing a large range of velocity classes to be transferred towards zero momentum within a decreased region of physical space (green arrows) and, as a result, lower entropy. (b) Schematic of the normalized velocity distributions $P(v)$ of the particle beam before (solid) and after (dashed) the slowing process. We characterize the initial distribution by a Gaussian function with a standard deviation σ_v and mean velocity $\bar{v}$.

The ability to produce a large number of ultracold particles is made difficult by practical shortcomings of slowing methods, such as a large slowing distance that requires significant physical space, or substantial spread in the final velocities of the particles. Furthermore, the main hindrance to slowing particles that lack closed cycling transitions is that there may be leakage of population to dark electronic states that are not coupled with the fields that perform the laser slowing and cooling, resulting in the loss of the particle from the system. Even if this does not occur, spontaneous emission of many photons creates momentum diffusion due to the random emission direction, and this results in heating and a finite limit on the achievable temperatures. These issues may be alleviated through tailored coherent dynamics in a timescale fast compared to the natural decay of the excited state, as discussed with rapid adiabatic passage in Section 2.3. This makes methods that increase slowing forces and minimize the number of scattering events though mostly coherent dynamics, such as SWAP cooling, the Allen-Eberly scheme [7], stimulated Raman adiabatic passage (STIRAP), the adiabatic passage force, and the bichromatic force [148, 128, 28, 100, 129, 95] enticing candidates to consider for particle slowing. However, one concern is that in order to satisfy the intrinsic adiabaticity condition, the time evolution should typically be slow and this could result in a long stopping time and associated large stopping distance.

To overcome these issues, we present a method to develop fast, simple, and robust particle slowing schemes that employ the Lewis-Riesenfeld invariant shortcut method. The slowing protocol involves driving sped-up transitions using counterpropagating, pulsed lasers with intensity and detuning profiles prescribed by the LRI shortcut. By applying this protocol many times, the particle can in principle be subject to the impulse of many photon momenta without emitting spontaneous photons. In Section 3.1, we drive a two-level system from its ground state to its excited state and back by time-ordered, single-photon transitions. We apply the protocol to a slightly more complicated model in Section 3.2, where slowing occurs by way of two-photon Raman transitions between internal ground states while maintaining a small excited state population. We then turn our attention to the next state of the cooling process (right-hand side of Fig. 3.1(a)) in Chapter 4 to create a quantum gas with low entropy.

3.1 Application to Particle Slowing in Two-Level Atoms

I now present a novel method for slowing particles via time-ordered laser sweeps sped up by adiabatic shortcuts that address a narrow electronic transition between two internal states. This work has the potential to generate large classical forces without a reliance on spontaneously emitted photons and culminated in a publication in Physical Review A [15]. We show that the application of Lewis-Riesenfeld invariants will afford our slowing scheme the advantages of adiabatic slowing schemes similar to SWAP cooling, such as robustness against the precise strength and detuning of the laser pulses, but with a much smaller slowing time and associated slowing distance. Furthermore, we demonstrate that in the limit that the excited state linewidth is much smaller than the laser's Rabi frequency, the shortcut slowing scheme has many advantages over traditional, radiation pressure based slowing schemes such as Zeeman slowers. I begin by introducing a theoretical model for the slowing scheme, presenting an analytical study of the slowing scheme in classical phase space, and studying the evolution of a momentum eigenstate and a Gaussian momentum distribution under repeated absorption and emission cycles. I conclude this section by comparing the robustness of the adiabatic shortcut to SWAP slowing and a π-pulse technique.

3.1.1 Model

We consider the experimental setup depicted in Fig. 3.2. A thermal beam of particles emerge from a particle source and enter a slowing region where a narrow transition is addressed by counterpropagating lasers. Each particle is modeled by a two-level atom, as shown in the inset. The excited state $|e\rangle$ can decay to the ground state $|g\rangle$ at a rate given by the natural linewidth $\mathit{\Gamma}$. The particles exit the source with a high average velocity and velocity large spread, as depicted in Fig. 3.1(b). The goal is to translate an appreciable fraction of the initial momentum distribution from $p \approx \bar{p}$ to $p \approx 0$, where p is the particle's momentum and $\bar{p}$ is the mean particle momentum. We track motion along one dimension, for which the particle has position and momentum operators $\hat{z}$ and $\hat{p}$. We choose to represent the slowing dynamics of the system in the momentum basis. To

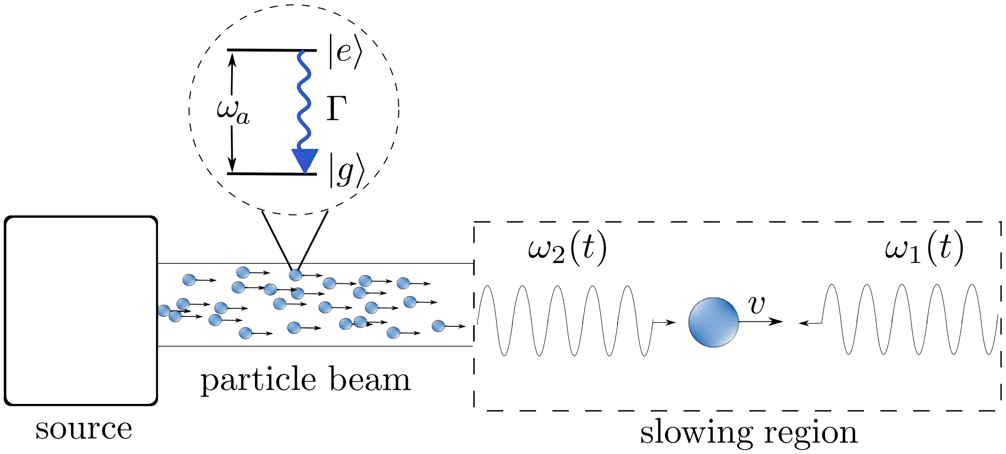

Figure 3.2: Particles exit an atom or molecule source and are collimated into the slowing region. The spatial setup of the sequentially-pulsed counterpropagating lasers, which have time-dependent frequencies $\omega_1(t)$ and $\omega_2(t)$, and a sample particle with velocity v in the laboratory frame are displayed in the slowing region. The circular inset shows the two-level internal structure of each particle.

quickly reduce the kinetic energy of an appreciable fraction of the momentum distribution, the lasers are pulsed in a time-ordered fashion to stimulate emission and absorption of photons that cause momentum impulses in the direction opposite to the particle's motion.

3.1.1.1 Slowing Mechanism

The ideal coherent dynamics are presented in Fig. 3.3, where it is assumed that the particle begins in $|g\rangle$. The counterpropagating laser (laser 1) is switched on first and its frequency ω_1 is swept over resonance. This stimulates absorption of a photon in the direction opposite to its motion, and the atom transitions to $|e\rangle$. In a timescale where it is assumed that the particle does not decay back to the ground state, the first laser is switched off and the copropagating laser (laser 2), with frequency ω_2, is turned on which causes stimulated emission back to the ground state in the direction of the laser. Therefore, by conservation of momentum, the particle experiences an impulse of $2\hbar k$ without the adverse affects of momentum diffusion that is associated with spontaneous emission. Repeating this cycle many times, we remove a plethora of momentum from a selected portion of the particles' velocity distribution through predominately coherent dynamics.

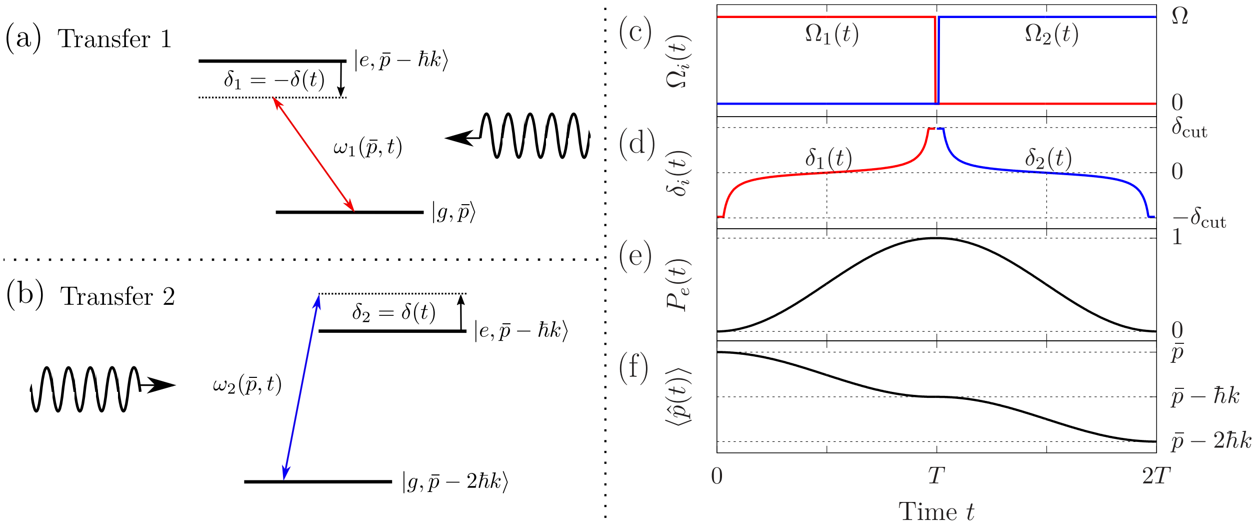

Figure 3.3: **Left**: Frequency diagram of an isolated subset of states in the lab frame. The laser frequencies $\omega_i(\bar{p}, t)$ [see Eq. (3.1)] are dynamically updated according to the solution derived from the Lewis-Riesenfeld invariant shortcut method to promote quick, coherent transfer from (a) $|g, \bar{p}\rangle$ to $|e, \bar{p} - \hbar k\rangle$, followed by (b) $|e, \bar{p} - \hbar k\rangle$ to $|g, \bar{p} - 2\hbar k\rangle$. **Right**: Experimental parameters and particle dynamics over a $|\bar{p}\rangle \rightarrow |\bar{p} - 2\hbar k\rangle$ sequence of period $2T$. (c) Square-pulse Rabi frequency profiles $\mathit{\Omega}_1(t)$ (red) and $\mathit{\Omega}_2(t)$ (blue) with amplitude $\mathit{\Omega}$ [see Eq. (3.28)]. (d) Lewis-Riesenfeld detuning profile $\delta(t)$ [see Eq. (3.29)] with cutoff frequency $\pm\delta_{\mathrm{cut}}$ [see Eq. (3.48)] for each laser. (e) Ideal excited state fraction P_e dynamics. (f) Ideal average momentum $\langle \hat{p} \rangle$ dynamics. Parameters are: $T = 0.032/\omega_r$, $\mathit{\Omega} = 100\omega_r$, $\delta_{\mathrm{cut}} = 250\omega_r$, $\mathit{\Gamma} = 0$, $\bar{p} = 100\hbar k$, and $\beta = 0.85\,\pi/2$.

We choose a square-wave profile for each laser's Rabi frequency $\mathit{\Omega}_i(t)$, whose peak value is determined by the LRI shortcut protocol. This makes the scheme robust to aligning the centers of periodic Rabi frequency and detuning profiles in time. The two lasers' Rabi frequencies $\mathit{\Omega}_1$ and $\mathit{\Omega}_2$ have the same maximum amplitude $\mathit{\Omega}$, but are, initially, completely offset [see Fig. 3.3(c)] to avoid multi-photon processes that may hinder the desired system dynamics. Our scheme is velocity selective because of the velocity-dependent Doppler shift $\pm kv$ of the two laser fields. Thus, we parameterize the instantaneous frequencies of each laser, $\omega_1(t)$ and $\omega_2(t)$, to account for the mean particle velocity $\bar{v} = \bar{p}/m$,

$$\begin{aligned} \omega_1(\bar{p}, t) &= \omega_a - \delta(t) - k\bar{v} + \omega_r \\ \omega_2(\bar{p}, t) &= \omega_a + \delta(t) + k\bar{v} - 3\omega_r, \end{aligned} \tag{3.1}$$

where $\omega_r \equiv \hbar k^2/2m$ is the recoil frequency and m is the particle's mass. The photon wavenumber k is approximated to be constant throughout the slowing process, although the frequecy is varying. Each laser is on resonance with the associated transition displayed in Fig. 3.3(a-b) when the detuning $\delta(t)$ is zero, where we have introduced the notation $|i, p\rangle = |i\rangle \otimes |p\rangle$ since the internal and momentum Hilbert spaces are simultaneously diagonalizable. Here, $|i\rangle, i \in \{g, e\}$ is in the internal Hilbert space and $\hat{p}\,|p\rangle = p\,|p\rangle$ is a momentum eigenstate with eigenvalue p. The explicit form of $\delta(t)$ is derived from the LRI shortcut method, and is the aim of this subsection. Similar results to those presented here may also be obtained by flipping the sign of $\delta(t)$ in Eq. (3.1).

3.1.1.2 System Dynamics

We apply the Hamiltonian to a system with momentum $\bar{p} = m\bar{v}$. It takes the form

$$\hat{H}(\bar{p}, t) = \hat{H}_{\text{self}} + \hat{H}_{\text{int}}(\bar{p}, t), \tag{3.2}$$

where the particle's free evolution Hamiltonian is given by

$$\hat{H}_{\text{self}}(\bar{p}, t) = \frac{\hat{p}^2}{2m} + \frac{\hbar\omega_a}{2}\hat{\sigma}^z, \tag{3.3}$$

where the first term represents the particle's kinetic energy and $\hat{\sigma}^z \equiv |e\rangle\langle e| - |g\rangle\langle g|$ is the usual Pauli spin matrix. Under the dipole and rotating wave approximations (see Appendix A), the particle-field interaction Hamiltonian in the Schrödinger picture is given by

$$\hat{H}_{\text{int}}(\bar{p},t) = \frac{\hbar}{2}\,\hat{\sigma}^{-}\left[\mathit{\Omega}_1(t)e^{i[k\hat{z}+\eta_1(\bar{p},t)]} + \mathit{\Omega}_2(t)e^{-i[k\hat{z}-\eta_2(\bar{p},t)]}\right] + \text{H.c.}, \tag{3.4}$$

where $\hat{\sigma}^{-} \equiv |g\rangle\langle e|$ is the lowering operator, $\exp[-ik\hat{z}]\,|p\rangle = |p - \hbar k\rangle$ is the momentum-shift operator [130, Chapter 6], and the accumulated phase of each laser field is given by

$$\eta_i(\bar{p},t) \equiv \int_{t_0}^{t} \omega_i(\bar{p},t')dt'. \tag{3.5}$$

The relevant physics of the laser-field interaction can be captured in the first transfer when laser 2 is off ($\mathit{\Omega}_2 = 0$), where the interaction Hamiltonian becomes

$$\hat{H}_{\text{int}}(\bar{p},t) = \frac{\hbar\mathit{\Omega}_1(t)}{2}\left(\hat{\sigma}^{-}e^{i[k\hat{z}+\eta_1(\bar{p},t)]} + \text{H.c.}\right). \tag{3.6}$$

We move into the interaction picture defined by

$$\hat{H}_0(t) = \frac{\hat{p}^2}{2m} + \frac{\hbar}{2}\left[\omega_a - \delta(t)\right]\hat{\sigma}^{z}, \tag{3.7}$$

resulting in the Hamiltonian (see Appendix B.3)

$$\hat{H}_1(\bar{p},t) = \frac{\hbar\delta(t)}{2}\hat{\sigma}^{z} + \frac{\hbar\mathit{\Omega}_1(t)}{2}\left(\hat{\sigma}^{-}\exp\!\left(i\left[k\hat{z} + k\left(\frac{\hat{p}}{m} - \bar{v}\right)t + \omega_r t\right]\right) + \text{H.c.}\right). \tag{3.8}$$

The Hamiltonian associated with laser 2 being on $\hat{H}_2(\bar{p},t)$ is found by the substitutions $1 \to 2$, $\delta(t) \to -\delta(t)$, $k \to -k$, and $\omega_r \to -3\omega_r$ into Eq. (3.8). After application of $\hat{H}_1(\bar{p},t)$ followed by $\hat{H}_2(\bar{p},t)$, the particle ideally has decreased its momentum by $2\hbar k$, and thus the addressed momentum state $\bar{p}$ is updated to $\bar{p} - 2\hbar k$ in the laser detunings [Eq. (3.1)] and the process is repeated. This repeated cycle takes place until the particle ideally reaches $\bar{p} = 0$.

We are now tasked with the duty of finding the appropriate forms of the detuning profile $\delta(t)$ using the LRI shortcut protocol. To simplify the analytical complexity of this, we limit our scope to a small, isolated subset $W(\bar{p})$ of the full composite Hilbert space during transfer 1,

$$W(\bar{p}) = \{|g,\bar{p}\rangle\,,|e,\bar{p}-\hbar k\rangle\} \equiv \{|G\rangle\,,|E\rangle\}. \tag{3.9}$$

In this subspace, the interaction Hamiltonian $\hat{H}_1(t)$ is given by

$$\hat{H}_1^{(W)}(t) = \frac{\hbar\delta(t)}{2}\hat{\sigma}_W^{z} + \frac{\hbar\mathit{\Omega}_1(t)}{2}\hat{\sigma}_W^{x}, \tag{3.10}$$

where we have introduced the W subsystem Pauli matrices $\hat{\sigma}^z_W \equiv |E\rangle\langle E| - |G\rangle\langle G|$ and $\hat{\sigma}^x_W \equiv |G\rangle\langle E| + |E\rangle\langle G|$. In parallel to Eqs. (2.13) and (2.16), the eigenvectors are given by

$$\begin{aligned} |+(t)\rangle &= \cos\left(\frac{\chi(t)}{2}\right)|E\rangle + \sin\left(\frac{\chi(t)}{2}\right)|G\rangle\,, \\ |-(t)\rangle &= \sin\left(\frac{\chi(t)}{2}\right)|E\rangle - \cos\left(\frac{\chi(t)}{2}\right)|G\rangle\,, \end{aligned} \tag{3.11}$$

with associated eigenvalues

$$E_\pm(t) = \pm\frac{\hbar\tilde{\Omega}_1(t)}{2}, \tag{3.12}$$

and we have introduced the generalized Rabi frequency $\tilde{\Omega}_1 \equiv \sqrt{\delta^2 + \Omega_1^2}$ and mixing angle $\cos\chi \equiv \delta/\tilde{\Omega}_1$. Similar to [32], we cast the eigenvectors of our invariant operator in a similar form to the eigenvectors of $\hat{H}_1^{(W)}$. The subset

$$W'(\bar{p}) = \{|e, \bar{p} - \hbar k\rangle\,, |g, \bar{p} - 2\hbar k\rangle\} \tag{3.13}$$

is then used to calculate the corresponding quantities for transfer 2 which follows in a straightforward manner.

3.1.1.3 Shortcut Application

We are now in a position to design an invariant operator in order to end up with the desired final populations. The construction of the invariant operator and its associated eigenvalue equation can be a difficult process, and various methods have been introduced to overcome this [80, 55, 74, 43]. However, since we have the form of the Hamiltonian and its eigenvectors, we need only to parameterize $\hat{I}(t)$ and $|\phi_n(t)\rangle$ in the same functional forms. Thus, in an identical manner to [32], we use the inverse engineering approach to parameterize $\delta(t)$ and $\Omega_1(t)$ as to begin and end the sweep with the desired populations. Note that this derivation holds for time-dependent $\Omega(t)$ unless noted otherwise.

We parameterize the eigenvectors of an invariant operator $\hat{I}(t)$ in parallel to Eq. (3.11):

$$\begin{aligned} |\phi_+(t)\rangle &= \cos\left(\frac{\gamma}{2}\right)e^{i\beta}|E\rangle + \sin\left(\frac{\gamma}{2}\right)|G\rangle\,, \\ |\phi_-(t)\rangle &= \sin\left(\frac{\gamma}{2}\right)|E\rangle - \cos\left(\frac{\gamma}{2}\right)e^{-i\beta}|G\rangle\,, \end{aligned} \tag{3.14}$$

where $\gamma = \gamma(t)$ and $\beta = \text{const}$ are auxiliary angles. The unitary phase $e^{i\beta}$ was introduced as an additional degree of freedom to define the shortcut solution, as we shall see in subsection 3.1.2. It follows that the invariant with eigenvalues $\lambda_{\pm} = \pm\hbar\mathit{\Omega}'/2$ can be written in the basis of the Hamiltonian as

$$\hat{I}(t) = \frac{\hbar\mathit{\Omega}'}{2}\begin{pmatrix} \cos\gamma & \sin\gamma\, e^{i\beta} \\ \sin\gamma\, e^{-i\beta} & -\cos\gamma \end{pmatrix}, \tag{3.15}$$

where $\mathit{\Omega}'$ is an arbitrary constant frequency in order to keep $\hat{I}(t)$ with units of energy. Substituting Eqs. (3.10) and (3.14) into Eq. (2.37), we calculate the Lewis-Riesenfeld phases for transfer 1 as

$$\alpha_{\pm}(t) = \mp\frac{1}{2}\int_0^t (\delta\cos\gamma + \mathit{\Omega}_1\sin\gamma\cos\beta)\, dt'. \tag{3.16}$$

Substituting these phases into Eq. (2.40), we find that the Hamiltonian is parameterized by

$$\hat{H}_1^{(W)}(t) = \frac{\hbar}{2}\begin{pmatrix} A & B\, e^{i\beta} \\ B\, e^{-i\beta} & -A \end{pmatrix}, \tag{3.17}$$

where

$$A = \delta(t)\cos^2\gamma + \mathit{\Omega}_1(t)\cos\gamma\sin\gamma\cos\beta, \tag{3.18}$$

$$B = \delta(t)\cos\gamma\sin\gamma + \mathit{\Omega}_1(t)\sin^2\gamma\cos\beta - i\dot{\gamma}. \tag{3.19}$$

Equating the two forms of the Hamiltonian [Eqs. (3.10) and (3.17)], we arrive at the auxiliary equations

$$\dot{\gamma} = \mathit{\Omega}_1(t)\sin\beta, \tag{3.20}$$

$$\delta = \mathit{\Omega}_1(t)\cot\gamma\cos\beta, \tag{3.21}$$

from which we determine the experimental parameters $\delta(t)$ and $\mathit{\Omega}_1(t)$, subject to the boundary conditions on the auxiliary variables γ and β required for state transfer from state $|G\rangle$ to $|E\rangle$, which we now determine.

As seen from Eq. (3.14), γ must satisfy

$$\gamma(t_0) = \pi n, \qquad \gamma(t_f) = \gamma(t_0) + \pi(2m+1), \tag{3.22}$$

to induced state transfer, where n and m are integers. For simplicity and without loss of generality, we choose $n = m = 0$ so that

$$\gamma(t_0) = 0, \qquad \gamma(t_f) = \pi \tag{3.23}$$

and causes the state $|\phi_-(t)\rangle$ to align with $|G\rangle$ and $|E\rangle$ at initial and final times t_0 and t_f, respectively. Since the commutator between $\hat{H}_1^{(W)}(t)$ and $\hat{I}(t)$ is

$$\begin{aligned}\left[\hat{H}_1^{(W)}(t), \hat{I}(t)\right] =& \frac{\hbar^2 \varOmega'}{2}\Big(-i\varOmega_1 \sin\gamma \sin\beta \hat{\sigma}_W^z \\ &+ (\delta \sin\gamma e^{i\beta} - \varOmega_1 \cos\gamma)\hat{\sigma}_W^+ + (\varOmega_1 \cos\gamma - \delta \sin\gamma e^{-i\beta})\hat{\sigma}_W^-\Big),\end{aligned} \tag{3.24}$$

where $\hat{\sigma}_W^- = (\hat{\sigma}_W^+)^\dagger \equiv |G\rangle\langle E|$, we should also impose

$$\varOmega_1(t^*) \sin\gamma(t^*) \sin\beta = 0, \tag{3.25}$$

$$\beta = q\pi \tag{3.26}$$

for $t^* = t_0$ and $t^* = t_f$ and integer q to align the eigenbases of $\hat{H}_1^{(W)}(t)$ and $\hat{I}(t)$ at the beginning and end of the shortcut process [see Eq. (2.41)]. The condition (3.25) is automatically satisfied by (3.23), whereas the condition (3.26) is not necessary to enforce in the case of complete state transfer because it only affects non-physical, global phases.

We have now parameterized the Hamiltonian in terms of the auxiliary angles and found boundary conditions for these angles for the interaction with laser 1. The corresponding quantities for the subsequent interaction with laser 2 are derived in a similar manner. Note that the particular choice of invariant eigenvector does not affect the resulting form of $\delta(t)$ and $\varOmega_1(t)$. As we shall see in Section 3.2, the general case of $\varOmega_1(t) \neq$ const results in the task of choosing, from an infinite set of Hamiltonians, a particular form of $\gamma(t)$ and $\beta(t)$ that satisfy the boundary conditions. We now use Eqs. (3.20), (3.21), and (3.23) to determine the detuning profile associated with a constant Rabi frequency over a single sweep $\varOmega_1(t) = \varOmega =$ const.

We first define the initial and final times $t_0 = 0$ and $t_f = T$. From the auxilary equation Eq (3.20) and the boundary condition $\gamma(0) = 0$, we see

$$\gamma(t) = (\varOmega \sin\beta)t. \tag{3.27}$$

To satisfy the other γ boundary condition $\gamma(T) = \pi$, we require that

$$\pi = \mathit{\Omega} T \sin\beta, \tag{3.28}$$

which we combine with Eqs. (3.21) and (3.27) to arrive at

$$\delta(t) = \frac{\pi \cot\beta}{T} \cot\left(\frac{\pi t}{T}\right). \tag{3.29}$$

This is the main result of this subsection, and a plot of $\delta(t)$ for a particular choice of β and T is given in Fig. 3.3(d). We now have a particular Hamiltonian that will drive the $|g, \bar{p}\rangle \rightarrow |e, \bar{p} - \hbar k\rangle$ transition with dynamics that do not have to be adiabatic. The process is repeated to derive the same profiles for laser 2 to drive the transition $|e, \bar{p} - \hbar k\rangle \rightarrow |g, \bar{p} - 2\hbar k\rangle$. Ideal dynamics of this cycle is shown in Fig. 3.3(e-f). The method may be optimized further with respect to different cost functions, but we do not explore such solutions here (e.g., see [131]). We now, similar to subsection 2.4.1, examine the trajectories of the Bloch vector for different shortcut solutions.

3.1.2 Bloch Sphere Trajectories

As stated with Eq. (3.14), different choices of the auxiliary angle β can result in distinct dynamics as the particle is transferred from $|G\rangle$ and $|E\rangle$. This can be seen by investigating the Bloch sphere trajectories. As seen from Eqs. (3.10), (3.29), and $\mathit{\Omega}_1(t) = \mathit{\Omega} = \text{const}$, the trajectories under $\hat{H}_1(t)$ are purely longitudinal and parameterized by β. For a better comparison, we instead transform into a time-dependent interaction picture defined by the free evolution Hamiltonian Eq. (3.3). This results in the interaction Hamiltonian in the W subspace,

$$\hat{H}_I^{(W)}(t) = \frac{\hbar \mathit{\Omega}}{2} \left(e^{i\theta(t)} |E\rangle\langle G| + \text{H.c.}\right), \tag{3.30}$$

where the accumulated phase of the detuning is defined as

$$\theta(t) \equiv \int_{t_0}^{t_f} \delta(t')dt', \tag{3.31}$$

with $\delta(t)$ given by Eq. (3.29).

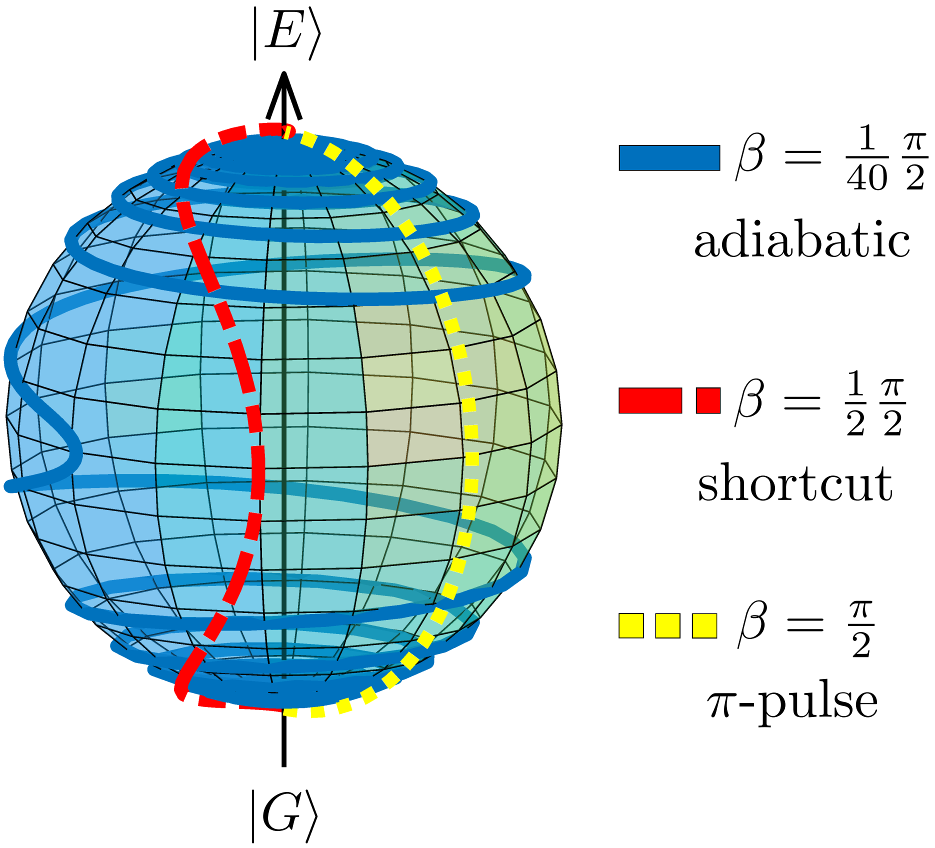

Figure 3.4: Bloch sphere trajectories (thick curves) between the initial state $|G\rangle$ and final state $|E\rangle$ parameterized by the auxiliary angle β [see Eq. (3.14)] in the free-energy interaction picture [see Eq. (3.30)]. We set the Rabi frequency Ω to be equal for all trajectories, and the slowing periods T are given by Eq. (3.28). The cutoff detunings for $\beta = \frac{1}{40}\frac{\pi}{2}$ and $\beta = \frac{1}{2}\frac{\pi}{2}$ are $\delta_{\mathrm{cut}} = 318\Omega$ and $\delta_{\mathrm{cut}} = 225\Omega$, respectively [see Eq. (3.48)].

We plot the Bloch vector trajectories for three choices of β with a fixed Rabi frequency Ω in Fig. 3.4. The slowing periods T vary from trajectory to trajectory since it is completely determined by β from Eq. (3.28) when Ω is a constant. A choice of $\beta = (r + \frac{1}{2})\pi$ for integer r minimizes the slowing period. Since this results in $\delta(t) = 0$, this corresponds to a simple, resonant π-pulse (see Section 2.3). The choice of $r = 0$ results in the longitudinal Bloch sphere trajectory (yellow, dotted curve) in Fig. 3.4. However, this choice of β can lead to many experimental challenges, such as sensitivity to errors in Ω. This point will be investigated further in subsection 3.1.6. The choice of $\beta = s\pi$ for integer s results in an adiabatic process as T tends towards infinity. We approximate $s = 0$ to have a finite slowing time by using $\beta = \frac{1}{40}\frac{\pi}{2}$, which results in the highly processing curve (blue, solid curve) in Fig. 3.4. This results in a long slowing distance, increased probability of spontaneous emission, and a large sensitivity to laser phase. We therefore use a choice from the range $0 \ll \beta < \pi/2$ that results in an intermediate trajectory for our slowing example in subsection 3.1.5. The middle trajectory (red, dash-dotted curve) in Fig. 3.4 results from the choice $\beta = \pi/4$.

3.1.3 Quantum Master Equation

So far, we have only considered the system's coherent, reversible dynamics. We now include the incoherent, irreversible dynamics due to spontaneous emission, incoherent pumping, and dephasing, among others, by considering an *open quantum system.* Here, the full system-environment density matrix $\hat{\rho}_{SB}(t)$ that undergoes unitary dynamics is assumed, by the Born-Markov approximation, to factorize $\hat{\rho}_{SB}(t) = \hat{\rho}_S(t) \otimes \hat{\rho}_B$, where $\hat{\rho}_B$ is a stationary-state of the reservoir. We then preform a partial trace over the degrees of freedom of the reservoir to arrive at the reduced density matrix

$$\hat{\rho}(t) \equiv \hat{\rho}_S(t) = \mathrm{Tr}_B[\hat{\rho}_{SB}(t)]. \tag{3.32}$$

We can now derive an equation of motion for the state of the system alone that undergoes dynamics that need not be unitary. See Appendix C for a comprehensive study on open quantum systems.

Typically, the system's incoherent dynamics are incorporated by evolving the reduced density matrix via the quantum master equation in Lindblad form [82] (see Appendix C.1):

$$\frac{\partial \hat{\rho}}{\partial t} = \frac{1}{i\hbar}\left[\hat{H}, \hat{\rho}\right] + \hat{\mathcal{L}}(\hat{\rho}). \tag{3.33}$$

The Lindblad superoperator $\hat{\mathcal{L}}(\hat{\rho})$ depicts the irrevesible dynamics and takes the general form

$$\hat{\mathcal{L}}(\hat{\rho}) = \sum_j \hat{\mathcal{D}}[\hat{C}_j]\hat{\rho} = \sum_j \hat{C}_j\hat{\rho}\hat{C}_j^\dagger - \frac{1}{2}\{\hat{C}_j^\dagger\hat{C}_j, \hat{\rho}\}, \tag{3.34}$$

where the summation is over all of the system's jump operators $\hat{C}_j$ and $\{A, B\} = AB + BA$ is the anti-commutator. Meanwhile, the first term on the right hand side of Eq. (3.33) represents the unitary dynamics of the system, and reduces to the Schrödinger equation when $\hat{\mathcal{L}} = 0$. The right hand side of the master equation can be written compactly as the Liouvillian superoperator,

$$\hat{\mathfrak{L}}[\hat{\rho}] = -\frac{i}{\hbar}[\hat{H}, \hat{\rho}] + \sum_j \hat{\mathcal{D}}[\hat{C}_j]\hat{\rho}. \tag{3.35}$$

For the slowing schemes considered in this chapter, the only incoherent process is spontaneous emission from the excited state to the ground state manifold at a rate $\mathit{\Gamma}$. Since we use a discreet momentum grid that is parameterized by integer multiples of photon momenta, we approximate the continuous dipole radiation pattern to only have three discreet recoil probabilities that correspond to whole integers of $\hbar k$. For the two-level system, this can be described by three jump operators for each momentum state,

$$\hat{C}_0^{(p)} = \sqrt{\frac{3\mathit{\Gamma}}{5}}\hat{\sigma}^- \otimes |p\rangle\langle p|\,, \quad \hat{C}_-^{(p)} = \sqrt{\frac{\mathit{\Gamma}}{5}}\hat{\sigma}^- \otimes |p - \hbar k\rangle\langle p|\,, \quad \hat{C}_+^{(p)} = \sqrt{\frac{\mathit{\Gamma}}{5}}\hat{\sigma}^- \otimes |p + \hbar k\rangle\langle p|\,. \tag{3.36}$$

Thus, the system's Lindblad superoperator $\hat{\mathcal{L}}(\hat{\rho}) = \sum_p \sum_j \hat{\mathcal{D}}[\hat{C}_j^{(p)}]\hat{\rho}$ takes the form [102]

$$\hat{\mathcal{L}}(\hat{\rho}) = -\frac{\mathit{\Gamma}}{2}\left[\hat{\sigma}^+\hat{\sigma}^-\hat{\rho} + \hat{\rho}\hat{\sigma}^+\hat{\sigma}^- - \frac{2}{5}\left(3\,\hat{\sigma}^-\hat{\rho}\hat{\sigma}^+ \;+\; e^{ik\hat{z}}\hat{\sigma}^-\hat{\rho}\hat{\sigma}^+e^{-ik\hat{z}} + e^{-ik\hat{z}}\hat{\sigma}^-\hat{\rho}\hat{\sigma}^+e^{ik\hat{z}}\right)\right], \tag{3.37}$$

which implies possible impulses of $-\hbar k$, 0, and $\hbar k$ along the slowing axis with associated probabilities of $\frac{1}{5}$, $\frac{3}{5}$, and $\frac{1}{5}$, respectively. I will study numerical simulations of Eq (3.33) for our slowing system in Section 3.1.5. Beforehand, however, I preform an analytical study of the system's slowing dynamics in classical phase space to determine the usefulness of our slowing protocol and compare to results from methods that rely on radiation pressure.

slowing method	force F	slowing time $\varDelta t$	slowing distance $\varDelta x$	scattering rate R^s	number of scattered photons N
Lewis-Riesenfeld	$\frac{\varOmega \hbar k \sin\beta}{\pi}$	$\frac{\pi\zeta_0}{\varOmega \sin\beta}$	$\frac{\omega_r \zeta_0^2}{2\varOmega \sin\beta}\lambda$	$\frac{\varGamma}{2}$	$\frac{\varGamma}{\varOmega}\frac{\pi}{2\sin\beta}\zeta_0$
Radiation pressure	$\varGamma \hbar k \rho_{\mathrm{ee}}$	$\frac{\zeta_0}{\varGamma \rho_{\mathrm{ee}}}$	$\frac{\omega_r \zeta_0^2}{2\pi \rho_{\mathrm{ee}} \varGamma}\lambda$	$\varGamma \rho_{\mathrm{ee}}$	ζ_0

Table 3.1: Comparison of slowing dynamics between the shortcut slowing scheme based on Lewis-Riesenfeld invariants and radiation pressure slowing. If $\varOmega \sin\beta \gg \pi \varGamma \rho_{\mathrm{ee}}$, the shortcut slowing scheme results in larger forces, shorter slowing times, shorter slowing distances, and fewer scattered photons than RP.

3.1.4 Slowing Dynamics in Classical Phase Space

We now determine whether the LRI shortcut method can achieve a practical device that is competitive with slowing methods that are regularly employed. To do this, we compare different quantities associated with the slowing process in LRI slowing to commonly-implemented processes that rely on radiation pressure (RP) such as Zeeman slowers or Stark decelerators. We calculate quantities such as the classical force associated with each sweep, total slowing distance, and number of scattered photon below, and present the results in Table 3.1.

We first note the classical force $F = \varDelta p/\varDelta t$ exerted on the particle during each sweep is given by

$$F_{\mathrm{LRI}} = \frac{\hbar k}{T} = \frac{\varOmega \hbar k \sin\beta}{\pi}, \tag{3.38}$$

where we have used Eq. (3.28). In contrast, the classical force from RP is given by

$$F_{\mathrm{RP}} = \varGamma \hbar k \rho_{ee} \leq \frac{\varGamma \hbar k}{2}, \tag{3.39}$$

where ρ_{ee} is the excited state fraction and equality is reached with infinite laser power [96].

Assuming the particle begins the slowing process in the eigenstate $|g, \bar{p}_0\rangle$, it receives an impulse of $\hbar k$ against its motion for a total time

$$\varDelta t_{\mathrm{LRI}} = \frac{T\bar{p}_0}{\hbar k} = \frac{\pi\zeta_0}{\varOmega \sin\beta}, \tag{3.40}$$

until it reaches zero momentum, where $\zeta = p/\hbar k$ is the momentum number and $\zeta_0 = \bar{p}_0/\hbar k$ is the initial momentum number.

We can now calculate the distance that a particle that undergoes the slowing process travels in physical space in order to reach zero momentum. We approximate $p(t)$ during the LRI scheme to be linear,

$$p(t) \approx \bar{p}_0 - \frac{\hbar k t}{T} = \hbar k \left(\zeta_0 - \frac{t}{T} \right), \tag{3.41}$$

so that we may write the slowing distance as

$$\Delta x_{\mathrm{LRI}} = \frac{p_{\mathrm{avg}}}{m} \Delta t_{\mathrm{LRI}} = \frac{\omega_r T \zeta_0^2}{2\pi} \lambda, \tag{3.42}$$

where $p_{\mathrm{avg}} \equiv \bar{p}_0/2$ is the time-averaged momentum and λ is the wavelength of the electronic transition, which is typically $\mathcal{O}(10^{-7}\,\mathrm{m})$. We rewrite this using Eq. (3.28) in terms of the Rabi frequency:

$$\Delta x_{\mathrm{LRI}} = \frac{\omega_r \zeta_0^2}{2\Omega \sin\beta} \lambda. \tag{3.43}$$

Using a similar method, we obtain the related expression for the RP slowing distance,

$$\Delta x_{\mathrm{RP}} = \frac{\omega_r \zeta_0^2}{2\pi \rho_{ee} \Gamma} \lambda. \tag{3.44}$$

Comparing the LRI and RP results, we find that the shortcut slowing scheme is able to exert higher forces, and therefore slow particles in a shorter distance, when $\Omega \sin\beta \gg \pi \Gamma \rho_{ee}$, which reduces to $\Omega \gg \Gamma$ when $\sin\beta$ is chosen to be on order of unity.

So far, we have not incorporated the effects due to dissipation as a result of spontaneous emission in the analysis of the LRI scheme. Since the mechanism to reduce momentum in this scheme is purely coherent, the ideal case is when there is no scattered photons during the process. This can be nearly accomplished by using ultra-narrow linewidth transitions or by applying the entire slowing protocol in a time that is shorter that the lifetime of the excited state. The latter method typically requires an extremely large laser power, but also results in an extremely small slowing distance. Furthermore, we will show in Section 3.2 that application of the shortcut to a two-photon Raman transition between internal ground states can greatly reduce the scattering rate through an engineered excited state linewidth [see Eq. (3.70)]. Nevertheless, the scattering rate R^s of the LRI slowing technique is approximately

$$R^s_{\mathrm{LRI}} \approx \frac{\mathit{\Gamma}}{2} \tag{3.45}$$

since the particles are in the excited state for roughly half the slowing time. This is the saturation of the inequality

$$R^s_{\mathrm{RP}} \approx \mathit{\Gamma} \rho_{ee} \leq \frac{\mathit{\Gamma}}{2} \tag{3.46}$$

for the RP scattering rate [96]. However, the expected number of scattered photons, $N = R^s \mathit{\Delta} t$ for each technique is

$$N_{\mathrm{LRI}} \approx \frac{\mathit{\Gamma}}{\mathit{\Omega}} \frac{\pi}{2 \sin \beta} \zeta_0, \qquad N_{\mathrm{RP}} \approx \zeta_0. \tag{3.47}$$

This again implies that the LRI slowing scheme is advantageous to RP schemes when $\mathit{\Omega} \gg \mathit{\Gamma}$, with $\sin \beta$ on order of unity, as it generates much fewer scattered photons.

3.1.5 Slowing Example

By repeatedly driving the transition $|g, \bar{p}\rangle \to |e, \bar{p} - \hbar k\rangle$ followed by $|e, \bar{p} - \hbar k\rangle \to |g, \bar{p} - 2\hbar k\rangle$ according to our shortcut solution, we now show that we are able to slow a significant number of particles when the full composite Hilbert space $\mathcal{H}_i \otimes \mathcal{H}_p$ is taken into account. After each pair of transitions, we update the momentum $\bar{p}$ to $\bar{p} - 2\hbar k$ in the laser frequencies Eq. (3.1), as we assume that the initial population in $|g, \bar{p}\rangle$ has moved to $|g, \bar{p} - 2\hbar k\rangle$. Note that this procedure results in the slowing of a pulse of particles, as opposed to a steady-state ensemble. We assume that the jump in laser frequency at the end of each ramp is perfectly diabatic. Since there is very little population transfer when $\delta(t) \gg \mathit{\Omega}$, we do not track the detuning profile's asymptotic behavior, as this can cause numerical errors. We thus take $\delta(t)$ to be equal to a constant $\pm\delta_{\mathrm{cut}}$ in these regions, defined by

$$\delta(t < t_0 + t_{\mathrm{cut}}) = -\delta(t > t_f - t_{\mathrm{cut}}) = \delta_{\mathrm{cut}} \tag{3.48}$$

for some cutoff time t_{cut}, as shown in Fig. 3.3(d). We evolve the quantum master equation Eq. (3.33) using the method of quantum Monte Carlo wave functions [102], which is presented in Appendix C.2.

Species	Transition	Wavelength (nm)	Linewidth (kHz)	Recoil frequency (kHz)	Saturation intensity (W/cm^2)
^{40}Ca	$^1S_0 \to {}^3P_1$	657	0.4	11.5	1.8×10^{-7}
^{88}Sr	$^1S_0 \to {}^3P_1$	689	7.5	4.8	3.0×10^{-6}
YO	$X^2\Sigma^+ \to A'^2\Delta_{3/2}$	690	5.9	4.0	2.3×10^{-6}
^{174}Yb	$^1S_0 \to {}^3P_1$	556	180	3.7	1.4×10^{-4}
BaH	$X^2\Sigma^+ \to A^2\Pi$	1061	1200	1.3	1.3×10^{-4}

Table 3.2: Fundamental properties for various atomic and molecular candidates for shortcut slowing on a narrow transition.

Fig. 3.5 presents the momentum distribution of an ensemble of particles before (blue line) and after (orange distribution) application of our slowing scheme over 100 sweeps of each laser in the case of purely coherent (left column) and dissipative (right column) dynamics. In the dissipative case, we chose $\varGamma = \omega_r$ as an order-of-magnitude estimate for a narrow-linewidth transition that roughly corresponds to the linewidth for the $^1S_0 \to {}^3P_1$ transition in ^{88}Sr (see Table 3.2). We chose to initialize the momentum distribution as either a momentum eigenstate at $100\hbar k$ (top row) or a Gaussian profile with an average momentum $\langle \hat{p} \rangle = 100\hbar k$ and a standard deviation of $\sigma_{p,0} = 10\hbar k$ (bottom row), which typically corresponds to an initial average particle speed on the order of 1 m/s. While actual physical systems may have much higher initial particle beam speeds, this choice sufficiently demonstrates the slowing effects of our protocol. We have chosen to use the average momentum of the Gaussian as the initial momentum used in the laser frequencies, $\bar{p}_0 = \langle \hat{p} \rangle$, because it results in the largest fraction of slowed particles. For experimental accessibility and robustness, we chose $\beta = 0.85\,\pi/2$ and $\varOmega = 100\varGamma$, which results in a shortcut time $T = 0.032/\varGamma$ typically on the order of microseconds, much shorter than the associated timescale of radiation pressure slowing on the transition. This choice of $\varOmega$ also sets the expected number of scattered photons N to be on the order of unity [see Eq. (3.47)].

As seen in Fig. 3.5, a substantial fraction of the distribution is slowed to near zero momentum. We first discuss the results in the case of purely coherent dynamics (left column). If the system begins in the eigenstate $|g, 100\hbar k\rangle$ [Fig. 3.5(a)], about 99.3% of the population ends in the zero

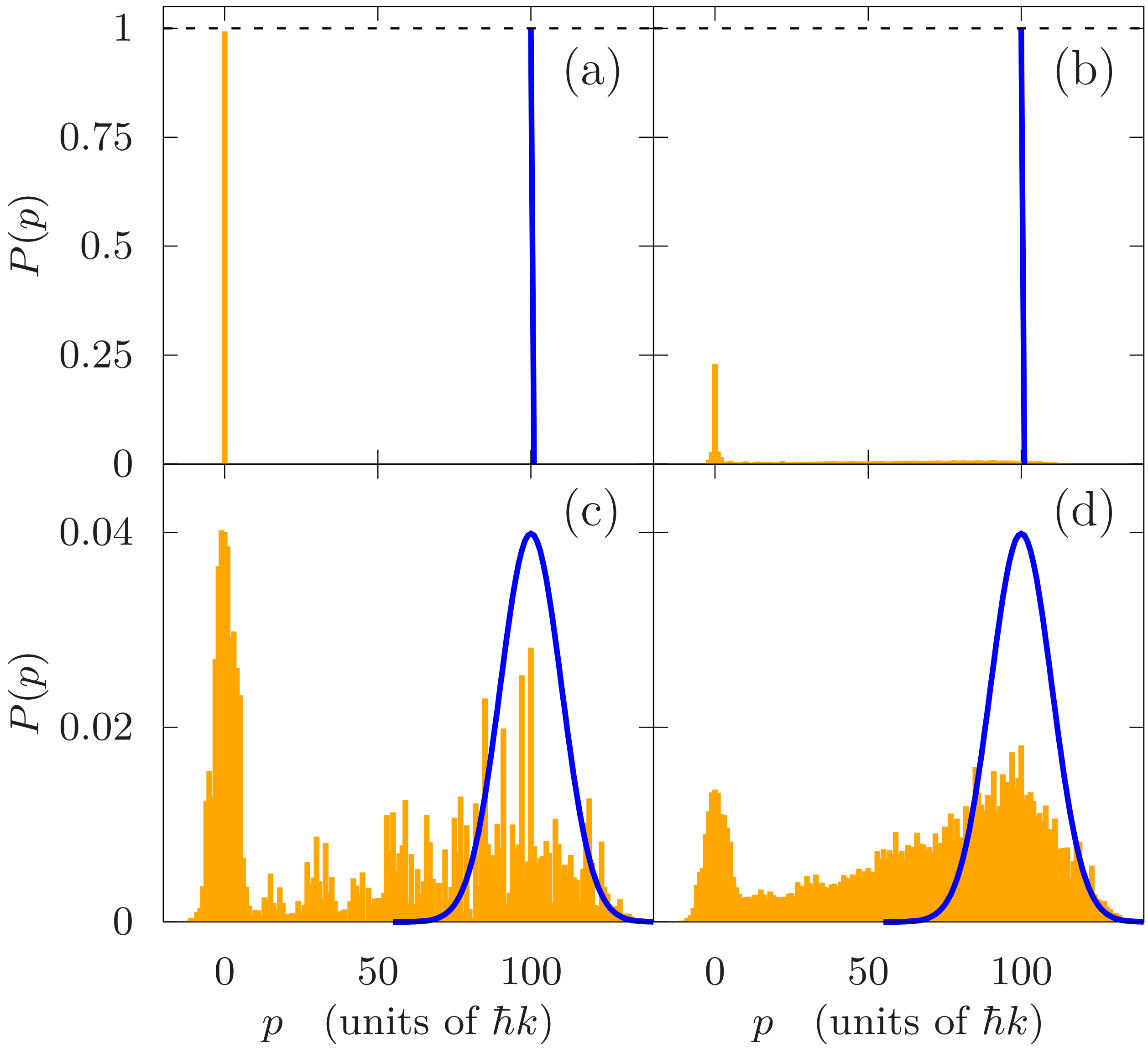

Figure 3.5: Initial (blue) and final (orange) momentum distributions $P(p)$ of a system subject to the shortcut slowing protocol. The system is initialized in the internal ground state $|g\rangle$ and with a momentum distribution of either the $100\hbar k$ eigenstate (top row) or a Gaussian state with average momentum $\langle \hat{p} \rangle = 100\hbar k$ and width $\sigma_p = 10\hbar k$ (bottom row). The excited state linewidth is $\mathit{\Gamma} = 0$ in (a) and (c), and $\mathit{\Gamma} = \omega_r$ in (b) and (d). Further details are discussed in text. Other parameters are: $\mathit{\Omega} = 100\omega_r$, $T = 0.032/\omega_r$, $t_{\text{tot}} = 1.6/\omega_r$, and $\delta_{\text{cut}} = 244\omega_r$, $\beta = 0.85\,\pi/2$, and $\bar{p}_0 = 100\hbar k$. Subplots (b) and (d) are averaged over 1,000 trajectories.

Species	Rabi frequency (MHz)	Initial speed at $200\hbar k$ (m/s)	Slowing time (μs)	Slowing distance (μm)	Capture fraction
^{40}Ca	0.2	3.0	494	746	5.6×10^{-1}
^{88}Sr	1.0	1.3	106	70	1.5×10^{-1}
YO	0.9	1.1	119	66	2.1×10^{-1}
^{174}Yb	3.4	0.82	30	12	6.8×10^{-6}
BaH	23.6	0.54	4	1	1.6×10^{-5}

Table 3.3: Slowing results for various atomic and molecular candidates using a 0.1 W/cm^2 laser intensity and starting from a momentum of $200\hbar k$. The Rabi frequency, slowing time, and slowing distance follow from Eqs. (3.49), (3.40), and (3.43) respectively, with $\beta = 0.85\,\pi/2$. The simulated capture fraction, defined as the fraction of particles with momentum $|p| \leq 3\hbar k$ after the slowing process, was calculated over 1,000 trajectories for Ca, Sr, and YO, and 10,000 trajectories for Yb and BaH.

momentum eigenstate. (We attribute the lack of 100% transfer to our use of a cutoff frequency $\delta_{\text{cut}} = 244\omega_r$.) If the system begins in a Gaussian distribution [Fig. 3.5(c)], about 35% of the population ends with momentum $|p| \leq 10\hbar k$, which corresponds to about half of the population within one standard deviation of the average momentum in the initial distribution.

In the case of dissipative dynamics, 29% of the population ends with momentum $|p| \leq \hbar k$ if the system is initialized in the eigenstate $|g, 100\hbar k\rangle$ [Fig. 3.5(b)], and 13% of the population ends with momentum $|p| \leq 10\hbar k$ if the system is initialized in the Gaussian state [Fig. 3.5(d)]. In both cases, there was an average of 1.6 scattered photons per particle, which agrees with the predicted scattering rate given in Table 3.1. This is a two order-of-magnitude improvement over the number of scattered photons that occur during radiation pressure. These results demonstrate that our protocol can potentially slow a significant fraction of particles to zero momentum in a very short distance and with a virtually negligible reliance on spontaneous emission.

As a more realistic demonstration, we present several atomic and molecular species that are reasonable candidates [110, 108, 39, 152, 137] for our slowing protocol in Table 3.2. We simulate the slowing of each species with an initial momentum of $200\hbar k$ using a 0.1 W/cm^2 laser intensity, and provide the expected slowing times $\varDelta t$, slowing distances $\varDelta x$, and capture fractions C in Table 3.3. The saturation intensity I_{sat}, laser intensity I, and Rabi frequency $\varOmega$ can be calculated according to [96]

$$2\left(\frac{\varOmega}{\varGamma}\right)^2 = \frac{I}{I_{\text{sat}}}, \quad I_{\text{sat}} \equiv \frac{\pi h c \varGamma}{3\lambda^3}, \tag{3.49}$$

where $h = 2\pi\hbar$ is Planck's constant and c is the speed of light. The calculated slowing times and distances become smaller as the transition dipole matrix element increases, as can be seen for the species with larger linewidths. However, the required temporal control of the Rabi frequency and detuning profiles in these cases may be an experimental challenge. One solution is to simply reduce the laser power, but this can quickly move the parameters away from the regime $\varOmega \gg \varGamma$, which increases the chance of spontaneous emission and hence reduces the capture fraction C.

Due to our method's sensitivity to spontaneous emission, a rough estimate for the capture fraction C is given by the fraction of particles that do not emit a single spontaneous photon throughout the slowing process. Using Eq. (3.47), this is approximately

$$C \approx \exp\left(-N_{\mathrm{LRI}}\right) = \exp\left(-\frac{\mathit{\Gamma}}{\mathit{\Omega}}\frac{\pi}{2\sin\beta}\zeta_0\right). \tag{3.50}$$

This formula is on the same order as the simulated capture fractions given in Table 3.3 for Ca, Sr, and YO, but it underestimates the results for Yb and BaH, suggesting that particles can still be slowed after emitting spontaneous photons. It should be noted that Eq. (3.50) is not a fundamental limit, as it can be improved with a more sophisticated implementation of the shortcut process, such as introducing occasional waiting periods so that the particles return to the internal ground state, allowing the laser pulses to overlap in time (as studied in Fig. 3.7), or repeating the slowing protocol over a range of momentum states. For example, we were able to increase the simulated ^{174}Yb capture fraction by over an order of magnitude to $C = 1.7 \times 10^{-4}$ by introducing a laser pulse overlap fraction $f = 0.2$ as discussed in the next subsection. Furthermore, it should be noted that atomic and molecular sources can often produce particle fluxes on the order 10^{12}-10^{14} particles/(cm · s) [97], so an $\mathcal{O}(10^{-4})$ capture fraction may still be valuable.

3.1.6 Robustness

We now study the robustness of the shortcut slowing scheme to various systematic errors that may arise in an experimental setting. Specifically, we modify the Rabi frequency amplitude, then separately consider the result of slowing a particle with a momentum p that is not equal to the momentum accounted for in the laser frequencies $\bar{p}$ (Fig. 3.6). We also consider the scheme's robustness to the temporal overlap f of the square pulses (Fig. 3.7), which may minimize scattering events since it potentially reduces the amount of time the particle remains in the internal excited state. For simplicity, we focus on a single $|g\rangle \rightarrow |e\rangle \rightarrow |g\rangle$ process and calculate the resulting impulse $\mathit{\Delta} p$ experienced by the particle. Moreover, we employ a phase relation between the laser pulses such that the Rabi frequency of each pulse is purely real. The correct detuning profiles are employed throughout this section. We set the Rabi frequency to $\mathit{\Omega} = 10\,\omega_r$ across all slowing methods, but necessarily allow for different slowing times.

Using the auxiliary variable $\beta = 0.5\,\pi/2$, we compare the robustness of our scheme to both π-pulse and SWAP slowing. As discussed in subsection 3.1.2, the π-pulse solution is a special case of our slowing method with the choice $\beta = \pi/2$, which results in a fixed detuning [see Eq. (3.29)]. SWAP slowing is simulated by using a sawtooth-wave detuning profile with full range $\varDelta_s$ and period T for each single-photon transfer. Unlike SWAP cooling, the lasers are sequentially pulsed as in Fig. 3.3(a) and 3.3(b), and the laser detunings are centered on the momentum $\bar{p}$.

As discussed in Section 2.3, the population of the (initially unoccupied) excited state P_e, if the laser is linearly chirped from a detuning of minus infinity to positive infinity, is

$$P_e = 1 - \exp\left(-\frac{\pi}{2}\frac{\varOmega^2}{\alpha}\right), \tag{3.51}$$

where α is the frequency chirping rate in rad/s^2. Therefore, to obtain a transfer probability of at least 95%, we chose to set $\varOmega^2/\alpha = 2$. Next, we increased the chance of population transfer by setting the shortcut period to be several times larger than the approximate time τ_j required to transfer population between quantum states in the adiabatic regime [147]:

$$\tau_j = \frac{2\varOmega}{\alpha} = \frac{0.4}{\omega_r} \quad \Rightarrow \quad T = \frac{1}{\omega_r} > \tau_j. \tag{3.52}$$

These choices constrained the sweep range to be $\varDelta_s = 50\,\omega_r$. Note that the resulting SWAP slowing period $T = 1/\omega_r$ is significantly longer than the π-pulse ($T \approx 0.3/\omega_r$) and shortcut slowing ($T \approx 0.4/\omega_r$) periods [see Eq. (3.28)].

Fig. 3.6(a) presents the resulting particle impulse, which reaches a maximum of $\varDelta p = -2\hbar k$, as a function of the error in the Rabi frequency amplitude, which is characterized by the small parameter ϵ:

$$\varOmega \to \varOmega(1+\epsilon). \tag{3.53}$$

While the shortcut scheme applies a similar impulse $\varDelta p$ compared to the π-pulse method for $\epsilon < 0$, it is the most robust method for $\epsilon > 0$. The SWAP slowing result, while being the most robust method for $\epsilon < 0$, can change significantly with small changes to the parameters. This instability is

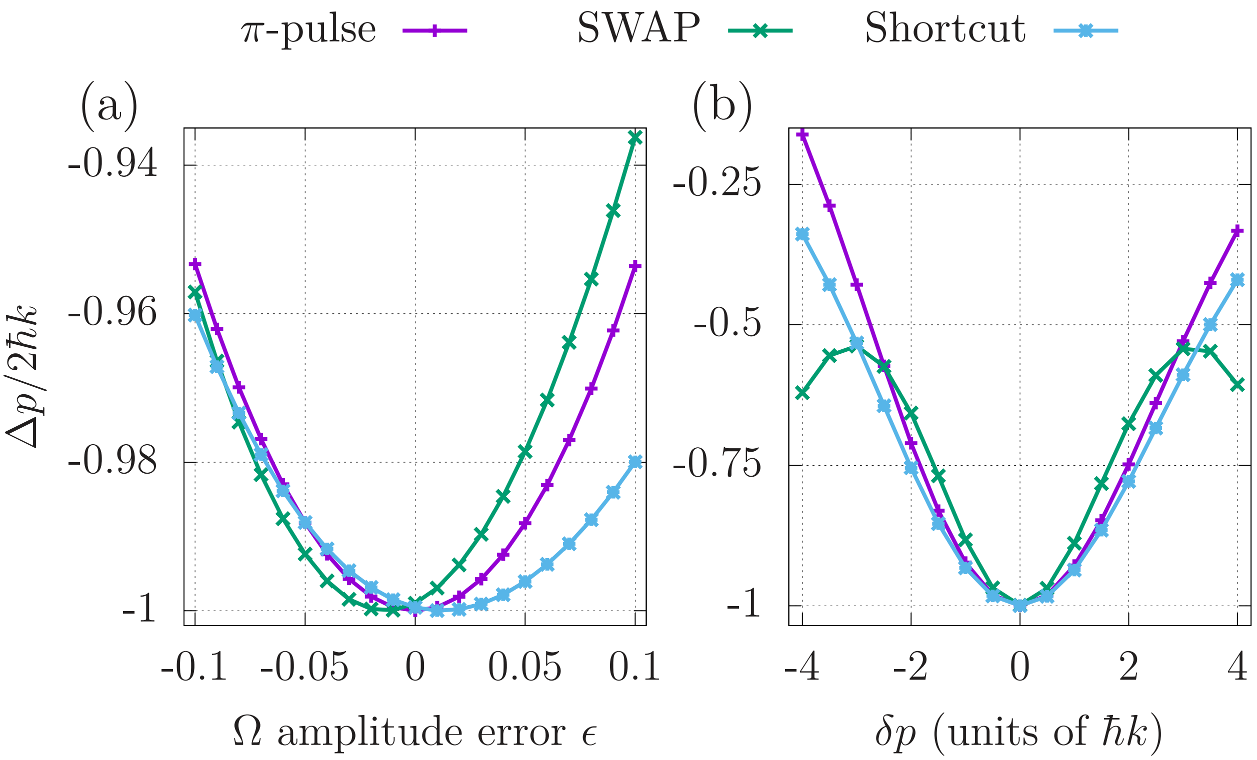

Figure 3.6: Robustness comparison of π-pulse slowing (purple, plus), SWAP slowing (green, cross), and the shortcut scheme (blue, circle with cross) over a $\bar{p} \to \bar{p} - 2\hbar k$ transfer process. Ideally, the resulting impulse $\mathit{\Delta} p$ satisfies $\mathit{\Delta} p/2\hbar k = -1$. The evolution is purely coherent ($\mathit{\Gamma} = 0$), the momentum of the particle (which is addressed by the laser frequencies) is $\bar{p} = 2\hbar k$, and the Rabi frequency is $\mathit{\Omega} = 10\omega_r$ for all processes. (a) Impulse $\mathit{\Delta} p$ experienced by the particle, in units of the ideal impulse magnitude $2\hbar k$, as a function of the error in the Rabi frequency amplitude ϵ [see Eq. (3.53)]. The shortcut scheme is the most robust protocol when $\epsilon > 0$. (b) $\mathit{\Delta} p/2\hbar k$ as a function of the relative momentum of the particle δp with respect to the momentum $\bar{p} = 2\hbar k$ used in the laser frequencies [see Eqs. (3.1) and (3.54)]. For this set of parameters, the shortcut and π-pulse scheme are generally more robust than SWAP slowing. π-pulse parameters are: $T = 0.314/\omega_r$ and $\beta = \pi/2$. SWAP slowing parameters are: $T = 1/\omega_r$ and $\mathit{\Delta}_s = 50\omega_r$. Shortcut parameters are: $T = 0.44/\omega_r$, $\delta_{\text{cut}} = 230\omega_r$, and $\beta = 0.5\,\pi/2$.

a result of high-frequency population oscillations [147], as can be seen in Fig. 2.3. Moreover, when dissipation is included, the much longer SWAP slowing period increases the chance of spontaneous emission, which can disrupt the slowing process. These results demonstrate the utility of the shortcut scheme, as it is robust to small errors ϵ and takes much less time than SWAP slowing. Note that intensity modulators typically have errors less than approximately 5%.

Fig. 3.6(b) presents the effects of applying each slowing method to a particle with a momentum p which is not equal to the momentum $\bar{p}$ accounted for in the laser frequencies [see Eq. (3.1)]. Such an error occurs when slowing a cloud of particles with a distribution of momenta. We parameterize this difference in momentum with the variable δp as:

$$p = \bar{p} + \delta p. \tag{3.54}$$

In this case, we find that the shortcut scheme is most robust for small δp, but SWAP slowing becomes more robust for $|\delta p| > 3\hbar k$. This change in the trend for SWAP slowing near the particular values $\delta p = \pm 3\hbar k$ is due to population oscillations, and the results can again change significantly with small changes in the parameters. In the limit of adiabatic dynamics and time-resolved transfers (which necessarily takes a long time), SWAP slowing is generally most robust to this error since the rate of change of the detuning profile in SWAP slowing is constant, thereby removing the need to align the center of the laser detuning profile with the Doppler shift of the particle. It should be noted that it is not necessarily a major problem that the shortcut scheme is less robust to large deviations of δp from zero because we scan through values of $p/\hbar k$ in integer steps by design. What is more important is that the shortcut scheme is more robust when $|\delta p| < \hbar k$ than SWAP slowing, as particles will not necessarily have integer momentum.

Fig. 3.7 presents the effects of allowing the laser pulses to overlap in time. We define the overlap fraction of the square pulses f such that $f = 0$ when the pulses are completely time-resolved but occur sequentially with no delay, and $f = 1$ when the pulses occur at the same time for the entire pulse duration. We find, in the case of purely coherent dynamics ($\mathit{\Gamma} = 0$), that a pulse overlap fraction as large as $f = 0.2$ does not change the impulse experienced by the particle. In

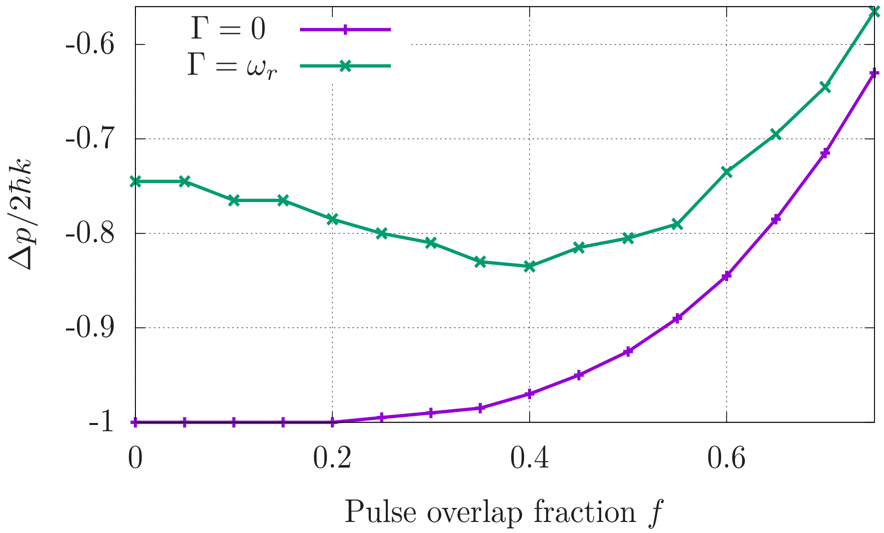

Figure 3.7: Impulse Δp experienced by the particle, in units of the ideal impulse magnitude $2\hbar k$, as a function of the laser pulse overlap fraction f. The impulse is calculated under both coherent ($\Gamma = 0$) and dissipative ($\Gamma = \omega_r$) dynamics. Other parameters are: $T = 0.44/\omega_r$, $\delta_{\text{cut}} = 230\omega_r$, $\Omega = 10\omega_r$, $\bar{p} = 2\hbar k$, and $\beta = 0.5\,\pi/2$. All points are averaged over 1,000 trajectories.

the case of dissipative dynamics, we find that there is an optimal f that maximizes the impulse Δp. This optimal f, which depends on system specifics, must be small enough to allow for full population transfer to $|e\rangle$ before the transfer back to $|g\rangle$, but large enough to minimize the time the particle spends in the excited state, thereby minimizing the chance of spontaneous emission. It should be noted that a pulse overlap introduces the possibility of multiphoton, or Doppleron, resonances [101] which may interfere with the single-photon slowing dynamics.

When slowing a particle with a large initial momentum $p \gg \hbar k$ to rest, we emphasize that the slowing efficiency is significantly affected by even a small deviation from the ideal impulse $\Delta p = -2\hbar k$ since the error compounds exponentially with the number of transfer processes, and the particle is generally not transferred back to $|g\rangle$ for the next pulse sequence. It may be possible to further enhance the robustness of the slowing protocol to the rapidly changing detuning profile at the beginning and end of the transfers by using a Rabi frequency profile that satisfies $\Omega(t_0) = \Omega(t_f) \to 0$, such as a Gaussian or a sinusoidal function [124, 100, 129]. However, in order to satisfy the auxiliary equations and boundary conditions, the peak Rabi frequency may need to be larger than what we considered here.

We have now demonstrated how adiabatic shortcuts may be used to exert immense forces in order to remove a substantial fraction of a particle's kinetic energy. However, the scattering rate Eq. (3.45) for this time-ordered protocol is high as the particle spends half of the slowing protocol in its excited state. This problem can somewhat be overcame using the overlap strategy just discussed. We now turn to another slowing scheme that utilizes the LRI shortcut methods with the focus of limiting the excited state population throughout the slowing process by way of two-photon transitions.

3.2 Application to Particle Slowing in Three-Level Atoms

In this section, we consider a similar experimental setup as Section 3.1. However, we now model each particle as a three-level, Λ-system with an excited state $|e\rangle$ and two internal ground states, $|g_1\rangle$ and $|g_2\rangle$ with different magnetic quantum numbers m_F, as depicted in Fig. 3.8. We

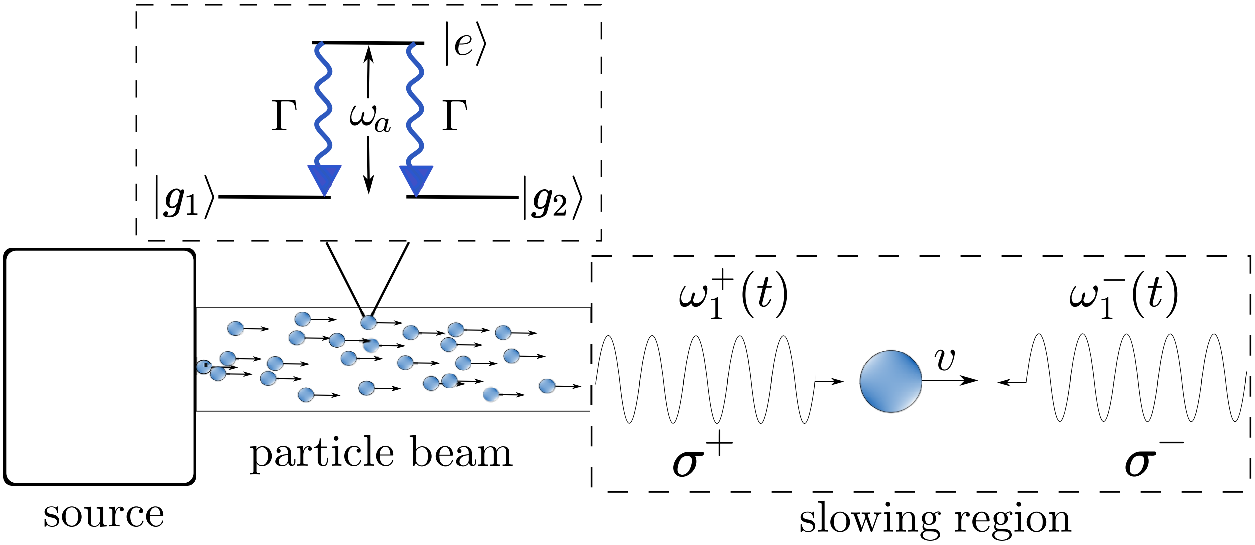

Figure 3.8: Particles exit an atom or molecule source and enter a slowing region. The spatial setup of the counterpropagating lasers, which have time-dependent frequencies $\omega_1^-(t)$ and $\omega_1^+(t)$ and polarizations σ^- and σ^+ for cycle 1, and a sample particle with velocity v in the laboratory frame are displayed in the slowing region. The circular inset shows the three-level internal structure of each particle.

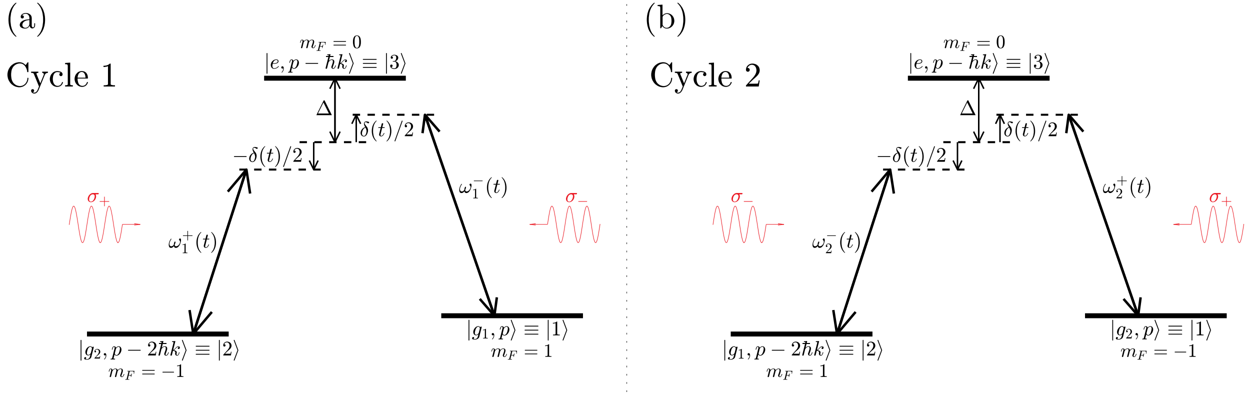

Figure 3.9: The two-cycle process that makes up the slowing scheme with a large detuning from the excited state Δ. The internal states $|e\rangle$, $|g_1\rangle$, and $|g_2\rangle$ have magnetic quantum numbers 0, 1, and -1, respectively. (a) Cycle 1: The counterpropagating (copropagating) laser has polarization σ^- (σ^+) to drive the $|g_1\rangle \to |e\rangle$ ($|e\rangle \to |g_2\rangle$) transition during the two-photon process $|g_1\rangle \to |g_2\rangle$ for an impulse of $\Delta p = -2\hbar k$. (b) The laser polarizations are flipped in order to now drive the $|g_1\rangle \to |g_2\rangle$ transition with another impulse of $\Delta p = -2\hbar k$.

speed up a two-photon Raman transition between the internal ground states that results in an impulse of $\Delta p = -2\hbar k$. Here, the magnetic quantum number of $|e\rangle$, $|g_1\rangle$, and $|g_2\rangle$ are 0, 1, and -1, respectively, which could represent, for example, hyperfine split states. Moreover, the lasers are no longer time-ordered to drive the transition, nor are they linearly polarized in order to avoid multi-photon physics at Doppleron resonances that may interfere with the slowing dynamics. Here, multi-photon physics refers to transitions between motional states within the individual ground state manifolds (i.e., $|g_i, p_1\rangle \to |g_i, p_2\rangle$) which is now forbidden due to conservation of angular momentum [42], as the circularly polarized photons have angular momentum of $\pm\hbar$ [20]. Multi-photon transitions between the two ground state manifolds can occur when the counterpropagating lasers have opposite polarizations. Assuming the particle begins in $|g_1\rangle$, the counterpropagating (copropagating) has circular polarization σ^- (σ^+) for the $|g_1\rangle \to |g_2\rangle$ transition during transfer 1, which is switched to σ^+ (σ^-) during transfer 2 from $|g_2\rangle$ back to $|g_1\rangle$, as shown in Fig. 3.9. This will ensure that each two-photon transition causes a $2\hbar k$ momentum impulse opposite the direction of the particle's motion during both cycles, and the two cycles are repeated until the particle reaches zero momentum.

The main advantage of the use of multi-photon transitions to reduce the particle's momentum is that the particle remains, for the most part, in the ground state manifol which virtually eliminates the incoherent scattering of photons during the slowing process. This assumes that the laser fields are far-detuned from atomic resonance, so that single-photon transitions become negligible. Another obvious advantage of the two-photon transition is that it results in a change of momentum of $2\hbar k$ after each sweep, rather than just $\hbar k$ in the single-photon case considered in Section 3.1 and radiation pressure methods. I begin this section by presenting the Λ-configuration's model, preform an adiabatic elimination of the excited state, and applying the LRI adiabatic shortcut to the acquired effective Hamiltonian. I follow this with an examination of the slowing dynamics in classical phase space. I conclude by studying an application of the LRI Raman transition slowing scheme to a Gaussian momentum distribution.

3.2.1 Model

We again track the dynamics in momentum space, where we assume that the motion is one-dimensional with position and momentum operators $\hat{z}$ and $\hat{p}$. The thermal beam of particles exit the source with an initial average velocity $\bar{v}_0$ and enter a slowing region where they undergo a series of Raman transitions driven by counterpropagating lasers. The ideal slowing process is shown in Fig. 3.9 and is described by the following: A particle begins in $|g_1\rangle$ and in the central momentum state $|\zeta_0\rangle$, where $\hat{p}\,|\zeta_0\rangle = \zeta_0\hbar k\,|\zeta_0\rangle = \bar{p}_0\,|\zeta_0\rangle$ is a momentum eigenstate. Far-detuned, counter-propagating lasers with opposite circular polarizations drive the $|g_1, \zeta_0\rangle \rightarrow |g_2, \zeta_0 - 2\rangle$ transition with little excited state population throughout the process. Here, the counterpropagating (copropagating) laser has polatization σ^- (σ^+) to ensure that it causes stimulated absorption from the counterpropagating beam and stimulated emission into the copropagating beam. Once the population is entirely in $|g_2\rangle$, the lasers' polarizations are exchanged and drive the $|g_2, \zeta_0 - 2\rangle \rightarrow |g_1, \zeta_0 - 4\rangle$ transition. The two cycles are repeated down the dispersion curve until it reaches zero momentum.

3.2.1.1 System Dynamics

The two internal ground states are assumed to be energetically degenerate, $E_{g_1} = E_{g_2}$, and thus both separated from the excited state by a frequency ω_a. We assume that the decay channels from the excited state to the two ground states in the $\mathit{\Lambda}$-transition have equal branching ratios, which is modeled by having the same linewidth $\mathit{\Gamma}$. Furthermore, we assume that the lasers are intensity locked,

$$\mathit{\Omega}_1(t) = \mathit{\Omega}_2(t) \equiv \mathit{\Omega}(t), \tag{3.55}$$

for the ease of both analytical calculations and of experimental implementation. Note that this differentiates our mechanism from stimulated Raman adiabatic passage (STIRAP) and its adiabatic shortcuts, such as the application of Berry's TQD in [30].

During cycle 1, the laser frequencies, addressing the Doppler shifts of the momentum state ζ, are given by

$$\begin{aligned} \omega_1^-(\zeta,t) &= \omega_a - \mathit{\Delta} + \frac{\delta(t)}{2} + \omega_r(1-2\zeta), \\ \omega_1^+(\zeta,t) &= \omega_a - \mathit{\Delta} - \frac{\delta(t)}{2} + \omega_r(2\zeta-3), \end{aligned} \tag{3.56}$$

where ω_1^- and ω_1^+ are the counterpropagating and copropagating laser frequencies, respectively, $\mathit{\Delta} = \text{const}$ is both lasers' large detuning from the respective single-photon resonance, and $\delta(t) \ll \mathit{\Delta}$ is a small detuning from $\mathit{\Delta}$ that will be determined via the LRI shortcut method. This is followed by cycle 2, where the laser polarizations are switched and momentum number is updated from ζ to $\zeta - 2$:

$$\begin{aligned} \omega_2^+(\zeta-2,t) &= \omega_a - \mathit{\Delta} + \frac{\delta(t)}{2} + \omega_r(-3-2\zeta), \\ \omega_2^-(\zeta-2,t) &= \omega_a - \mathit{\Delta} - \frac{\delta(t)}{2} + \omega_r(2\zeta-7), \end{aligned} \tag{3.57}$$

such that ω_2^+ and ω_2^- are the counterpropagating and copropagating laser frequencies, respectively.

Defining the energy to be zero at the ground states, $E_{g_1} = E_{g_2} = 0$, the Hamiltonian of the composite Hilbert space is given by

$$\hat{H}_1(\zeta,t) = \frac{\hat{p}^2}{2m} + \hbar\omega_a \left|e\right\rangle\!\left\langle e\right| + \frac{\hbar\mathit{\Omega}(t)}{2}\left(\left|g_1\right\rangle\!\left\langle e\right| e^{i\left[k\hat{z}+\eta_1^-(\zeta,t)\right]} + \left|g_2\right\rangle\!\left\langle e\right| e^{-i\left[k\hat{z}-\eta_1^+(\zeta,t)\right]} + \text{H.c.}\right), \tag{3.58}$$

where the accumulated phase of each laser is

$$\eta_i^{\pm}(\zeta, t) \equiv \int_{t_0}^{t} \omega_i^{\pm}(\zeta, t')\, dt'. \tag{3.59}$$

We now transform into the interaction picture defined by

$$\hat{H}_0(\zeta, t) = \frac{\hat{p}^2}{2m} + \hbar\left[\frac{\omega_1^-(\zeta, t) + \omega_1^+(\zeta, t)}{2} + \omega_r\right] |e\rangle\langle e| + \frac{\hbar[\delta(t) + 4\omega_r]}{2}\left(|g_2\rangle\langle g_2| - |g_1\rangle\langle g_1|\right), \tag{3.60}$$

which results in an interaction Hamiltonian of

$$\begin{aligned}\tilde{\hat{H}}_1(\zeta, t) =& \hbar\varDelta\, |e\rangle\langle e| + \frac{\hbar[\delta(t) + 4\omega_r]}{2}\left(|g_1\rangle\langle g_1| - |g_2\rangle\langle g_2|\right)\\ &+ \frac{\hbar\varOmega(t)}{2}\Big(\, |g_1\rangle\langle e|\, e^{i\left(k\left[\hat{z}+\frac{\hat{p}t}{m}\right]+\eta_1^-(\zeta,t)-\omega_a t+t\varDelta-\frac{\theta}{2}-2\omega_r t\right)}\\ &+ |g_2\rangle\langle e|\, e^{-i\left(k\left[\hat{z}+\frac{\hat{p}t}{m}\right]-\eta_1^+(\zeta,t)+\omega_a t-t\varDelta-\frac{\theta}{2}-2\omega_r t\right)} + \text{H.c.}\Big).\end{aligned} \tag{3.61}$$

Here, we have defined $\omega_a - \varDelta = \left[\omega_1^-(\zeta, t) + \omega_1^+(\zeta, t)\right]/2 + \omega_r$ and

$$\theta_1(\zeta, t) \equiv \eta_1^-(\zeta, t) - \eta_1^+(\zeta, t) = \theta(t) - 4\omega_r(\zeta - 1)\, t, \tag{3.62}$$

where $\theta(t)$ is the accumulated phase of of the small $\delta(t)$ detunings. We note that

$$\begin{aligned}\omega_r + 2\hat{\zeta}\omega_r + \omega_r(1 - 2\zeta) - 2\omega_r &= 2\omega_r(\hat{\zeta} - \zeta) = k\left(\frac{\hat{p}}{m} - \bar{v}\right),\\ \omega_r - 2\hat{\zeta}\omega_r + \omega_r(2\zeta - 3) + 2\omega_r &= -2\omega_r(\hat{\zeta} - \zeta) = -k\left(\frac{\hat{p}}{m} - \bar{v}\right),\end{aligned} \tag{3.63}$$

with $\hat{\zeta} = \hat{p}/\hbar k$ and $\bar{v} = \zeta\hbar k/m$. This allows us to rewrite Eq. (3.61) as

$$\begin{aligned}\tilde{\hat{H}}_1(\zeta, t) =& \hbar\varDelta\, |e\rangle\langle e| + \frac{\hbar[\delta(t) + 4\omega_r]}{2}\left(|g_1\rangle\langle g_1| - |g_2\rangle\langle g_2|\right)\\ &+ \frac{\hbar\varOmega(t)}{2}\left(|g_1\rangle\langle e|\, e^{ik\hat{z}} e^{i\hat{\varphi}(\zeta,t)} + |g_2\rangle\langle e|\, e^{-ik\hat{z}} e^{-i\hat{\varphi}(\zeta,t)} + \text{H.c.}\right),\end{aligned} \tag{3.64}$$

where we defined $\hat{\varphi}(\zeta, t) \equiv k\left(\hat{p}/m - \bar{v}\right) t$. This is the Hamiltonian we use for cycle 1 in our numerical simulations presented Section 3.2.3. By moving into a similar interaction picture as Eq. (3.60), but with an opposite sign on the final term, we arrive at the interaction Hamiltonian for cycle 2,

$$\begin{aligned}\tilde{\hat{H}}_2(\zeta, t) =& \hbar\varDelta\, |e\rangle\langle e| - \frac{\hbar[\delta(t) + 4\omega_r]}{2}\left(|g_2\rangle\langle g_2| - |g_1\rangle\langle g_1|\right)\\ &+ \frac{\hbar\varOmega(t)}{2}\left(|g_1\rangle\langle e|\, e^{-ik\hat{z}} e^{-i\hat{\varphi}(\zeta,t)} + |g_2\rangle\langle e|\, e^{ik\hat{z}} e^{i\hat{\varphi}(\zeta,t)} + \text{H.c.}\right).\end{aligned} \tag{3.65}$$

3.2.1.2 Adiabatic Elimination of Excited State

Focusing on cycle 1, we now, once again, isolate our analysis to a subset $W_1(\zeta)$ of the full composite Hilbert space:

$$W_1(\zeta) = \{|g_1, \zeta\rangle, |g_2, \zeta - 2\rangle, |e, \zeta - 1\rangle\} \equiv \{|1\rangle, |2\rangle, |3\rangle\}. \tag{3.66}$$

In this subsystem, the cycle 1 Hamiltonian Eq. (3.64) is given by

$$\begin{aligned}\hat{H}_1^{(W)}(\zeta, t) =& \hbar\varDelta\,|3\rangle\langle 3| + \frac{\hbar\,[\delta(t) + 4\omega_r]}{2}\left(|1\rangle\langle 1| - |2\rangle\langle 2|\right) \\ &+ \frac{\hbar\varOmega(t)}{2}\left(|1\rangle\langle 3|\exp\left[i\varphi^{\zeta}_{\zeta-1}(t)\right] + |2\rangle\langle 3|\exp\left[-i\varphi^{\zeta}_{\zeta-1}(t)\right] + \text{H.c.}\right),\end{aligned} \tag{3.67}$$

where $\varphi^{\zeta}_{l}(t) \equiv k\left(l\hbar k/m - \bar{v}\right)t$ for momentum number l. The time-dependent Schrödinger equation with this Hamiltonian and atomic state vector $|\psi(t)\rangle = c_1(t)\,|1\rangle + c_2(t)\,|2\rangle + c_3(t)\,|3\rangle$ results in the following equations of motion:

$$\begin{aligned}\dot{c}_1 &= -\frac{i\,[\delta + 4\omega_r]}{2}c_1 - \frac{i\varOmega}{2}c_3\exp\left[i\varphi^{\zeta}_{\zeta-1}\right], \\ \dot{c}_2 &= \frac{i\,[\delta + 4\omega_r]}{2}c_2 - \frac{i\varOmega}{2}c_3\exp\left[-i\varphi^{\zeta}_{\zeta-1}\right], \\ \dot{c}_3 &= -i\varDelta c_3 - \frac{i\varOmega}{2}\left(c_1\exp\left[-i\varphi^{\zeta}_{\zeta-1}\right] + c_2\exp\left[i\varphi^{\zeta}_{\zeta-1}\right]\right).\end{aligned} \tag{3.68}$$

In the limit $\varDelta \gg \varOmega(t), \delta(t)$, the form of our Hamiltonian places the fast time-dependence on the excited state $|3\rangle$, which allows us to make the approximation that the excited state amplitude damps to equilibrium instantaneously $\dot{c}_3 \approx 0$ [130, Chapter 6]. Thus, we find from Eq. (3.68) that the excited state population can be determined from

$$c_3 \approx -\frac{\varOmega}{2\varDelta}\left(c_1\exp\left[-i\varphi^{\zeta}_{\zeta-1}\right] + c_2\exp\left[i\varphi^{\zeta}_{\zeta-1}\right]\right), \tag{3.69}$$

which predicts the scattering rate

$$R^s = \varGamma_{\text{tot}}\rho_{ee} = 2\varGamma|c_3|^2 \ll \frac{\varGamma}{2}, \tag{3.70}$$

to be very small since $|c_3|^2 \ll 1$ in the limit $\varOmega \ll \varDelta$. Here, we have defined the $\varLambda$-configuration's total decay rate $\varGamma_{\text{tot}}$ given by the sum of each individual channel's rate $\varGamma_{\text{tot}} = \sum_i \varGamma_i = 2\varGamma$. Note that adiabatic elimination of $|3\rangle$ is used only to simplify the mathematical complexity of applying the adiabatic shortcut, and that the excited state manifold will be included in the numerical simulations in subsection 3.2.3.

We now plug Eq. (3.69) into the first two lines of Eq. (3.68) to find an effective Hamiltonian $\tilde{\hat{H}}_{R,1}$ describing the effective two-level evolution of the Raman system formed by $|1\rangle$ and $|2\rangle$ with the result

$$\begin{aligned}\tilde{\hat{H}}_{R,1}(\zeta,t) =& \frac{\hbar\left[\delta(t)+4\omega_r\right]}{2}\left(|1\rangle\langle 1| - |2\rangle\langle 2|\right) + \frac{\hbar\Omega_R(t)}{2}\left(|1\rangle\langle 1| + |2\rangle\langle 2|\right) \\ &+ \frac{\hbar\Omega_R(t)}{2}\Big(|1\rangle\langle 2|\exp\left[2i\varphi^{\zeta}_{\zeta-1}(t)\right] + \text{H.c.}\Big).\end{aligned} \tag{3.71}$$

Here,

$$\Omega_R(t) \equiv -\frac{\Omega^2(t)}{2\Delta} \tag{3.72}$$

is the two-photon Rabi frequency, or Raman Rabi frequency, and $\hbar\Omega_R(t)/2$ is the AC Stark shift. Lastly, we shift the definition of zero energy by the AC Stark shift and move into another rotating frame by use of the interaction picture

$$\tilde{\hat{H}}_0(\zeta,t) = \frac{\hbar\Omega_R(t)}{2}\left(|1\rangle\langle 1| + |2\rangle\langle 2|\right) + 2\hbar\omega_r\left(|1\rangle\langle 1| - |2\rangle\langle 2|\right), \tag{3.73}$$

resulting in the Raman interaction Hamiltonian for cycle 1:

$$\hat{H}_{R,1}(\zeta,t) = \frac{\hbar\delta(t)}{2}\left(|1\rangle\langle 1| - |2\rangle\langle 2|\right) + \frac{\hbar\Omega_R(t)}{2}\Big(|1\rangle\langle 2|\exp\Big[2i\left(\varphi^{\zeta}_{\zeta-1}(t) + 2\omega_r t\right)\Big] + \text{H.c.}\Big). \tag{3.74}$$

Noting that $\varphi^{\zeta}_{\zeta-1}(t) = k(\zeta\hbar k/m - \bar{v})t - 2\omega_r t$, we can write the final form of the Raman Hamiltonian,

$$\hat{H}_{R,1}(\zeta,t) = \frac{\hbar\delta(t)}{2}\left(|1\rangle\langle 1| - |2\rangle\langle 2|\right) + \frac{\hbar\Omega_R(t)}{2}\left(|1\rangle\langle 2| + \text{H.c.}\right), \tag{3.75}$$

which can be written in matrix notation as

$$\hat{H}_{R,1}(\zeta,t) = \frac{\hbar}{2}\begin{pmatrix} -\delta(t) & \Omega_R(t) \\ \Omega_R(t) & \delta(t) \end{pmatrix}. \tag{3.76}$$

A similar process can be done from cycle 2. We have found that the effective two-level dynamics of the subsystem again takes a similar form to Eq. (2.16), and thus the application of the LRI shortcut protocol will be similar to that given in subsection 3.1.1.3. Here, however, we pursue shortcut solutions with a Gaussian Rabi frequency profile.

3.2.1.3 Shortcut Application and Analytical Solution

We again parameterize the invariant eigenvectors in parallel to the eigenvectos of Eq. (3.75),

$$\begin{aligned} |\phi_+(t)\rangle &= \cos\left(\frac{\gamma}{2}\right) e^{i\beta} |1\rangle + \sin\left(\frac{\gamma}{2}\right) |2\rangle , \\ |\phi_-(t)\rangle &= \sin\left(\frac{\gamma}{2}\right) |1\rangle - \cos\left(\frac{\gamma}{2}\right) e^{-i\beta} |2\rangle , \end{aligned} \tag{3.77}$$

with auxiliary angles $\gamma = \gamma(t)$ and $\beta = \beta(t)$. This leads to the same auxiliary equations as in Eqs. (3.20) and (3.21) when we assume $\beta = \text{const}$:

$$\dot{\gamma} = \mathit{\Omega}_R(t) \sin\beta, \tag{3.78}$$

$$\delta(t) = \mathit{\Omega}_R(t) \cot\gamma \cos\beta, \tag{3.79}$$

We impose the boundary condition defined in Eq. (3.23), as well as those in Eqs. (3.25) and (3.26), so that we drive the system from $|1\rangle$ at t_0 into $|2\rangle$ at t_f via the upper invariant eigenstate $|\phi_+(t)\rangle$.

We are now faced with the task of choosing, from an infinite set of Hamiltonians, a particular form of γ and β that satisfy these boundary conditions. This particular solution is often found by trying a quadratic ansatz for γ and β [32]. However, the resulting laser frequency and intensity profiles may be difficult to implement experimentally, which led to the use of a constant Rabi frequency profile solution in subsection 3.1.1.3. This method also has drawbacks such as a the requirement to maintain a large laser intensity throughout the entire slowing process. This problem is compounded when driving Raman transition as, in the limit $\mathit{\Delta} \gg \mathit{\Omega}(t)$, the maximum single-photon Rabi frequency will be large compared to the Raman Rabi frequency that is found from the shortcut method $\mathit{\Omega}(t) \gg \mathit{\Omega}_R(t)$ [see Eq. (3.72)]. I now present an analytical solution that can produce experimentally implementable solutions, such as Gaussian Rabi frequency profiles, that may be advantageous when considering these issues.

Let us define a time-dependent function $f(t)$ such that

$$\mathit{\Omega}_R(t) = \mathit{\Omega}_0 f(t), \tag{3.80}$$

with a frequency constant $\mathit{\Omega}_0$. Plugging this into Eq. (3.78) and integrating, we find (noting

$\beta = \text{const}$),

$$\gamma(t) = \Omega_0 \sin\beta \int_{t_0}^{t} f(t')dt', \tag{3.81}$$

to which we apply the boundary condition Eq. (3.23) to arrive at

$$\Omega_0 \sin\beta \int_{t_0}^{t_f} f(t')dt' = \pi. \tag{3.82}$$

The second auxiliary equation Eq. (3.79) then reads

$$\delta(t) = \Omega_0 f(t) \cos\beta \cot\left(\Omega_0 \sin\beta \int_{t_0}^{t} f(t')dt'\right). \tag{3.83}$$

Suppose, for example, we choose $\Omega_R(t)$ to have a Gaussian waveform. We also assume the single-photon Rabi frequencies to be real $\Omega(t) = \Omega(t)^*$. Therefore, we impose $\Omega_0 \leq 0$ [see Eq. (3.72)] and

$$f(t) = e^{-t^2/\tau^2}, \tag{3.84}$$

where $\tau > 0$ is a time constant and $t_0 = -t_f$. This choice gives

$$\gamma(t) = \sqrt{\pi} \sin\beta \frac{\Omega_0 \tau}{2}\left[\operatorname{erf}\left(\frac{t}{\tau}\right) - \operatorname{erf}\left(\frac{t_0}{\tau}\right)\right], \tag{3.85}$$

which, in conjunction with Eq. (3.82), allows us to derive the minimum Raman Rabi frequency

$$\Omega_0 = \Omega_R(0) = \sqrt{\pi}\left(\tau \sin\beta \operatorname{erf}\left[\frac{T}{2\tau}\right]\right)^{-1} < 0, \tag{3.86}$$

for total shortcut time $T = 2t_f$. Here, we have used the error function erf. The condition $\Omega_R(t) \leq 0$ imposes $\beta \leq 0$ and Eq. (3.86) shows that the choice of a particular β directly determines the required maximum of the absolute value of the Raman Rabi frequency. This should be minimized for experimental simplicity. A choice that minimizes the laser intensity is given by $\beta = (r + \frac{1}{2})\pi$, but again results in a constant detuning (i.e., a Raman π-pulse). Thus, we examine solution in the regime $-\pi/2 \ll \beta < 0$. We also note that Eq. (3.83) becomes

$$\delta(t) = \Omega_0 \cos\beta e^{-t^2/\tau^2} \cot\left(\sqrt{\pi} \sin\beta \frac{\Omega_0 \tau}{2}\left[\operatorname{erf}\left(\frac{t}{\tau}\right) - \operatorname{erf}\left(\frac{t_0}{\tau}\right)\right]\right). \tag{3.87}$$

We again impose a cutoff time t_{cut} to avoid tracking the asymptotic behavior of the detuning [see Eq. (3.48)].

3.2.2 Slowing Dynamics in Classical Phase Space

We now examine the slowing dynamics of the Raman slowing scheme in classical phase space in order to interpret its usefulness. This analysis will be similar to subsection 3.1.4, but now with an impulse of $\Delta p = 2\hbar k$ per sweep as well as factors resulting from the time-dependence of the Rabi frequency. Eq. (3.82) can be written, for the Gaussian solution, as

$$\Omega_0 \sin\beta \operatorname{erf}\left(\frac{G}{2\sqrt{2}}\right) = \sqrt{\frac{\pi}{2}}\frac{G}{T}. \tag{3.88}$$

Here, we have defined $G \equiv \sqrt{2}T/\tau$ and $D \equiv \Omega_{\max}/\Delta$, where $\Omega_{\max}$ is the maximum single-photon Rabi frequency,

$$\Omega_{\max} = \Omega(0) = \sqrt{-2\Delta\Omega_0}. \tag{3.89}$$

The variable G measures the total number of standard deviations of the Rabi frequency profile that is used during each sweep, which must be large to approximately satisfy Eqs. (3.25) and (3.26). For the adiabatic elimination of the excited state to remain valid, the condition $D \ll 1$ must be satisfied.

We use Eq. (3.88) to calculate the classical force exerted of the particle during each sweep,

$$F_{\mathrm{LRI}} = \frac{2\hbar k}{T} = \sqrt{\frac{2}{\pi}}\frac{2\hbar k\Omega_0}{G}\sin\beta \operatorname{erf}\left(\frac{G}{2\sqrt{2}}\right). \tag{3.90}$$

We assume that $D = \text{const}$ which implies, from Eq. (3.89), that the force scales with $\Omega_{\max}$. We now use the force to derive the associated slowing distance of the Raman slowing protocol.

The particle begins the process in the state $|g_1, \zeta_0\rangle$ and we again approximate the momentum to be linear

$$p(t) \approx \hbar k\left(\zeta_0 - \frac{2t}{T}\right), \tag{3.91}$$

so that we may write

$$\Delta x_{\mathrm{LRI}} = \frac{p_{\mathrm{avg}}}{m}\Delta t = \frac{T\omega_r\zeta_0^2}{4\pi}\lambda, \tag{3.92}$$

where we have used $p_{\mathrm{avg}} = \zeta_0\hbar k/2 = \zeta_0 m\omega_r/k$ and $\Delta t = \zeta_0 T/2$. Using Eq. (3.88), we write this in terms of the Raman Rabi frequency as

$$\Delta x_{\mathrm{LRI}} = \sqrt{\frac{1}{2\pi}}\frac{G\omega_r\zeta_0^2\lambda}{4\Omega_0}\left[\sin\beta \operatorname{erf}\left(\frac{G}{2\sqrt{2}}\right)\right]^{-1} \propto \frac{\zeta_0^2\omega_r\lambda}{|\Omega_0|}. \tag{3.93}$$

We can compare this quantity to the corresponding expression for radiation pressure [see Eq. (3.44)] by computing the ratio

$$\frac{\mathit{\Delta} x_{\mathrm{LRI}}}{\mathit{\Delta} x_{\mathrm{RP}}} = \frac{\rho_{ee}\mathit{\Gamma}_{\mathrm{tot}}T}{2} \propto \frac{\rho_{ee}\mathit{\Gamma}}{|\mathit{\Omega}_0|}, \tag{3.94}$$

where we have used the $\mathit{\Lambda}$-configuration's total decay rate $\mathit{\Gamma}_{\mathrm{tot}} = 2\mathit{\Gamma}$ in our $\mathit{\Delta} x_{\mathrm{RP}}$ calculation for a sensible comparison between schemes. We once again find that our scheme significantly reduces the slowing distance when $|\mathit{\Omega}_0| \gg \mathit{\Gamma}$ and $D \ll 1$ or, more specifically, when $\mathit{\Delta} \gg \mathit{\Omega}_{\max} \gg \mathit{\Gamma}$. Since the excited state population is minimal in the Raman slowing scheme, its number of scattered photon is on order of unity or less, which is a massive improvement to the approximately ζ_0 scattered photons for RP.

3.2.3 Slowing Example

By repeatedly driving the two-photon transition $|g_i, \zeta\rangle \rightarrow |g_j, \zeta - 2\rangle$ according to our Raman shortcut solution, we now show that we are able to generate an impulse of $2N\hbar k$ against the particle's motion in N sweeps with an engineered excited state linewidth. Compared to slowing processes that rely on radiation pressure such as the Zeeman slower, our procedure significantly reduces the number of scattered photons which can be crucial for slowing atoms and molecules that lack closed cycling transitions. To exemplify our slowing scheme, we simulate the results of applying the analytic solution developed in subsection 3.2.1.3 to a specific momentum family $W_1(\zeta)$ when we track a large subset of the composite Hilbert space. After each cycle, we flip the laser polarizations and update the momentum number we are tracking $\zeta \rightarrow \zeta - 2$ as we assume the initial population in the first ground state has fully transferred to the other ground state.

The incoherent dynamics of our system are governed by the master equation Eq. (3.33) with, in a similar fashion as Eq. (3.36), six decay channels for each momentum state:

$$\begin{aligned} \hat{C}_{1,0}^{(\zeta)} &= \sqrt{\frac{3\mathit{\Gamma}}{5}}\, |g_1\rangle\langle e| \otimes |\zeta\rangle\langle\zeta|\,, \hat{C}_{1,-}^{(\zeta)} = \sqrt{\frac{\mathit{\Gamma}}{5}}\, |g_1\rangle\langle e| \otimes |\zeta-1\rangle\langle\zeta|\,, \hat{C}_{1,+}^{(\zeta)} = \sqrt{\frac{\mathit{\Gamma}}{5}}\, |g_1\rangle\langle e| \otimes |\zeta+1\rangle\langle\zeta|\,, \\ \hat{C}_{2,0}^{(\zeta)} &= \sqrt{\frac{3\mathit{\Gamma}}{5}}\, |g_2\rangle\langle e| \otimes |\zeta\rangle\langle\zeta|\,, \hat{C}_{2,-}^{(\zeta)} = \sqrt{\frac{\mathit{\Gamma}}{5}}\, |g_2\rangle\langle e| \otimes |\zeta-1\rangle\langle\zeta|\,, \hat{C}_{2,+}^{(\zeta)} = \sqrt{\frac{\mathit{\Gamma}}{5}}\, |g_2\rangle\langle e| \otimes |\zeta+1\rangle\langle\zeta|\,. \end{aligned} \tag{3.95}$$

We again simulate the incoherent dynamics by way of Monte Carlo wave functions (see Appendix C.2) over many trajectories to ease the numerical complexity.

An example of our Raman LRI slowing scheme over 200 sweeps is shown in Fig. 3.10 and discussed below. The momentum distribution of the ensemble of particles is initialized as a Gaussian profile (purple line) with a standard deviation $\sigma_{p,0} = 50\hbar k$ centered at $\bar{p}_0 = 400\hbar k$. We choose the center of the Gaussian distribution to be our central momentum state to account for the Doppler shifts, $\zeta_0 = 400/\hbar k$. We first apply $\hat{H}_1(\zeta, t)$ to the full, composite Hilbert space, followed by the application of $\hat{H}_2(\zeta - 2, t)$, and then $\hat{H}_1(\zeta - 4, t)$ and so on until the slowed momentum packet reaches zero average momentum. Fig. 3.10 presents snapshots of the momentum distribution after 50 (green distribution), 100 (blue distribution), 150 (yellow distribution), and 200 (red distribution) cycles of our slowing scheme. The applied laser detuning and Raman Rabi frequency profiles are determined through the adiabatic shortcut by Eqs. (3.84), (3.86), and (3.87), which we plot for our chosen parameters in Fig 3.11. We note that our choice of $\beta = -\pi/4$ satisfies the inequality given in the text before Eq. (3.87).

We find that about 4% of the initial momentum distribution has been slowed to around zero momentum at the conclusion of the slowing process, as shown by the red spike near 0 in Fig. 3.10. There is only an average of 0.18 scattered photons per particle throughout the slowing scheme, which is in stark contrast to the $\mathcal{O}(\zeta_0)$ scattered photons in radiation pressure schemes, as well as an order of magnitude improvement over the single-photon slowing scheme presented in subsection 3.1.5. This comes at the cost of a larger single-photon Rabi frequency which may be difficult to create experimentally, although some possible solutions to this problem are discussed in Section 3.3. Furthermore, we note that our choice of shortcut time, $T = 0.1/\omega_r$, is typically much shorter than the associated timescale of radiation pressure, and thus slowing occurs in a much shorter distance (see subsection 3.2.2).

We can calculate the 1D temperature T_f of the final, slowed momentum packet,

$$\frac{1}{2}k_B T_f = \frac{\langle \hat{p}^2 \rangle}{2m} \approx \frac{\sigma_{p,f}^2}{2m}, \tag{3.96}$$

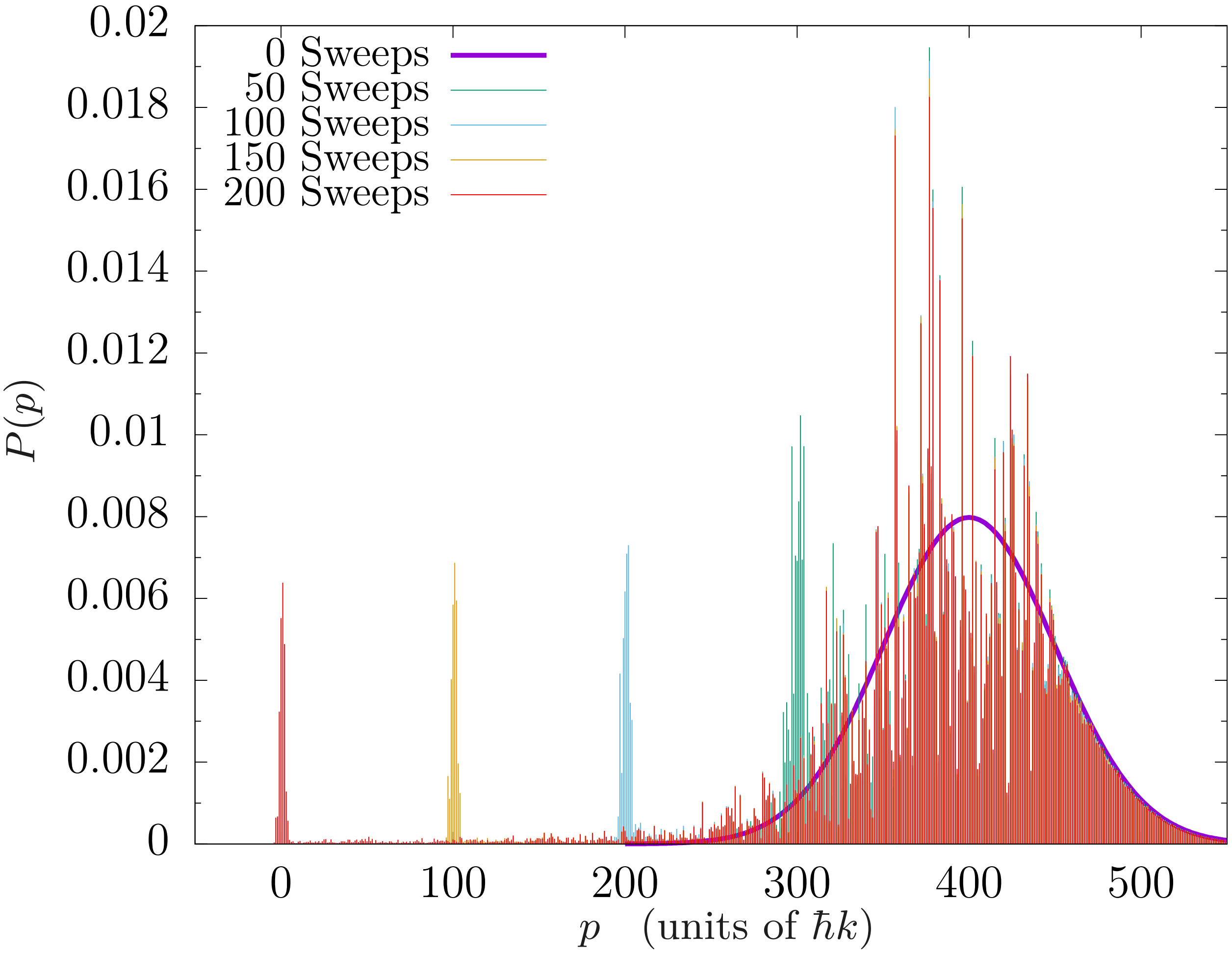

Figure 3.10: Sanpshots of the momentum distribution $P(p)$ of the system at different times throughout the slowing process. The system is initialized (purple line) in a Gaussian state with average momentum $\langle \hat{p} \rangle = 400\hbar k$ and width $\sigma_p = 50\hbar k$. Snapshots of the momentum distribution at 50 (green distribution), 100 (blue distribution), 150 (gold distribution), and 200 sweeps (red distribution) are shown. The other parameters are: $\varGamma = \omega_r$, $\varDelta = 5000\omega_r$, $\beta = -\frac{\pi}{4}$, $\delta_{\text{cut}} \approx 89\omega_r$, $\tau = 0.025/\omega_r$, and $T = 0.1/\omega_r$, which leads to a maximum Rabi frequency of $\varOmega_{\max} \approx 1004\omega_r$. Results are averaged over 500 trajectories.

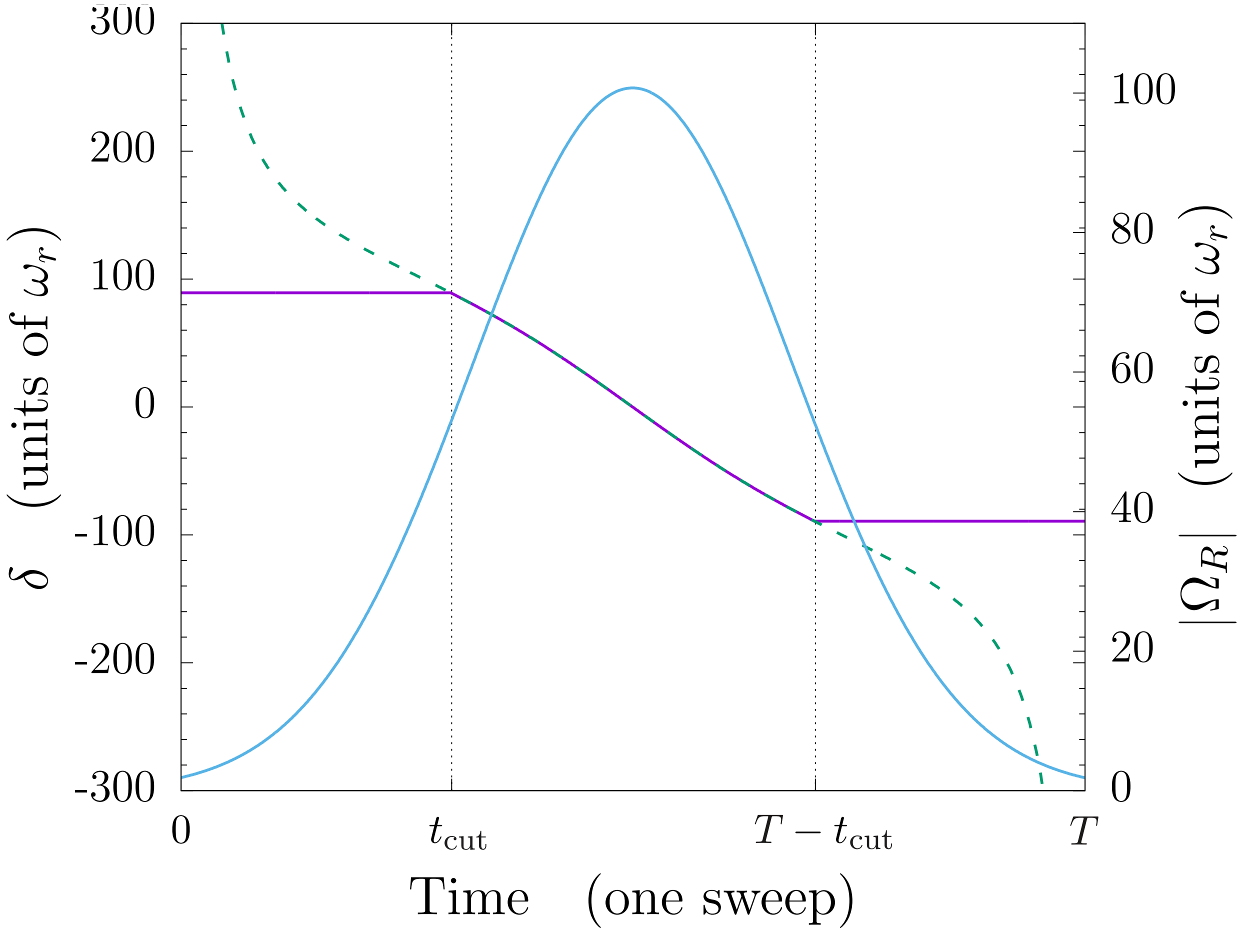

Figure 3.11: The detuning profile (dashed green curve) and the absolute value of the Raman Rabi frequency profile (blue curve) over a single sweep. Also displayed is the cutoff scheme for the detuning profile at cutoff time t_{cut} (purple curve). The parameters are: $\mathit{\Delta} = 5000\omega_r$, $\beta = -\frac{\pi}{4}$, $\delta_{\mathrm{cut}} \approx 89\omega_r$, $\tau = 0.025/\omega_r$, and $T = 0.1/\omega_r$.

where k_B is Boltzmann's constant. Here, $\sigma_{p,f}$ is the variance in p of the final momentum packet which we calculate using a Gaussian fit of the final momentum distribution in the range $-15 \leq \zeta \leq 15$. We find that, for the example given in Fig. 3.10, the final distribution has a temperature of $T_f \approx 5T_r$, where $k_B T_r = \hbar\omega_r$ is the recoil temperature. We note that the slowed packet of particles will spread out in position space during the slowing process, so phase space compression, and thus cooling, does not occur. However, this final momentum packet is now in a suitable state to be trapped and cooled. We turn our attention to laser cooling in the next chapter.

3.3 Outlook

By periodically modifying the frequency and intensity profiles of counterpropagating lasers based on the LRI shortcut protocol, we have created a novel slowing scheme that has the potential to generate a large classical force against the motion of a thermal beam of particles. The coherent nature of our scheme allows for a very low scattered photon number and can greatly reduce the slowing distance compared to radiation pressure techniques for narrow-line transitions or systems that lack a closed cycling transition. We also demonstrated that our slowing blueprint has advantages over adiabatic and purely resonant schemes. We presented an operating regime for our slowing schemes, which we showed to be when the maximum Rabi frequency is much larger than the linewidth. The use of a ring-cavity may be used to achieve such high laser intensities [61], which is a particularly important consideration in implementing the Raman slowing scheme.

A possible practical implementation of our scheme is to directly apply it to a particle beam exiting a supersonic nozzle or buffer gas cell. Our scheme may also be utilized as a second slowing stage after particles exiting an effusive oven have been slowed in a precursor stage to the order of 10 m/s and the initial spread in velocity has been greatly reduced. Additionally, it may be possible to implement our protocol as a steady-state slowing procedure by compensating for the changing particle velocity with a magnetic field gradient instead of the time-dependent laser frequencies, in a similar approach to a Stark or Zeeman decelerator. This has the potential to greatly increase the slowing blueprint's capture range and is an enticing candidate for future work.

A natural next step would be to optimize our shortcut solutions with respect to different criteria. Time-optimization of different adiabatic shortcuts has been studied previously for two-level systems [118, 119], STIRAP [103], and frictionless cooling in harmonic traps [131]. Additionally, quantum optical control based protocols could be implemented to derive further solutions [58]. Another optimization criterion comes from the fact that adiabatic shortcuts cannot be implemented without an energetic cost, an intrinsic relationship that has been rigorously studied for various shortcuts [26, 1, 41], as noted in subsection 2.4.1. Thus, minimizing the energetic cost for a fixed sweep period is, in effect, finding the most efficient shortcut.

Furthermore, it is impossible to implement the LRI scheme to the entire momentum Hilbert space by hand. An intriguing possible solution to this problem is to employ advanced optimization techniques, such as quantum optimal control and reinforcement learning, to find a solution that maximizes the slowing scheme's capture range or minimizes the energetic cost of implementing the shortcut for a given sweep period.

There are similarities between our results and others [124, 83, 100, 129] in the sense that two-level inversion is achieved in the diabatic limit. A more thorough investigation could further our understanding of the connection between these solutions and adiabatic shortcuts.

Having successfully slowed a substantial fraction of the momentum distribution to near zero momentum with a low velocity spread, the final packet of particles is now in a position to be loaded into an electromagnetic trap. Here, the particles are then trapped and cooled to both a low temperature and low entropy state. Such is the study of the next chapter.

Chapter 4

Entropy Removal by a Laser Field

As mentioned in Section 3.2.3, the slowing schemes developed in the previous chapter does not lead to entropy removal. To see this, we can quantify the entropy S of a system by identifying the volume it occupies in a phase space consisting of pairs of conjugate variables. The slowing schemes considered in Chapter 3 only produce a translation in momentum space, and therefore do not lead to phase space compression. However, the final slowed state is in an ideal position to be trapped and cooled in which the entropy of the particle cloud can be reduced.

We now expand on the idea of phase space compression. While the total phase space volume must be conserved, the volume can be redistributed so that a subspace can experience phase space compression [50]. In the language of open quantum systems (see Appendix C), the system subspace deposits its entropy into the degrees of freedom of an external reservoir so that it may reduce its entropy without violating the second law of thermodynamics [50, 115].

Our particular interest is entropy transfer in the process of laser cooling and trapping where the atomic gas redistributes the photons of a coherent laser field while spontaneous emission into the background radiation field is possible. The compression of the atomic phase space, as the cloud's spread in both momentum and position is reduced, decreases both the entropy and the temperature of the atomic subspace. It is often assumed that the only subspace that is suitable to absorb the entropy lost by the atomic subsystem is the radiation field via the spontaneous emission process. As Wolfgang Ketterle stated in his Nobel lecture [72]:

> Real cooling needs an open system which allows entropy to be removed from the

system – in laser cooling, in the form of scattered photons.

This commonly accepted explanation lies in the fact that the reservoir can absorb a substantial amount of entropy due to the large number of possible configurations of the outgoing light, such as various frequencies, polarizations, and direction [96, Chapter 5, §1]. Furthermore, it is often assumed that the state of the laser field is not significantly perturbed, and therefore can not remove entropy from the gas. However, there are some studies that predict entropy removal from the gas via interaction with the laser field [76, 94, 40, 29, 99].

To investigate this point, we propose a simple gedanken experiment that probes the change in the state of a laser field that interacts with a system with non-zero initial entropy. We begin this chapter with a condensed background on quantum statistical mechanics and Fock space, preliminaries necessary for understanding the usefulness of our approach. We then further motivate the possibility of entropy transfer to the laser fields in Section 4.2, and we propose a gedankan experiment to test our rationale. In Section 4.3, we present the model of our gedankan experiment, followed by an analysis of the time evolution of the cavity field. Our main results are presented in Sections 4.5 and 4.6 where we provide both an experimental and a theoretical approach to quantify the entropy exchange between the laser and atomic cloud.

4.1 Preliminary Information

4.1.1 Quantum Statistical Mechanics Background

In Section 2.4.1, we introduced the density matrix $\hat{\rho}$ to map a pseudo-spin $\frac{1}{2}$ system to the three dimensional Bloch vector representation. We saw further usefulness of the density matrix in Section 3.1.3 as the dynamics of the system subspace is governed by the quantum master equation Eq. (3.33) under the Born-Markov approximation. Let us now generalize our conversation of density matrices as they are critical for representing *mixed ensembles*. Here, all of the members of the ensemble can not be characterized by a single ket which undergoes Schrödinger dynamics. Throughout the last chapter, this statistical mixture arose because the randomness of the system's incoherent dynamics. This can be thought of in a quantum trajectories picture as the jump operator associated with spontaneous emission being applied to particles at different times, resulting in different final states.

We can write the density matrix for an arbitrary mixed ensemble as

$$\hat{\rho}(t) = \sum_i w_i \left|\psi^{(i)}\middle\rangle\middle\langle\psi^{(i)}\right|, \tag{4.1}$$

where $\left|\psi^{(i)}\right\rangle$ is a ket that characterizes a fraction of the ensemble's population with weight w_i. The normalization condition is now $\sum_i w_i = 1$. For a pure state, we have $w_j = 1, w_{i\neq j} = 0$ and thus, $\hat{\rho} = |\psi_j\rangle\langle\psi_j|$. To measure the overlap between two systems, we define the fidelity

$$F\left[\hat{\rho}, \hat{\sigma}\right] = \mathrm{Tr}\left[\sqrt{\sqrt{\hat{\rho}}\hat{\sigma}\sqrt{\hat{\rho}}}\right]^2, \tag{4.2}$$

which, using the cyclic property of the trace, reduces to

$$F\left[\hat{\rho}, |\psi_j\rangle\langle\psi_j|\right] = \langle\psi_j|\,\hat{\rho}\,|\psi_j\rangle, \tag{4.3}$$

when $\hat{\sigma}$ is a pure state.

We now define the von Neumann entropy (see [121, Chapter 3, §4])

$$S(\hat{\rho}) = -\,\mathrm{Tr}[\hat{\rho}\ln\hat{\rho}], \tag{4.4}$$

which is written in the diagonal basis of $\hat{\rho}$ as

$$S(\hat{\rho}) = -\sum_i \rho_{ii}\ln\rho_{ii} \geq 0, \tag{4.5}$$

where $\rho_{ii} = \langle i|\,\hat{\rho}\,|i\rangle$, we have set Boltzmann's constant $k_B = 1$, and we have used $0 \leq \rho_{ii} \leq 1$. This is, as traditionally stated, a measure of disorder of which the second law of thermodynamics states will never decrease in the universe. For a pure ensemble, we either have $w_{i\neq j} = 0 \rightarrow \rho_{ii} = 0$ or $w_j = 1 \rightarrow \ln\rho_{jj} = 0$ and thus, the entropy of a pure ensemble is zero:

$$S(|\psi_j\rangle\langle\psi_j|) = 0. \tag{4.6}$$

We can further define the mutual information between two subsystems A and B as

$$I(A:B) = S(\hat{\rho}_A) + S(\hat{\rho}_B) - S(\hat{\rho}_{AB}), \tag{4.7}$$

where one assumes the two systems are uncorrelated and measures the error of that assumption. This therefore expresses how much information is common to both subsystems, which is contained in the total correlations between A and B [107]. This is an important measure when differentiating between entropy that is created during the interaction from entropy that is transferred between subsystems. We use mutual information in Section 4.3 to look at correlations between atoms and a quantized field.

4.1.2 Interactions Between Atoms and Quantized Fields

In Chapters 2 and 3, we treated the laser field as a purely classical electric field [see Eq. (A.1)]. However, the situation often arises when an electromagnetic field must also be treated quantum mechanically – that is, as a collection of identical particles of light called photons. Such a situation occurs when considering a quantum gases inside of a *cavity*: two mirrors that form an optical resonator that allows for stable, contained, standing-wave modes of oscillation.

4.1.2.1 Fock Space

We spare the details of the quantization of the electromagnetic field (see, for example, [130, Chapter 8, §3] or [121, Chapter 7, §6]) and present the important points here. The energy eigenstates take the form of the number basis $|n\rangle$, often referred to as *Fock space*, so that $\hat{n}\,|n\rangle = n\,|n\rangle$ for $n = 0, 1, 2, \ldots$, and the number operator $\hat{n}$. This gives the number of quanta in the field (photons). For a single cavity mode, the system's Hamiltonian takes the form [98, Chapter 13, §1]

$$\hat{H}_F = \hbar\omega_c\left(\hat{n} + \frac{1}{2}\right) \approx \hbar\omega_c\hat{n}, \tag{4.8}$$

where ω_c is the cavity mode frequency and we have, in the last step, neglected the zero-point energy $\hbar\omega_c/2$. Since the energy eigenvalues are quantized by integer multiples of $\hbar\omega_c$, it is convenient to introduce *ladder operators* that raise and lower the energy eigenstates and thus, adds or removes a quanta of energy to or from the field. These take the form of the non-Hermitian creation $\hat{a}^\dagger$ and annihilation $\hat{a}$ operators that raise and lower the eigenstate:

$$\hat{a}^\dagger |n\rangle = \sqrt{n+1}\,|n+1\rangle\,, \qquad \hat{a}\,|n\rangle = \sqrt{n}\,|n-1\rangle\,. \tag{4.9}$$

The number operator can be written in terms of ladder operators as $\hat{n} = \hat{a}^\dagger\hat{a}$, so that the field Hamiltonian becomes

$$\hat{H}_F = \hbar\omega_c\hat{a}^\dagger\hat{a}. \tag{4.10}$$

The eigenstates of the annihilation operator

$$\hat{a}\,|\alpha\rangle = \alpha\,|\alpha\rangle\,, \tag{4.11}$$

are called the *coherent states*:

$$|\alpha\rangle = e^{-\frac{1}{2}|\alpha|^2}\sum_{n=0}^{\infty}\frac{\alpha^n}{\sqrt{n!}}\,|n\rangle\,. \tag{4.12}$$

This is the quantum state that shares the most similarities with a classical coherent laser field [4] and has the property $\langle\hat{n}\rangle = |\alpha|^2$.

4.1.2.2 Jaynes-Cummings Hamiltonian

Now having a quantum description of the electromagnetic field, we move to how atomic systems interact with this quantized field. We consider a two-level atom with ground state $|g\rangle$ and excited state $|e\rangle$, separated by atomic frequency ω_a, and follow the presentation of [130, Chapter 10]. The free evolution Hamiltonian is then

$$\hat{H}_{\text{self}} = \hat{H}_A + \hat{H}_F = \hbar\omega_a\,|e\rangle\!\langle e| + \hbar\omega_c\hat{a}^\dagger\hat{a}, \tag{4.13}$$

where A and F represent the atomic and field Hilbert spaces, respectively. Similar to Appendix A, we write the atom-field interaction in dipole form of Eq. (A.4):

$$\hat{H}_{\text{int}} = -\hat{\boldsymbol{d}}\cdot\hat{\boldsymbol{E}}, \tag{4.14}$$

where the dipole operator $\hat{\boldsymbol{d}}$ takes the form [see Eq. (A.12)]

$$\hat{\boldsymbol{d}} = \langle g|\,\hat{\boldsymbol{d}}\,|e\rangle\,(|g\rangle\!\langle e| + |e\rangle\!\langle g|) = \langle g|\,\hat{\boldsymbol{d}}\,|e\rangle\left(\hat{\sigma} + \hat{\sigma}^\dagger\right). \tag{4.15}$$

The interaction between the atoms and the cavity is given by (see [130, Chapter 8, §3] for the electric field operator $\hat{\boldsymbol{E}}$ derivation)

$$\hat{H}_{\text{int}} = \sqrt{\frac{\hbar\omega_c}{2\epsilon_0}} \left(\hat{\sigma} + \hat{\sigma}^\dagger\right) \langle g| \hat{\boldsymbol{d}} |e\rangle \cdot \left[\boldsymbol{f}(\boldsymbol{r})\hat{a} + \boldsymbol{f}^*(\boldsymbol{r})\hat{a}^\dagger\right], \tag{4.16}$$

where ϵ_0 is the permittivity of free space and $\boldsymbol{f}(\boldsymbol{r})$ is a mode function that satisfies the Helmholtz equation $\left(\boldsymbol{\nabla}^2 + k^2\right) \boldsymbol{f}(\boldsymbol{r}) = 0$.

We now define the cavity coupling constant[1]

$$g(\boldsymbol{r}) = -\sqrt{\frac{2\omega_c}{\hbar\epsilon_0}} \langle g| \hat{\boldsymbol{d}} |e\rangle \cdot \boldsymbol{f}(\boldsymbol{r}), \tag{4.17}$$

so that, at a given point, the interaction Hamiltonian becomes

$$\hat{H}_{\text{int}} = \frac{\hbar g}{2} \left(\hat{\sigma} + \hat{\sigma}^\dagger\right) \left(\hat{a} + \hat{a}^\dagger\right). \tag{4.18}$$

We use the rotating-wave approximation (see Appendix A.3) to write this as

$$\hat{H}_{\text{int}} = \frac{\hbar g}{2} \left(\hat{\sigma} \otimes \hat{a}^\dagger + \hat{\sigma}^\dagger \otimes \hat{a}\right) = \frac{\hbar g}{2} \left(\hat{\sigma}\hat{a}^\dagger + \hat{\sigma}^\dagger\hat{a}\right), \tag{4.19}$$

where we have dropped the tensor products for compactness. As should be expected, the first term in the parenthesis describes the creation of a cavity photon in conjunction with the lowering of the atomic state $|e\rangle \to |g\rangle$ while the second term represent the absorption of a photon $\hat{a}$ that excites the atom $|g\rangle \to |e\rangle$. The total Hamiltonian, called the *Jaynes-Cummings model* [71], is given by

$$\hat{H}_{\text{JC}} = \hbar\omega_a |e\rangle\langle e| + \hbar\omega_c \hat{a}^\dagger\hat{a} + \frac{\hbar g}{2} \left(\hat{\sigma}\hat{a}^\dagger + \hat{\sigma}^\dagger\hat{a}\right). \tag{4.20}$$

4.2 Motivation

With this rudimentary knowledge presented, we can now move on to the idea of entropy removal in laser cooling. As discussed in this chapter's introduction, it is often assumed that the laser fields do not remove entropy from an atomic gas during laser cooling. A typical argument that attempts to denounce the possibility of entropy removal by the laser field is the fact that a

---

[1] Some literature [98, 130] include a factor of 1/2 in this definition, i.e., this is the definition of $2g$.

Hamiltonian process can not change the entropy of a quantum system. This can be seen using the definition of von Neumann entropy Eq. (4.4), the cyclic property of the trace, and the unitary time evolution, under the Hamiltonian $\hat{H}$, of the density matrix (see Eq. B.5):

$$\hat{\rho}(t) = e^{-i\hat{H}(t-t_0)/\hbar}\hat{\rho}(t_0)e^{i\hat{H}(t-t_0)/\hbar}, \tag{4.21}$$

so that $S(t) = \text{const}$. Thus, it is asserted that an interaction that is described in dipole form,

$$\hat{H}_{AF} = \hat{\boldsymbol{d}}_A \cdot \hat{\boldsymbol{E}}_F, \tag{4.22}$$

can not change the entropy of the system, where A and F represent the atomic and field Hilbert spaces, respectively.

While the entropy S_{AF} of the total AF system is indeed a constant, this argument does not consider the entanglement entropy between the two subspaces that can be seen using $\hat{\rho}_A = \text{Tr}_F[\hat{\rho}_{AF}]$ or $\hat{\rho}_F = \text{Tr}_A[\hat{\rho}_{AF}]$ in Eq. (4.4) to calculate $S_A(t)$ or $S_F(t)$. Since, in laser cooling, one is only concerned about reducing the entropy of the atomic subsystem, we see that the entropy can be changed by coherent interaction with a laser. This analysis also explains the mechanism for entropy exchange via spontaneous emission if we replace the laser field's Hilbert space with that of the background radiation bath B. These concepts will be expanded upon in Sections 4.4 and 4.6.

We now present a gedanken experiment that highlights the essential physics of entropy removal in laser cooling, but with a much simpler model. The system that we consider is depicted in Fig. 4.1 and discussed below. A quantum gas consisting of three level atoms is placed inside a lossless optical cavity. We model the initial state of the cavity field as a coherent state $|\alpha\rangle$ [see Eq. (4.12)], as it is the quantum state that has the most in common with a classical laser field. Furthermore, a coherent state is pure ($\hat{\rho}_F(0) = |\alpha\rangle\langle\alpha|$) and the laser field therefore begins the interaction with zero entropy $S_F(0) = 0$. We represent the quantum gas as a single, motionless particle that exists at an anti-node of the optical cavity. While the lack of particle motion distances our investigation from a direct study of laser cooling and trapping, we can still investigate the entropy exchange process by instead studying the evolution of the entropy contained in the particle's internal degrees of freedom. The particle's internal structure is a Λ-configuration with two ground

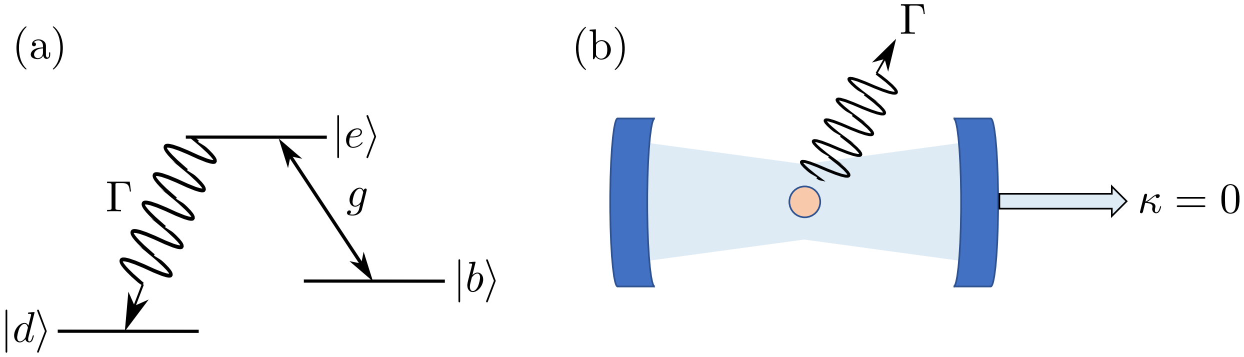

Figure 4.1: Schematic diagram of laser cooling gedanken experiment. (a) Energy diagram of the particle's internal state structure which is a Λ-configuration. It is coupled to the optical cavity with strength g on the bright transition ($|e\rangle \leftrightarrow |b\rangle$) and has a linewidth Γ on the dark transition ($|e\rangle \to |d\rangle$). (b) A schematic of the experimental setup. The quantum gas (orange circle) is placed in a lossless ($\kappa = 0$) optical cavity (dark blue mirrors) that contains a laser field (light blue). The particle can undergo spontaneous emission into free space with rate Γ.

states $|b\rangle$ and $|d\rangle$ and an excited state $|e\rangle$, as shown in Fig. 4.1(a). The $|b\rangle \leftrightarrow |e\rangle$ (bright) transition is resonant with the optical cavity, which models the coherent interaction between the laser and the atoms. Meanwhile, the dark state $|d\rangle$ does not interact with the laser field and is instead only mediated by the spontaneous emission process, which models the incoherent interaction between the background radiation field and the gas. We assume all scattered photons leave the cavity, as shown in Fig. 4.1(b). Our goal now is to understand the evolution of the entropy contained in the particle and laser field subspaces, A and F, and to determine whether or not the F subspace absorbs entropy from the A subspace.

Of course, the quantum state of the laser field must change if it is to absorb entropy from the gas. While a coherent state is unperturbed by the removal of a photon [see Eq. (4.11)], its evolution upon gaining a photon is non-trivial (action of $\hat{a}^\dagger$) [3]. Therefore, one should expect a coherent state to change upon interaction with near-resonant atoms and it is interesting to quantify the change in the laser field state after interaction with the gas. We will investigate this further in Section 4.4 using the model developed in the next section.

4.3 Gedankan Experiment

We now present the model of our gedanken experiment. The full system consists of three subspaces: a three-level particle A and a single mode optical cavity F that is loseless ($\kappa = 0$) except for spontaneous emission into free space into a background radiation field B. The total Hamiltonian is given by

$$\hat{H}_{AFB} = \hat{H}_0 + \hat{H}_{\text{int}}, \tag{4.23}$$

where the free energy is

$$\begin{aligned} \hat{H}_0 &= \hat{H}_A + \hat{H}_F + \hat{H}_B \\ &= \hbar\omega_{eb} |e\rangle \langle e| - \hbar\omega_{bd} |d\rangle \langle d| + \hbar\omega_c \left(\hat{a}^\dagger \hat{a} + \frac{1}{2}\right) + \hbar \sum_n \omega_n \left(\hat{c}_n^\dagger \hat{c}_n + \frac{1}{2}\right). \end{aligned} \tag{4.24}$$

Here, $\hbar\omega_{ij} = E_i - E_j$ is the energy difference between states $|i\rangle$ and $|j\rangle$ of the particle, and $\hat{c}_n$ are the annihilation operators for the background radiation field, which is modeled as an infinite bandwidth bosonic bath. The Hamiltonian describing the interaction between the particle and light fields $\hat{H}_{\text{int}}$ can be written in Jaynes-Cummings form as

$$\begin{aligned}\hat{H}_{\text{int}} =& \hat{H}_{AF} + \hat{H}_{BF} \\ =& \frac{\hbar g}{2}\left(\left|b\right\rangle\left\langle e\right|\hat{a}^{\dagger} + \text{H.c.}\right) + \frac{\hbar}{2}\left(\left|d\right\rangle\left\langle e\right|\sum_{n}\lambda_{n}\hat{c}_{n}^{\dagger} + \text{H.c.}\right),\end{aligned} \tag{4.25}$$

where g and λ_n are the coupling strengths of the particle to the cavity and bath modes [see Eq. (4.17)].

We, under the Born-Markov approximation (see Appendix C.1), trace out the background radiation field and study the dynamics of the reduced density matrix in the atom-field subspace $\hat{\rho}_{AF}$. Furthermore, we assume that the branching ratio of the $|e\rangle \to |d\rangle$ transition is much larger than $|e\rangle \to |g\rangle$ transition so that $\mathit{\Gamma}_d \gg \mathit{\Gamma}_b$, where $\mathit{\Gamma}_i$ is the respective $|e\rangle \to |i\rangle$ transition's linewidth. Moving into an interaction picture defined by $\hat{H}_0$ and assuming the cavity is on resonance with the bright transition $\omega_c = \omega_{eb}$, we arrive at the system's quantum master equation (see subsection 3.1.3)

$$\frac{\partial\hat{\rho}_{AF}}{\partial t} = \frac{1}{i\hbar}\left[\hat{H},\hat{\rho}_{AF}\right] + \hat{\mathcal{D}}\left[\sqrt{\mathit{\Gamma}}\left|d\middle\rangle\middle\langle e\right|\right]\hat{\rho}_{AF}, \tag{4.26}$$

in which the coherent particle-laser interaction is determined by the Hamiltonian

$$\hat{H} = \frac{\hbar g}{2}\left(\left|b\right\rangle\left\langle e\right|\hat{a}^{\dagger} + \text{H.c.}\right), \tag{4.27}$$

and we have set the spontaneous emission rate $\mathit{\Gamma} \equiv \mathit{\Gamma}_d$. In the sections that follow, we consider both analytical and numerical solutions to Eq. (4.26) with the atom initialized in a mixed state in the ground state manifold:

$$\hat{\rho}_A(0) = x\left|b\right\rangle\left\langle b\right| + (1-x)\left|d\right\rangle\left\langle d\right|. \tag{4.28}$$

We use the QuantumOptics package in the Julia programming language for all numerical calculations [77]. Since $|d\rangle$ is a dark state that does not undergo stimulated absorption throughout the process, any population that is in $|d\rangle$ will remain in that state. Therefore, as $t \to \infty$, one would expect the atomic ensemble $\hat{\rho}_A$ to end the process in a near pure state $\hat{\rho}_A(\infty) \approx |d\rangle\langle d|$, limited only by the probability of having 0 photons in the cavity, $P_0 = \exp[-\langle\hat{n}\rangle]$. However, the dynamics of the field $\hat{\rho}_F(t)$ is not obvious.

4.4 Displacement of Laser Field

We first demonstrate a change of the laser state upon interaction with the particle, which we define as the fidelity F between the initial laser state $\hat{\rho}_F(0)$ and the laser state after the AF system has reached equilibrium: $\hat{\rho}_F(\infty)$. Here, the laser field state $\hat{\rho}_F(t)$ is defined as the reduced density matrix on the F subspace $\hat{\rho}_F(t)$. Since the laser state is initialized as a coherent state $|\alpha\rangle$, the fidelity F is simply [see Eq. (4.3)]

$$F\big[\hat{\rho}_F(\infty), \hat{\rho}_F(0)\big] = \langle\alpha|\, \hat{\rho}_F(\infty)\, |\alpha\rangle\,. \tag{4.29}$$

4.4.1 Block Matrix Formalism

In order to derive an analytic form of the final state of the cavity, we now present a method for separating the density matrix into Jordan blocks to allow us to solve for the steady-state using the master equation. Our initial state

$$\begin{aligned}\hat{\rho}(0) &= [x\,|b\rangle\!\langle b| + (1-x)\,|d\rangle\!\langle d|] \otimes |\alpha\rangle\!\langle\alpha| \\ &= x\left(e^{-\frac{1}{2}|\alpha|^2}\sum_{n'=0}^{\infty}\frac{\alpha^{n'}}{\sqrt{n'!}}\,\big|b,n'\big\rangle\right)\left(e^{-\frac{1}{2}|\alpha|^2}\sum_{n=0}^{\infty}\frac{(\alpha^*)^n}{\sqrt{n!}}\,\langle b,n|\right) \\ &\quad + (1-x)\left(e^{-\frac{1}{2}|\alpha|^2}\sum_{n'=0}^{\infty}\frac{\alpha^{n'}}{\sqrt{n'!}}\,\big|d,n'\big\rangle\right)\left(e^{-\frac{1}{2}|\alpha|^2}\sum_{n=0}^{\infty}\frac{(\alpha^*)^n}{\sqrt{n!}}\,\langle d,n|\right),\end{aligned} \tag{4.30}$$

explicitly assumes there are no coherences between the three internal states. This motivates us solving the dynamics of the block matrices:

$$\begin{aligned}\hat{\rho}_b &= \langle b|\,\hat{\rho}\,|b\rangle\,|b\rangle\!\langle b| + \langle b|\hat{\rho}\,|e\rangle\,|b\rangle\!\langle e| + \langle e|\,\hat{\rho}\,|b\rangle\,|e\rangle\!\langle b| + \langle e|\,\hat{\rho}\,|e\rangle\,|e\rangle\!\langle e|\,, \\ \hat{\rho}_d &= \langle d|\,\hat{\rho}\,|d\rangle\,|d\rangle\!\langle d|\,.\end{aligned} \tag{4.31}$$

Taking a time derivative and using the master equation Eq. (4.26) in the form [see Eq. (C.28)]

$$\frac{\partial\hat{\rho}}{\partial t} = \frac{1}{i\hbar}\left(\hat{H}_{\text{eff}}\hat{\rho} - \hat{\rho}\hat{H}_{\text{eff}}^{\dagger}\right) + \hat{\mathcal{L}}_{\text{jump}}\left(\hat{\rho}\right), \tag{4.32}$$

we find

$$\dot{\hat{\rho}}_d = \Gamma\,\langle e|\,\hat{\rho}\,|e\rangle\,|d\rangle\!\langle d|\,, \qquad \dot{\hat{\rho}}_b = \frac{1}{i\hbar}\left[\hat{H}_{\text{eff}}\hat{\rho}_b - \hat{\rho}_b\hat{H}_{\text{eff}}^{\dagger}\right], \tag{4.33}$$

where we have used $\langle i|\,\hat{\mathcal{L}}_{\mathrm{jump}}\,|j\rangle = 0$ for $i,j \in \{b,e\}$ and defined [see Eqs. (C.26) and (C.27)]

$$\hat{H}_{\mathrm{eff}} = \hat{H} - \frac{i\hbar\mathit{\Gamma}}{2}\,|e\rangle\!\langle e|\,, \qquad \hat{\mathcal{L}}_{\mathrm{jump}}(\hat{\rho}) = \mathit{\Gamma}\,|d\rangle\!\langle e|\,\hat{\rho}\,|e\rangle\!\langle d|\,. \tag{4.34}$$

We first look at the subset $\{|e,n-1\rangle\,, |b,n\rangle\}$ and diagonalize the non-Hermitian matrix

$$\hat{H}_n = \frac{\hbar}{2}\begin{pmatrix} -i\mathit{\Gamma} & g\sqrt{n} \\ g\sqrt{n} & 0 \end{pmatrix}, \tag{4.35}$$

for $n > 0$. The eigenvalues are given by $\lambda_{\pm}^{(n)} = -i\hbar\mathit{\Lambda}_{\pm}^{(n)}$, with

$$\mathit{\Lambda}_{\pm}^{(n)} \equiv \frac{\mathit{\Gamma}}{4} \pm \frac{i}{2}\sqrt{ng^2 - \frac{\mathit{\Gamma}^2}{4}}, \tag{4.36}$$

and the kernel of the matrix $\hat{H}_n - \lambda_{\pm}^{(n)}\hat{\mathbb{I}}$ is spanned by

$$\hat{V}_n = \frac{\hbar}{c_n}\begin{pmatrix} -i\mathit{\Lambda}_{+}^{(n)} & -\frac{g\sqrt{n}}{2} \\ \frac{g\sqrt{n}}{2} & -i\mathit{\Lambda}_{+}^{(n)} \end{pmatrix}, \tag{4.37}$$

with normalization factor: $c_n^2 = \left(-i\hbar\mathit{\Lambda}_{+}^{(n)}\right)^2 + \hbar^2 g^2 n/4$. We now define $\hat{V} = \sum_n \hat{V}_n \otimes \hat{I}_n$ with n^{th} projection operator $\hat{I}_n$ so that the bright manifold matrix can be written as $\hat{\rho}_b = \hat{V}\hat{\rho}_V\hat{V}^{\dagger}$.

We can use Laplace's equation, $L[\hat{A}](s) = \int_0^\infty dt e^{-st}\hat{A}$, to solve for the transformed density matrix (see [130, Chapter 5, §5]):

$$sL[\hat{\rho}] = L\left[\dot{\hat{\rho}}\right](s) + \hat{\rho}(0), \tag{4.38}$$

which we then can solve for steady-state:

$$\hat{\rho}(t\to\infty) = \lim_{s\to 0} L[\dot{\hat{\rho}}](s) + \hat{\rho}(0). \tag{4.39}$$

Projecting with $\langle d|$ and $|d\rangle$ and using the master equation Eq. (4.26), $\langle d|\,\hat{\rho}_b\,|d\rangle = 0$, and $\langle e|\,\hat{\rho}_d\,|e\rangle = 0$, we find

$$\langle d|\,\hat{\rho}_d(\infty)\,|d\rangle = \mathit{\Gamma}\lim_{s\to 0}\langle e|\,L[\hat{\rho}_b](s)\,|e\rangle + \langle d|\,\hat{\rho}_d(0)\,|d\rangle\,. \tag{4.40}$$

To solve for the first term on the right-hand side, we find

$$L[\hat{\rho}_V](s) = L\left[\hat{V}^{-1}\hat{\rho}_b\hat{V}^{-\dagger}\right](s) = \sum_{n,n'\geq 1}\hat{R}_{n',n}\otimes\hat{I}_{n',n}, \tag{4.41}$$

where $\hat{I}_{n',n}$ is a matrix with 1 at position n', n and zeros everywhere else, and

$$\hat{R}_{n',n} = \frac{\hbar^2}{c_{n'}c_n^*} \begin{pmatrix} \frac{g^2\sqrt{nn'}}{4(s+\mathit{\Lambda}_+^{(n')}+\mathit{\Lambda}_+^{(n)*})} & \frac{ig\sqrt{n'}\mathit{\Lambda}_+^{(n)*}}{2(s+\mathit{\Lambda}_+^{(n')}+\mathit{\Lambda}_-^{(n)*})} \\ -\frac{ig\sqrt{n}\mathit{\Lambda}_+^{(n')}}{2(s+\mathit{\Lambda}_-^{(n')}+\mathit{\Lambda}_+^{(n)*})} & \frac{\mathit{\Lambda}_+^{(n')}\mathit{\Lambda}_+^{(n)}}{(s+\mathit{\Lambda}_-^{(n')}+\mathit{\Lambda}_-^{(n)*})} \end{pmatrix} e^{-|\alpha|^2} \frac{\alpha^{n'}(\alpha^*)^n}{\sqrt{n'!}\sqrt{n!}}. \tag{4.42}$$

We next calculate

$$L[\hat{\rho}_b](s) = \sum_{n,n'\geq 1} \hat{V}_{n'}\hat{R}_{n'n}\hat{V}_n^\dagger \otimes \hat{I}_{n'n}, \tag{4.43}$$

and project with $\langle e|$ and $|e\rangle$ to find the first term on the right hand side of Eq. (4.40). Remembering that the excited state in our basis in Eq. (4.35) is $|e, n-1\rangle$, Eq. (4.40) becomes

$$\begin{aligned} \langle d|\,\hat{\rho}_d(\infty)\,|d\rangle =& x \sum_{n,n'\geq 1} \frac{\sqrt{nn'}}{\frac{n+n'}{2} + \frac{g^2}{4\mathit{\Gamma}^2}\,(n-n')^2} \left|n'-1\middle\rangle\middle\langle n-1\right| \langle n'|\alpha\rangle \langle \alpha|n\rangle \\ &+ (1-x) \sum_{n,n'\geq 0} \left|n'\middle\rangle\middle\langle n\right| \langle n'|\alpha\rangle \langle \alpha|n\rangle\,, \end{aligned} \tag{4.44}$$

where we have used $\langle b, n'|\,\hat{\rho}_b(0)\,|b, n\rangle = x\,\langle n'|\alpha\rangle\,\langle \alpha|n\rangle$ and $\langle d, n'|\,\hat{\rho}_d(0)\,|d, n\rangle = (1-x)\,\langle n'|\alpha\rangle\,\langle \alpha|n\rangle$. Projecting $\langle b|$ and $|b\rangle$ on Eq. (4.39) and noting that the steady-state bright state population results from the cavity being in the vacuum state $|0\rangle$, we have

$$\langle b|\,\hat{\rho}_b(\infty)\,|b\rangle = x\,|0\rangle\langle 0|\,\langle 0|\alpha\rangle\,\langle \alpha|0\rangle\,. \tag{4.45}$$

Now that we have traced over the atomic states, we find the steady-state cavity density matrix

$$\begin{aligned} \hat{\rho}_F(\infty) =& x \left(e^{-|\alpha|^2}\,|0\rangle\langle 0| + \sum_{n,n'\geq 1} \frac{\sqrt{nn'}}{\frac{n+n'}{2} + \frac{g^2}{4\mathit{\Gamma}^2}\,(n-n')^2} \left|n'-1\middle\rangle\middle\langle n-1\right| e^{-|\alpha|^2} \frac{\alpha^{n'}(\alpha^*)^n}{\sqrt{n'!}\sqrt{n!}} \right) \\ &+ (1-x) \sum_{n,n'\geq 0} \left|n'\middle\rangle\middle\langle n\right| e^{-|\alpha|^2} \frac{\alpha^{n'}(\alpha^*)^n}{\sqrt{n'!}\sqrt{n!}}. \end{aligned} \tag{4.46}$$

4.4.2 Fidelity Calculation

We now introduce the critical photon number

$$m_0 \equiv \frac{1}{2}\left(\frac{\mathit{\Gamma}}{g}\right)^2, \tag{4.47}$$

which can be understood as the minimum Fock state that significantly participates in the dynamics [75]. We can therefore rewrite the final cavity field Eq. (4.46) as

$$\hat{\rho}_F(\infty) = (1-x)\hat{\rho}_F(0) + x \left(e^{-|\alpha|^2}\,|0\rangle\langle 0| + |\alpha|^2 \sum_{n,n'\geq 0} K_{n,n'} \left|n'\middle\rangle\middle\langle n\right| e^{-|\alpha|^2} \frac{\alpha^{n'}(\alpha^*)^n}{\sqrt{n'!}\sqrt{n!}} \right), \tag{4.48}$$

where $\hat{\rho}_F(0) = |\alpha\rangle\langle\alpha|$ and

$$K_{n,n'} \equiv \left(1 + \frac{n+n'}{2} + \frac{(n-n')^2}{8m_0}\right)^{-1}. \tag{4.49}$$

Defining the initial intracavity photon number $\bar{n}_0 \equiv \langle \hat{a}^\dagger \hat{a}(0)\rangle = |\alpha|^2$, we find the fidelity between the initial and final states of the cavity Eq. (4.29):

$$F\big[\hat{\rho}_F(\infty), \hat{\rho}_F(0)\big] = 1 - x\left(1 - e^{-2\bar{n}_0}\left[1 + \bar{n}_0 \sum_{n,n'\geq 0} K_{n,n'} \frac{\bar{n}_0^{(n+n')}}{n'!\,n!}\right]\right). \tag{4.50}$$

The classical limit results from a field that contains many photons $\bar{n}_0 \to \infty$. We now consider two limiting cases that exemplify the displacement of the laser field.

We first consider the limit of zero linewidth $m_0 \to 0$ in which $K_{n,n'} \to \delta_{n,n'}/(1+n)$:

$$F_{m_0\to 0} = 1 - x\left(1 - e^{-2\bar{n}_0}\left[1 + \bar{n}_0 \sum_{n\geq 0} \frac{1}{1+n}\left(\frac{\bar{n}_0^n}{n!}\right)^2\right]\right). \tag{4.51}$$

We note that the the modified Bessel functions of the first kind are [10, Chapter 11, §5]

$$I_v(x) = \sum_{s=0}^{\infty} \frac{1}{s!(s+v)!}\left(\frac{x}{2}\right)^{(2s+v)}, \tag{4.52}$$

such that

$$I_1(2\bar{n}_0) = \sum_{n=0}^{\infty} \frac{1}{n!(n+1)!}\bar{n}_0^{(2n+1)} = \sum_{n=0}^{\infty} \frac{\bar{n}_0}{n+1}\left(\frac{\bar{n}_0^n}{n!}\right)^2. \tag{4.53}$$

We therefore find

$$F_{m_0\to 0} = 1 - x\left(1 - e^{-2\bar{n}_0}\left[1 + I_1(2\bar{n}_0)\right]\right), \tag{4.54}$$

which we take in the classical limit

$$\lim_{\bar{n}_0\to\infty} F_{m_0\to 0} = 1 - x\left(1 - \frac{1}{2\sqrt{\pi\bar{n}_0}}\right) \approx 1 - x, \tag{4.55}$$

where we have used

$$\lim_{\bar{n}_0\to\infty} I_1(2\bar{n}_0) = \frac{e^{2\bar{n}_0}}{2\sqrt{\pi\bar{n}_0}}. \tag{4.56}$$

Interestingly, we find that $F_{m_0\to 0} \approx 1 - x$ in the limit of zero linewidth. The fact that $F_{m_0\to 0} \neq 1$ in this case provides direct evidence that the laser state can be substantially changed upon interaction with a quantum gas.

We now look at the opposite limit, that of infinite linewidth $m_0 \to \infty$. We have $K_{n,n'} \to (1+\frac{n+n'}{2})^{-1}$ and thus,

$$F_{m_0\to\infty} = 1 - x\left(1 - e^{-2\bar{n}_0}\left[1 + \frac{1 - e^{2\bar{n}_0}(1-2\bar{n}_0)}{2\bar{n}_0}\right]\right). \tag{4.57}$$

In the classical limit, we find

$$\lim_{\bar{n}_0\to\infty} F_{m_0\to\infty} = 1 - \frac{x}{2\bar{n}_0} \approx 1. \tag{4.58}$$

This demonstrates the importance of allowing the atom and field to interact for a substantial period before decaying to the dark state. The classical limit fidelities are thus:

$$\lim_{\bar{n}_0\to\infty} F\big[\hat{\rho}_F(\infty), \hat{\rho}_F(0)\big] = \begin{cases} 1 - x\left(1 - \frac{1}{2\sqrt{\pi\bar{n}_0}}\right), & m_0 = 0 \\ 1 - \frac{x}{2\bar{n}_0}, & m_0 \to \infty \end{cases} \tag{4.59}$$

We interpret the deviation from $F = 1$ as result of entanglement generation between the atoms and field through the coherent interaction $\hat{H}$ [see Eq. (4.27)].

4.4.3 Numerical Results

Having demonstrated in the two extreme regimes that the cavity state can change, we now turn to numerical simulations to check our analytic conclusions. We exemplify the change in the field in the intermediate regime by simulating the master equation Eq. (4.26) with $g = \Gamma = 1$ (and thus $m_0 = 1/2$). In Fig. 4.2, we plot the fidelity (blue curve) between the initial and final states of the field as a function of the initial intracavity photon number $\bar{n}_0$. We see that the fidelity only equals unity in the limit $\bar{n}_0 \to 0$, which is a result of the atomic gas and field not interacting when no photons are in the cavity. In contrast, the fidelity falls below unity for $\bar{n}_0 > 0$ which demonstrates that the laser state has changed as a result of its interaction with the atom. The fidelity asymptotes to some value less than unity in the classical limit $\bar{n}_0 \to \infty$ (dashed red line), demonstrating that the laser field is changed even when treated as a classical electric field. We verify the value of $\lim_{\bar{n}_0\to\infty} F$ using the analytic calculations from subsection 4.4.2.

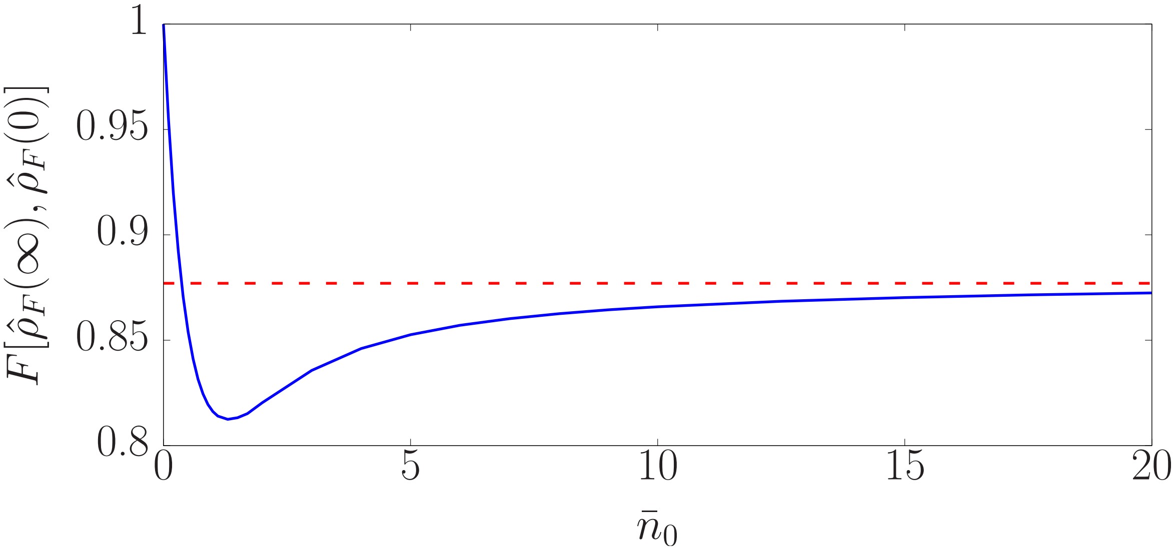

Figure 4.2: Fidelity F Eq. (4.50) between the initial and final laser states $\hat{\rho}_F(0)$ and $\hat{\rho}_F(\infty)$ (solid blue curve) as a function of the initial average intracavity photon number $\bar{n}_0$. The dashed red curve displays F in the infinite cavity photon limit $\bar{n}_0 \to \infty$. The fidelity F is equal to unity only when $\bar{n}_0 = 0$, demonstrating that the laser state is changed upon interaction with the particle. The parameters are $g = \Gamma = 1$.

4.5 Bayesian Analysis

Now that we have shown that the laser field is displaced upon its interaction with an atomic mixture, we demonstrate that information about the atom can be imprinted on the laser field. To this end, we first determine the dependence of the equilibrium laser state on the initial bright state fraction x. We will then examine the information transfer from a quantum information perceptive in the next section.

We first reduce the number of cavity photons by shifting the laser state toward the vacuum state by application of the displacement operator $\hat{D}$ of the initial coherent state [4, Chapter 1, §4]

$$\hat{D}(\alpha) \equiv \exp\left[\alpha\hat{a}^{\dagger} - \alpha^{*}\hat{a}\right], \qquad |\alpha\rangle = \hat{D}(\alpha)\,|0\rangle\,, \tag{4.60}$$

so that

$$\hat{\sigma}_F(x) = \hat{D}^{\dagger}(\alpha)\hat{\rho}_F(\infty)\hat{D}(\alpha) = \hat{D}(-\alpha)\hat{\rho}_F(\infty)\hat{D}(\alpha). \tag{4.61}$$

The dependence on the initial bright fraction x is obvious from Eq. (4.48). While Eq. (4.61) may be analytically tractable for $m_0 = 0$ and $\bar{n}_0 \to \infty$, we do not pursue such an analytical expression here.

The probability distribution for x, $P(x|n)$, can then be generated through Bayesian inference by sampling the resulting photon number distribution $P(n|x) = \langle n|\,\hat{\sigma}_F\,|n\rangle$ [68]. The procedure adopted is as follows. Bayes theorem states

$$P(x|n) = \frac{1}{P(n)}P(n|x)P(x), \tag{4.62}$$

where $P(x)$ is the prior knowledge about the initial bright fraction and $1/P(n)$ is a normalization factor. We assume that the prior is initially flat. For a given x, we first calculate the photon number distribution $P(n|x)$ and use the distribution to simulate a photon detection event. We use this to update our prior $P(x)$ and apply Eq. (4.62) to arrive at a new posterior probability distribution $P(x|n)$. To quantify how well the posterior predicts the initial bright fraction x, we fit $P(x|n)$ to a normalized Gaussian distribution and calculate its standard deviation $\sigma_N(x)$ as a metric of coincidence, as exemplified in the inset of Fig. 4.3. We then repeat the process N times for each $x \in \{0, 0.01, 0.02, \ldots, 1\}$. Furthermore, we repeat each run of x and average the results to minimize the inherent statistical unpredictability of each run.

The results of our Bayesian analysis are displayed in Fig. 4.3 and discussed below. We plot the standard deviation $\sigma_N(x)$ of the Gaussian fit of $P(x|n)$ for three different numbers of iterations, $N = 25$ (blue circles), $N = 50$ (orange crosses), and $N = 100$ (gold stars), with $m_0 = 1/2$ and $\bar{n}_0 = 5$. We see that the curves for $\sigma_N(x)$ decreases as N increases for every x. This indicates that the Gaussian fits are converging on the initial bright population as we generate more data from photodetection events. Furthermore, the figure demonstrates that the minimum of $\sigma_N(x)$ occurs at a value $x \neq 0, 1$. Noting that the two extreme values of x are when the atom is initially pure ($|b\rangle\langle b|$ and $|d\rangle\langle d|$), this behavior indicts that atomic states with initial entropy are easier to predict from cavity field measurements. In addition, the minimum occurs at values with a large initial dark state population, rather than the state $x = 0.5$ which has the maximum initial entropy. This suggests that the initial atomic state is easier to predict when there is less atom-field interaction but the atom has initial entropy.

4.6 State Purification and Mutual Information

A further complication of the thought experiment is that it may be unclear whether any of the final field entropy is directly transferred from the atom or if this is new entropy generated by entanglement between the atom and the field during the interaction. To investigate this question further, we now look at the gedanken experiment from a quantum information prospective. This will allow us to separate atomic entropy that must be removed during the process from the generated entanglement entropy (GEE).

We first purify the atomic state by way of its Schmidt decomposition. That is, we view the atomic ensemble as a marginal of a pure state, $\hat{\rho}_A = \mathrm{Tr}_R[|s^{(AR)}\rangle\langle s^{(AR)}|]$, where

$$\left|s^{(AR)}\right\rangle = \sum_j \sqrt{\beta_j} \left|\psi_j^{(A)}\right\rangle \otimes \left|\phi_j^{(R)}\right\rangle . \tag{4.63}$$

Here, $\hat{\rho}_A \left|\psi_j^{(A)}\right\rangle = \beta_j \left|\psi_j^{(A)}\right\rangle$ are the atomic eigenvectors and $\left|\phi_j^{(R)}\right\rangle \in \mathcal{H}_R$ for some auxiliary

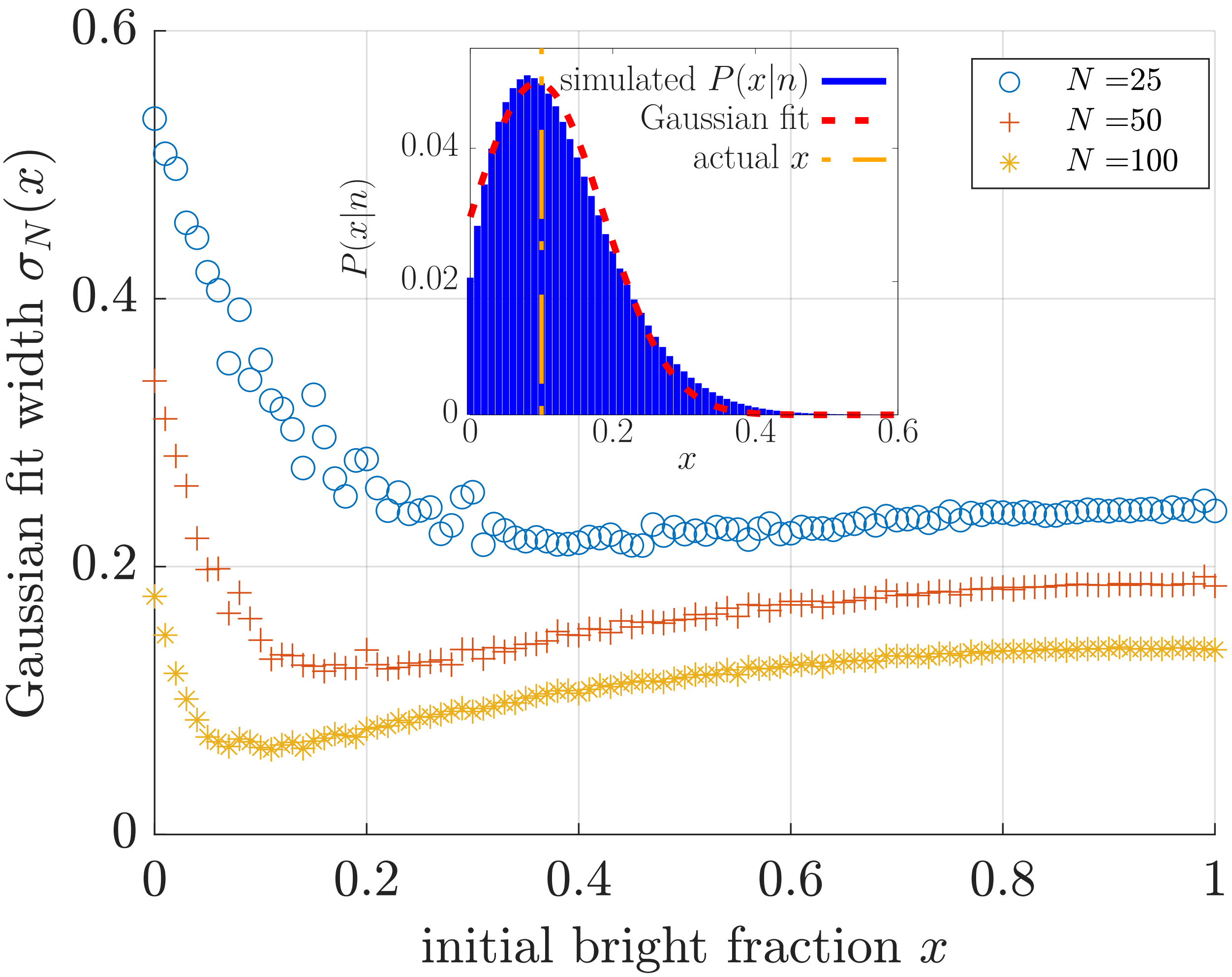

Figure 4.3: Standard deviation $\sigma_N(x)$ of the Gaussian fit to the posterior probability distribution $P(x|n)$ as a function of the initial bright fraction x after $N = 25$ (blue circles), 50 (orange targets), and 100 (gold stars) iterations. Inset: An example of a simulated $P(x|n)$ (blue, dotted) and associated Gaussian fit $\sigma_1 00(x)$ (black, solid). Both distributions are maximized near the actual bright fraction $x = 0.1$ (red, dot-dashed).

Hilbert space $\mathcal{H}_R$. It can be shown that the marginals of $\left|s^{(AR)}\middle\rangle\!\middle\langle s^{(AR)}\right|$ have the same eigenvalues [107]. This motivates the choice of $\hat{\rho}_R(0) = \mathrm{Tr}_A[\left|s^{(AR)}(0)\middle\rangle\!\middle\langle s^{(AR)}(0)\right|]$ to be an identically prepared ensemble to $\hat{\rho}_A(0)$, but with atoms that are not interacting with the field. Thus, the total system's density matrix becomes $\hat{\rho} = \hat{\rho}_{ARF}$, but only the identity operator of the $\mathcal{H}_R$ basis appears in the system's Hamiltonian and jump operators in Eq. (4.26): $\hat{H} \to \hat{H} \otimes \hat{\mathbb{I}}_R$ and $\sqrt{\varGamma}\,|d\rangle\!\langle e| \to \sqrt{\varGamma}\,|d\rangle\!\langle e| \otimes \hat{\mathbb{I}}_R$.

Since the auxiliary state in $\mathcal{H}_{\mathcal{R}}$ purifies the initial state of the atom, it contains information about $\hat{\rho}_A(0)$. We can therefore quantify the amount of information that is common to the cavity and auxiliary atom subsystems using quantum mutual information Eq. (4.7):

$$I(R:F) = S(\hat{\rho}_R) + S(\hat{\rho}_F) - S(\hat{\rho}_{RF}). \tag{4.64}$$

We characterize the information flow between the real atoms and the cavity by determining if there are any correlations between the field and the non-interacting atom, $I(R:F)$.

In Fig. 4.4, we track the von Neumann entropy of the various subsystems of the interaction, as well as the mutual information between the field and auxiliary atom. We start the atom in the maximum entropy state $x = 0.5$ and the field in a coherent state with $\bar{n}_0 = 5$. Furthermore, we choose $m_0 = 1/2$. It is clear that the field entropy (green line) increases throughout the process. This demonstrates that the field is not only displaced from its initial state during the interaction, but that the field ends the process in some mixed state rather than a new coherent state. We differentiate the entropy that is transferred from the atom during the interaction from the GEE by studying the mutual information between the field and auxiliary atoms Eq. (4.64). Fig. 4.4 demonstrates the the mutual information (dashed gold curve) increases during the interaction. This exemplifies, from a quantum information perspective, that part of the initial entropy in the atomic state has been transferred to the field as a result of the coherent dynamics of the system.

4.7 Outlook

Our results conclude that the laser field can also remove entropy from the gas, and that the laser field is consequently altered in a detectable manner. We do emphasize, however, that

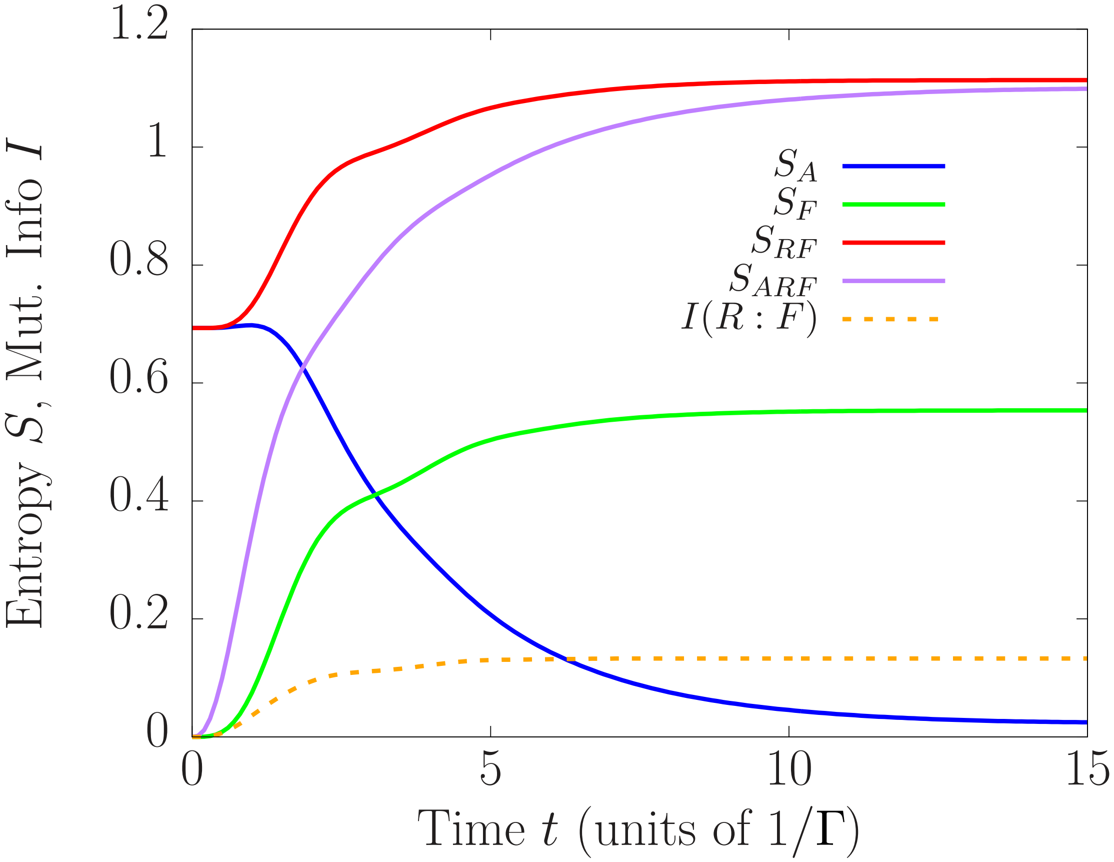

Figure 4.4: Entropy of various subspaces and quantum mutual information (dashed gold curve) between the field and non-interacting atoms $I(R:F) = S(\hat{\rho}_R) + S(\hat{\rho}_F) - S(\hat{\rho}_{RF})$. We display the entropy of the atomic (blue curve), field (green curve), and atom-auxiliary atom (red curve) subspaces, as well as the total entropy (purple curve) in time. The parameters are $g = \mathit{\Gamma} = 1$.

our conclusion requires the existence of spontaneous emission, so we do not claim the existence of steady-state gas-laser entropy exchange in its absence. Furthermore, comparing the initial atomic entropy and the final mutual information in Fig. 4.4 suggests that the field absorbs only a fraction of the initial atomic entropy. This implies, for our specific simulation parameters, that the majority of the initial atomic entropy has been transferred to the background radiation field.

It would be interesting to investigate if a regime exists where $I(R : F)$ increases significantly. It is possible that this may be done by deriving an analytic solution for the mutual information in a similar manner as Section 4.4. Another possible discussion point may be the the use of quantum discord [51] as a further measure of quantum correlations. This may allow us to connect our research to Liouville's theorem in a more appropriate way, by the use of Wigner trajectories [122].

Additional future work will explore the possibility of deriving analytic solutions using the block matrix formalism. As mentioned in Section 4.5, the displaced equilibrium laser field Eq. (4.61) might be analytically tractable for $m_0 = 0$ and $\bar{n}_0 \to \infty$. This calculation could inform how the minimum in Fig. 4.3 tends towards as $N \to \infty$. A non-zero value would be quite interesting as it would demonstrate that states with initial entropy are easier to predict in the limit of infinite iterations of the experiment.

Chapter 5

Subradiant State Selection by Photon Detection

In the last chapter, we demonstrated that an atomic system tends towards zero entropy as it becomes a pure state during the laser cooling process, subject to the condition of the second law of thermodynamics. This extends to more general systems where similar entropy reduction processes can occur when a subsytem is coupled to an environmental bath [2]. In this chapter, we present a protocol for creating low entropy many-body states that results from the steady-state superradiance model in the weak pumping regime [91, 90]. Here, we first drive the system to have a high probability of occupancy of its *subradiant state*, and then implement a detection phase to separate this state from the mixture. In doing so, we are reducing the system's entropy in a similar manner to the energy redistribution that occurs during evaporative cooling by way of two-body collisions. This cooling analogue is explored in Section 5.3.

While entropy removal is a consequence of our subradiant state selection protocol, its most useful application lies in the ever growing field of *quantum metrology* where quantum effects are exploited to enhance the precision of measurements beyond the capability of purely classical approaches [57]. This is because the subradiant state has the property that the total spontaneous emission scattering rate is significantly reduced compared to the independent decay rate as a result of interatomic interference. This occurs even in the presence of a significant amount of excited state population. The weakening of the system to the background radiation field allows for protocols that are robust to dissipative effects. This is an important consideration when the evolution times in metrological processes approach the lifetime of the excited state and thus, spontaneous emission

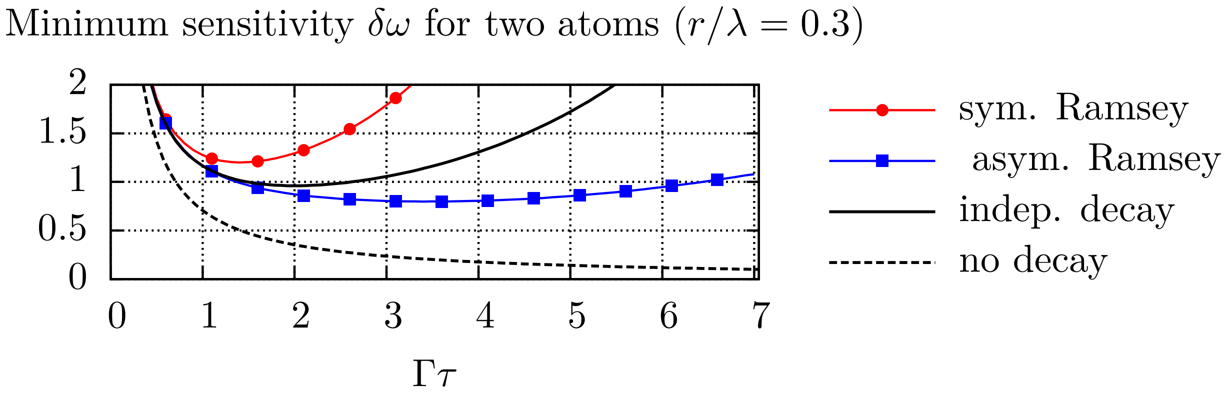

Figure 5.1: Source: Ref. [111]. Two-atom metrology plotting the optimal sensitivity $\delta\omega$ as a function of $\tau\mathit{\Gamma}$. This displays the enhancement of sensitivity for long time scales while using the anti-symmetric Ramsey sequence. The atoms are separated by a distance $r = 0.3\lambda$, with wavelength λ.

becomes a critical factor. To exemplify the usefulness of subradiant states in quantum metrology, we present a result from the the anti-symmetric Ramsey technique (ART) [111] that demonstrates the significant sensitivity improvement for timescales $\tau \gg \mathit{\Gamma}$. Fig. 5.1 shows the improvement of population inversion measurements at the end of a Ramsey-like [116] sequence, but with the free evolution now occurring with the system in its anti-symmetric state (blue curve) as opposed to a symmetric state (red curve). The basis of this improvement lies in the fact that decoherent spontaneous emission can cause a detrimental effect on population inversion, especially as the scattered photon number becomes proportional to the atom number [79, 53]. This can lead, for example, to improved measurements of transition frequencies [149, 22, 136].

Having motivated the usefulness of systems that are weakly coupled to the background radiation field in quantum metrology, we now turn our attention to the problem of effectively creating the subradiant state. While this is often an untrackable problem [111], we demonstrate a procedure that first enhances the subradiant state population and then selects this subradiant state out of a mixed ensemble by way of a photodetection scheme. We begin this chapter with some background information by introducing the concept of angular momentum in quantum mechanics and apply it to the problem of super- and subradiance. We then introduce a many-body model that leads to steady-state superradiance in the strong pumping limit, but a collective dark state with high overlap with the subradiant state in the weak pumping regime. We next propose a protocol to select the subradiant state from the statistical mixture. We then conclude the chapter by connecting our scheme to the idea of entropy removal by making an analogue to evaporative cooling.

5.1 Dicke Basis Background

5.1.1 Addition of Angular Momenta

I now provide a brief introduction to the addition of angular momentum in quantum mechanics. I again follow a similar format to Sakurai's presentation and refer the reader to [121, Chapter 3, §1,5,8] for a detailed derivation of the equations presented. This is useful in describing a collection of N two-level atoms because of the psuedo-spin $\frac{1}{2}$ nature of each atom, as discussed in subsection 2.4.1.

5.1.1.1 Eigenbasis of Angular-Momentum Operators

We begin with the quantum operator $\hat{D}(R)$ that induces, in the appropriate basis, the transformation

$$|\psi(\hat{\boldsymbol{n}},\theta)\rangle = \hat{D}[R(\hat{\boldsymbol{n}},\theta)]\,|\psi\rangle\,, \tag{5.1}$$

on a state $|\psi\rangle$ into a rotated system defined by a three-dimensional orthogonal matrix R characterized by a unit vector $\hat{\boldsymbol{n}}$ and angle θ. For infinitesimal rotations $d\theta$, this is given by the unitary operator

$$\hat{D}[R(\hat{\boldsymbol{n}},d\theta)] = 1 - i\left(\frac{\hat{\boldsymbol{J}}\cdot\hat{\boldsymbol{n}}}{\hbar}\right)d\theta, \tag{5.2}$$

where $\hat{\boldsymbol{J}} \equiv \hat{J}_x + \hat{J}_y + \hat{J}_z$ is the angular-momentum operator. The SO(3) rotation group is non-Abelian as the individual generators $\hat{J}_i$ about the three axes do not commute,

$$\left[\hat{J}_i, \hat{J}_j\right] = i\hbar\varepsilon_{ijk}\hat{J}_k, \tag{5.3}$$

with Levi-Civita symbol ε_{ijk}. Since the generators are not simultaneously diagonalizeable, we introduce a new operator $\hat{\boldsymbol{J}}^2 \equiv \hat{J}_x\hat{J}_x + \hat{J}_y\hat{J}_y + \hat{J}_z\hat{J}_z$ with the property $\left[\hat{\boldsymbol{J}}^2, \hat{J}_i\right] = 0$ so that[1]

$$\hat{\boldsymbol{J}}^2 \left|a, b\right\rangle = a \left|a, b\right\rangle, \qquad \hat{J}_z \left|a, b\right\rangle = b \left|a, b\right\rangle. \tag{5.4}$$

We determine the eigenvalues a and b using the non-Hermitian ladder operators $\hat{J}_\pm \equiv \hat{J}_x \pm i\hat{J}_y$, such that

$$\hat{J}_\pm \left|a, b\right\rangle = c_\pm \left|a, b \pm \hbar\right\rangle, \qquad \hat{J}_z\hat{J}_\pm \left|a, b\right\rangle = (b \pm \hbar)\hat{J}_\pm \left|a, b\right\rangle, \tag{5.5}$$

with normalization constants $c_\pm$. We see that b will be quantized by integer multiples of $\hbar$ and that the $\hat{J}_z$ eigenstate is raised (lowered) by $\hat{J}_+$ ($\hat{J}_-$).

By imposing boundary conditions on b, $b_{\text{min}} \leq b \leq b_{\text{max}}$, it can be shown that

$$\begin{gathered} \hat{\boldsymbol{J}} \left|j, m\right\rangle = j(j+1)\hbar^2 \left|j, m\right\rangle, \qquad \hat{J}_z \left|j, m\right\rangle = m\hbar \left|j, m\right\rangle, \\ \hat{J}_\pm \left|j, m\right\rangle = \hbar\sqrt{(j \mp m)(j \pm m + 1)} \left|j, m \pm 1\right\rangle, \end{gathered} \tag{5.6}$$

with the allowed values of

$$m = \underbrace{-j\,,\ -j+1\,,\ \ldots\,,\ j-1\,,\ j}_{2j+1 \text{ states}}, \tag{5.7}$$

where we have switched to the notation $j \equiv b_{\text{max}}/\hbar$ and $m \equiv b/\hbar$.

5.1.1.2 Coupled Basis

Let us now consider two angular-momentum operators $\hat{\boldsymbol{J}}_1$ and $\hat{\boldsymbol{J}}_2$ in different subspaces, such that $\left[\hat{J}_{1,i}, \hat{J}_{2,j}\right] = 0,\ \forall\, i, j$. We now consider the total angular-momentum operator

$$\hat{\boldsymbol{J}} = \hat{\boldsymbol{J}}_1 \otimes \hat{\mathbb{I}}_2 + \hat{\mathbb{I}}_1 \otimes \hat{\boldsymbol{J}}_2 = \hat{\boldsymbol{J}}_1 + \hat{\boldsymbol{J}}_2, \tag{5.8}$$

which satisfies $\left[\hat{\boldsymbol{J}}^2, \hat{\boldsymbol{J}}_1^2\right] = 0$ and Eq. (5.3) for the total generators, but $\left[\hat{\boldsymbol{J}}^2, \hat{J}_{1,i}\right] \neq 0$. There are similar equations for the $\hat{\boldsymbol{J}}_2$ generators. We chose to represent the base kets as eigenstates of $\hat{\boldsymbol{J}}_1^2, \hat{\boldsymbol{J}}_2^2, \hat{\boldsymbol{J}}^2$, and $\hat{J}_z$:

$$\begin{gathered} \hat{\boldsymbol{J}}_1^2 \left|j_1, j_2; J, M\right\rangle = j_1\left(j_1+1\right)\hbar^2 \left|j_1, j_2; J, M\right\rangle, \quad \hat{\boldsymbol{J}}_2^2 \left|j_1, j_2; J, M\right\rangle = j_2\left(j_2+1\right)\hbar^2 \left|j_1, j_2; J, M\right\rangle, \\ \hat{\boldsymbol{J}}^2 \left|j_1, j_2; J, M\right\rangle = J\left(J+1\right)\hbar^2 \left|j_1, j_2; J, M\right\rangle, \quad \hat{J}_z \left|j_1, j_2; J, M\right\rangle = M\hbar \left|j_1, j_2; J, M\right\rangle, \end{gathered} \tag{5.9}$$

---

[1] We make the arbitrary choice of working in the $\hat{J}_z$ basis by convention.

with $M = m_1 + m_2$ and $|j_1 - j_2| \leq J \leq j_1 + j_2$. We usually denote these states simply as $|J, M\rangle$ and assume the j_1 and j_2 values are understood.

A simple example is the singlet-triplet representation of two spin-$\frac{1}{2}$ systems. Here, $j_1 = j_2 = 1/2$ and thus, $|j_1 - j_2| = 0 \leq J \leq j_1 + j_2 = 1$. This leads to four eigenstates $|0,0\rangle, |1,-1\rangle, |1,0\rangle$, and $|1,1\rangle$, which we write out explicitly, with $+ = 1/2$ and $- = -1/2$, as

$$\begin{aligned} |1,-1\rangle = |m_1 = -, m_2 = -\rangle\,,\ |1,0\rangle &= \frac{1}{\sqrt{2}}\left[|m_1 = +, m_2 = -\rangle + |m_1 = -, m_2 = +\rangle\right], \\ |1,1\rangle = |m_1 = +, m_2 = +\rangle\,,\ &\underbrace{|0,0\rangle = \frac{1}{\sqrt{2}}\left[|m_1 = +, m_2 = -\rangle - |m_1 = -, m_2 = +\rangle\right].}_{\text{Spin Singlet}} \end{aligned} \tag{5.10}$$

The states with $J = 1$ are symmetric and are called the spin triplet states. The $J = 0$ state is anti-symmetric and corresponds to the spin singlet state. To add N spins, one first adds $\hat{\boldsymbol{J}}_1$ and $\hat{\boldsymbol{J}}_2$, followed by the addition of $\hat{\boldsymbol{J}}_{12}$ and $\hat{\boldsymbol{J}}_3$, and so on.

5.1.2 Superradiance and Subradiance

Let us now consider an ensemble of N two-level atoms which are modeled as spin-$\frac{1}{2}$ systems. We study atomic states with permutational invariance such that they are indiscernible with respect to photon emission or absorption processes [63, 150]. The symmetric states, called the Dicke states [46], correspond to the largest J value: $J = \sum_{i=1}^{N} j_i = N/2$. The simplest examples of this are the excited $|N/2, N/2\rangle$ and ground state $|N/2, -N/2\rangle$ which corresponds to the N-atom permutation invariant states,

$$\left|J = \frac{N}{2}, M = \frac{N}{2}\right\rangle \equiv |\underbrace{e, e, \ldots, e}_{N}\rangle, \qquad \left|J = \frac{N}{2}, M = -\frac{N}{2}\right\rangle \equiv |g, g, \ldots, g\rangle\,, \tag{5.11}$$

where, for example, $|e, e, \ldots, e\rangle = \bigotimes_{i=1}^{N} |e\rangle_i$. The other Dicke states are given by the “symmetrization operator” $\hat{S}$ [63]:

$$|JM\rangle = \hat{S}[|\underbrace{e, e, \ldots, e,}_{J+M} \quad \underbrace{g, g, \ldots, g}_{J-M}\rangle]. \tag{5.12}$$

A straightforward application of this is for $N = 2$, where the Dicke states are given by the $J = 1$ spin triplet states in Eq. (5.10).

These symmetric states are the superradiant states. To see this, let us define the single-atom spin-flip operators in the n^{th} atom's subspace,

$$\hat{\sigma}_-^{(n)} \equiv \left(\bigotimes_{i=1}^{n-1} \hat{\mathbb{I}}_i \right) \otimes |g\rangle_n \langle e|_n \otimes \left(\bigotimes_{i=n+1}^{N} \hat{\mathbb{I}}_i \right) = |g\rangle_n \langle e|_n = \left[\hat{\sigma}_+^{(n)} \right]^\dagger , \tag{5.13}$$

to introduce the collective operators,

$$\hat{J}_\pm = \sum_{n=1}^{N} \hat{\sigma}_\pm^{(n)}. \tag{5.14}$$

Assuming every excited state has linewidth $\mathit{\Gamma}$, the rate of photon emission from N atoms is

$$R_N^s = \mathit{\Gamma} \langle \hat{J}_+ \hat{J}_- \rangle = \mathit{\Gamma} \left(J + M \right) \left(J - M + 1 \right), \tag{5.15}$$

which, for $J = N/2$, demonstrates that the photon emission rate greatly increases, with a maximum rate proportional to N^2, until it reaches the ground state [63], as depicted in Fig. 5.2. This demonstrates the collective enhancement of spontaneous emission by way of interatomic coherence.

As demonstrated by the spin singlet state in Eq. (5.10), lower values of J can be obtained through superpositions of atomic states. The subradiant state $J = 0$ is called the subradiant state as it only has one M value, i.e.,

$$\hat{J}_\pm |0, 0\rangle = 0, \tag{5.16}$$

and thus, $R_N^s = 0$ in spite of nearly half the atoms being in the excited state [90]. This illustrates the suppression of spontaneous emission due to interatomic decoherence, and the $|0, 0\rangle$ dark state is the target state in the next section.

5.1.3 Permutation Invariant Simulations

The irreducible Hilbert space of the N permutation invariant two-level atoms obviously has a 2^N dimensionaity [9]. While numerical calculations can now be preformed in this uncoupled basis, the exponential scaling of the Hilbert space can make simulations quickly intractable for all but the smallest N values [151, 126]. This is compounded when studying open quantum systems as the Liouvillian space scales as 4^N. Therefore, we instead take advantage of the permuational, SU(4)

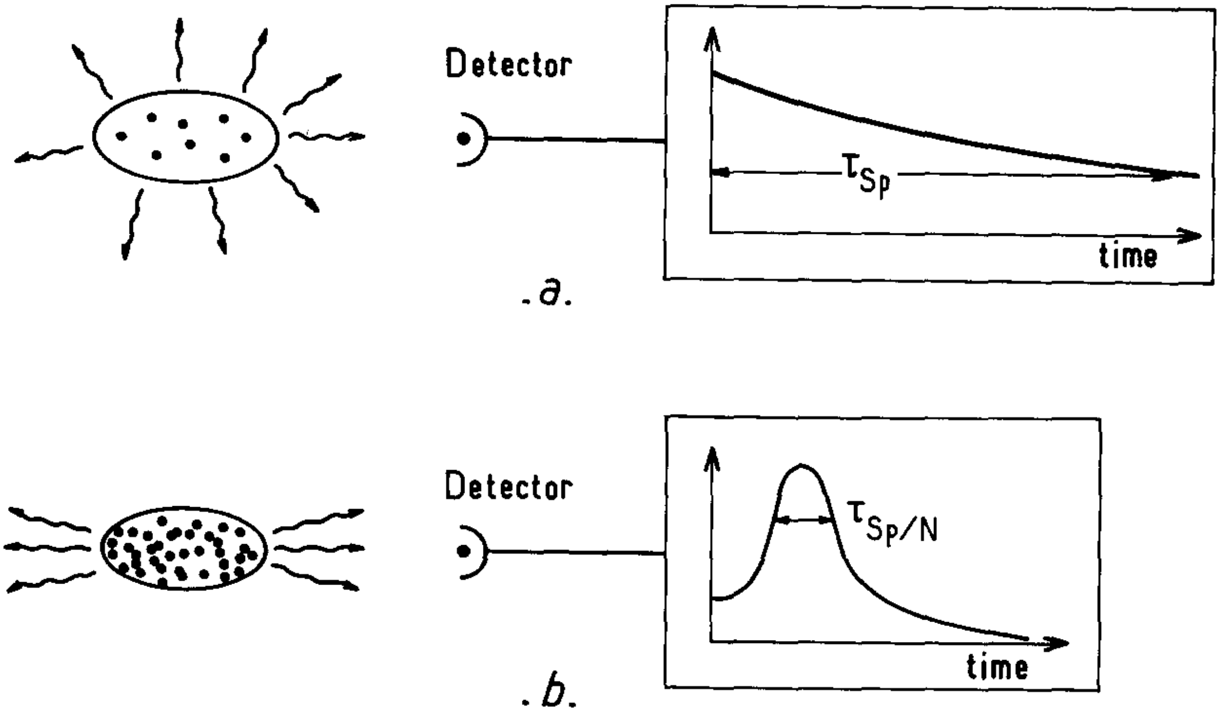

0.7

Figure 5.2: Source: Ref. [63]. Comparision of the general characteristics of ordinary fluorescence (a) and superradiant fluorescence (b) for decay time $\tau_{\mathrm{Sp}} = 1/\mathit{\Gamma}$.

symmetry that the system possesses to map its generators (the Gell-Mann matrices) to the coupled basis [151, 126]. Here, we note that the density matrix takes block diagonal form as no coherences are created when we project $\hat{\rho}$ into the Dicke basis [126]:

$$\hat{\rho} = \sum_{\pi} \hat{P}_\pi \hat{\rho} \hat{P}_\pi^\dagger = \sum_{J,J',M,M'} \rho_{J,J',M,M'} \left| J, M \middle\rangle\!\middle\langle J', M' \right| \delta_{J,J'}, \tag{5.17}$$

where $\hat{P}_\pi$ is the permutation operator for permutation π, $\delta_{i,j}$ is the Kronecker delta, and $\rho_{J,J',M,M'} = \langle J, M | \, \hat{\rho} \, | J', M' \rangle$. There is a

$$d_N^J = \frac{N!(2J+1)}{\left(\frac{N}{2} + J + 1\right)! \left(\frac{N}{2} - J\right)!} \tag{5.18}$$

degeneracy of each $|J, M\rangle$ Dicke state. We note that the state in the limit of infinite temperature $T \to \infty$ is given by

$$\hat{\rho}_{T\to\infty} = \sum_{J,M} \frac{d_N^J}{2^N} \left| J, M \middle\rangle\!\middle\langle J, M \right|, \tag{5.19}$$

as every state is equally occupied with a d_N^J degeneracy and normalization factor of 2^{-N}. Each "Dicke block" has $(2J+1)$ values of M [see Eq. (5.7)] which therefore allows us to work with a reduced density matrix with only $\sum_{J=0}^{N/2}(2J+1)^2 = (1/6)(N+1)(N+2)(N+3) = \mathcal{O}(N^3)$ total elements. This work has been collectivized into QuTip's permutational invariant quantum solver in Python [126] which is the core of my simulations.

5.2 Enhancement and Selection of $J = 0$ State

With these preliminaries complete, we now turn our attention to a specific model that operates in the bad-cavity limit. It has been shown that this system can achieve steady-state superradiance [92, 91, 90, 150], as well as lasing [23, 109], for intermediate repump rates. We instead focus, in this section, on the weak pumping limit in which the $J = 0$ state population is greatly enhanced. We then demonstrate a photon detection scheme that isolates the subradiant state from the steady-state of this previous model.

5.2.1 Superradiant Lasing Model

We now consider the simple steady-state superradiance model proposed [92] and developed [91, 90] to achieve lasing by Dominic Meiser, Jun Ye, and Murray Holland. The model was further expended by Minghui Xu [150, 151], David Tieri [139, 140], James Thompson [23], and Matt Norcia [109]. A schematic of the model is depicted in Fig. 5.3, and I will refer to the system as the *superradiant lasing model.*

5.2.1.1 System Dynamics

An ensemble of N atoms are, ideally, collected at the anti-nodes of a cavity mode so that they have an identical cavity-coupling constant g [see Eq. (4.17)]. Each atom has excited and ground states $|e\rangle$ and $|g\rangle$, separated by the atomic frequency ω_a, and an excited state linewidth $\mathit{\Gamma}$. The many-body Hamiltonian is given by

$$\hat{H} = \hbar\omega_a \hat{J}_z + \hbar\omega_c \hat{a}^\dagger \hat{a} + \frac{\hbar g}{2}\left(\hat{a}^\dagger \hat{J}_- + \hat{a}\hat{J}_+\right), \tag{5.20}$$

with cavity frequency ω_c and collective z-operator

$$\hat{J}_z = \frac{1}{2}\sum_{i=1}^{N} \hat{\sigma}_z^{(i)} = \frac{1}{2}\sum_{i=1}^{N} |e\rangle_i \langle e|_i - |g\rangle_i \langle g|_i \,. \tag{5.21}$$

The cavity field decays at a rate κ and its output can be monitored by two detectors D_1 and D_2 with a variable delay time τ between them. When the decay from the atomic ensemble is collectively enhanced through a cavity, we can assume that the spontaneous decay into free space $\mathit{\Gamma}$ can be neglected. This comes from the approximation $N\mathcal{C} \gg 1$, where $\mathcal{C} = g^2/(\kappa\mathit{\Gamma}) \propto 1/N_0$ is the single atom cooperativity parameter with critical atom number N_0.

We also include an incoherent process that represents noncollective pumping at rate w with jump operator $\hat{\sigma}_+^{(n)}$ for each atom. Here, the repumping can be implemented by coherently driving, at a rate $\mathit{\Omega}_p$, a transition between $|g\rangle$ and an auxiliary state $|a\rangle$. This state then decays, at a rate γ_p, to the $|e\rangle$ state, as shown in Fig. 5.4. Note that, in the limit of large γ_p, this leads to an effective pumping rate $w = |\mathit{\Omega}_p|^2/\gamma_p$ [150]. We choose to ignore the effects of incoherent dephasing of the

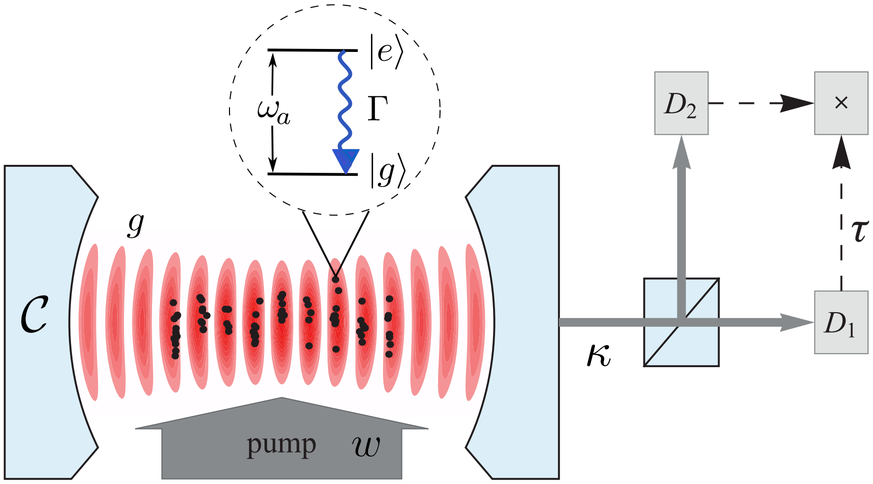

Figure 5.3: Source: Ref. [90]. Schematic diagram of the superradiant lasing model. N two-level atoms (black dots with internal structure given in the inset) with individual decay rate Γ are collected at the anti-nodes of a single-mode cavity field. The cavity has single atom cooperativity parameter $\mathcal{C}$, decay rate κ, and coupling constant g. The atoms are incoherently repumped at a rate w. The output of the cavity field is monitored by two detectors D_1 and D_2 with a variable time delay τ between them.

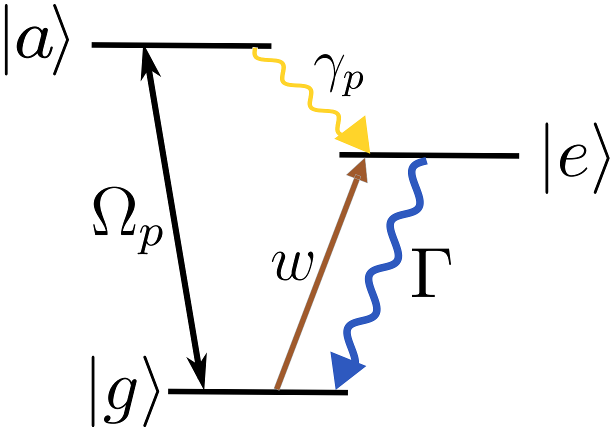

Figure 5.4: Source: Ref. [91, 150]. Schematic diagram for implementing the incoherent pumping scheme with a three-level atom at an effective rate $w = |\Omega_p|^2/\gamma_p$ (brown arrow). The atoms are coherently pumped (black arrow) from the ground state $|g\rangle$ to the auxiliary state $|a\rangle$ at a rate Ω_p. This then decays to the excited state $|e\rangle$ at a rate γ_p (yellow arrow). This can then decay back to the ground state at an individual decay rate Γ (blue arrow).

atomic dipole (with jump operator $\hat{\sigma}_z^{(n)}$) by assuming its characteristic time T_2 is very long. Thus, the system's master equation Eq. (3.33) is written in Lindblad form as

$$\frac{\partial \hat{\rho}}{\partial t} = \frac{1}{i\hbar}\left[\hat{H}, \hat{\rho}\right] + \kappa \hat{\mathcal{D}}[\hat{a}]\hat{\rho} + \sum_{i=1}^{N} w \hat{\mathcal{D}}[\hat{\sigma}_+^{(i)}]\hat{\rho}, \tag{5.22}$$

with Lindblad superoperators in the form of Eq. (3.34).

As it turn out, the problem can be simplified further by exploiting the fact that the cavity field decays much faster than the atomic coherence [90], and therefore is suitable for adiabatic elimination [24, 36]. The validity of the assumption that the intensity decay rate is much larger than atomic rates takes the form

$$\kappa \gg N\mathcal{C}\mathit{\Gamma}. \tag{5.23}$$

This is the so-called bad-cavity limit. Elimination of the light field yields [90], in the so-called "dissipation picture",

$$\begin{aligned} \frac{\partial \tilde{\hat{\rho}}}{\partial t} &= \mathit{\Gamma}_c \hat{\mathcal{D}}[\hat{J}_-]\tilde{\hat{\rho}} + \sum_{i=1}^{N} w \hat{\mathcal{D}}[\hat{\sigma}_+^{(i)}]\tilde{\hat{\rho}} \\ &= \mathit{\Gamma}_c \left(\hat{J}_- \tilde{\hat{\rho}} \hat{J}_+ - \frac{1}{2}\{\hat{J}_+\hat{J}_-, \tilde{\hat{\rho}}\} \right) + w \left(\sum_i \hat{\sigma}_+^{(i)} \tilde{\hat{\rho}} \hat{\sigma}_-^{(i)} - \frac{1}{2}\{\hat{\sigma}_-^{(i)}\hat{\sigma}_+^{(i)}, \tilde{\hat{\rho}}\} \right), \end{aligned} \tag{5.24}$$

where the collective decay rate of the atoms through the cavity is given by

$$\mathit{\Gamma}_c = \mathcal{C}\mathit{\Gamma} = \frac{g^2}{\kappa}. \tag{5.25}$$

We are now in a position to only study the dynamics of the atomic evolution as the cavity has effectively become a decay channel for the atoms with jump operator $\hat{J}_-$. Based on [154], I include a Dicke-state diagram (see Fig. 5.5) and a table (see Table. 5.1) listing the different decay processes that have been discussed. We can now consider numerical results of Eq. (5.24).

5.2.1.2 Second-Order Correlation Function

To motivate the usefulness of the superradiant lasing model, we will discuss fluctuations of the light intensity in a similar manner to [90]. By using a Hanbury Brown-Twiss photodetector setup (see right side of Fig. 5.3), one can measure a joint probability $P_2(t, t+\tau)$ of detecting a photon in

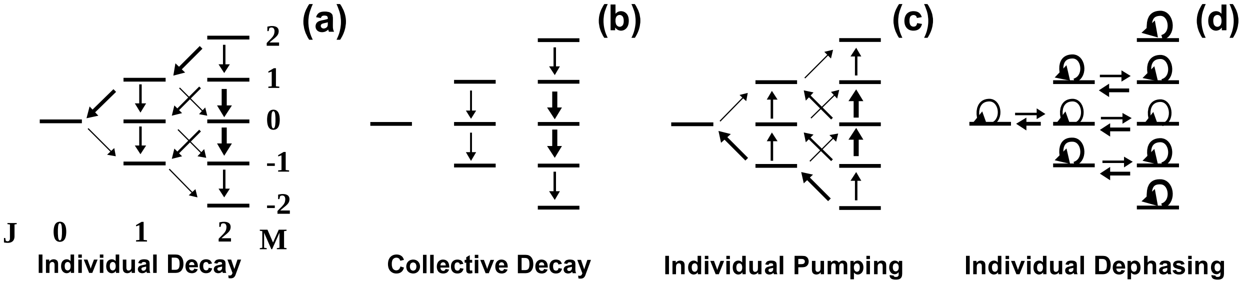

Figure 5.5: Source: Ref. [154]. Dicke ladder diagrams with $N = 4$ for (a) individual decay, (b) collective decay through the cavity, (c) individual pumping, and (d) individual dephasing. The thickness of the arrows indicates the probabilities of the different jumps (see, for example, Table 5.2).

Dissipation	Rate	Jump Operator	Jump
Individual decay	Γ	$\hat{\sigma}_-^{(n)}$	$(J,M) \to (J,M-1)$ $(J,M) \to (J-1,M-1)$ $(J,M) \to (J+1,M-1)$
Collective decay	Γ_c	$\hat{J}_- = \sum_n \hat{\sigma}_-^{(n)}$	$(J,M) \to (J,M-1)$
Individual pumping	w	$\hat{\sigma}_+^{(n)}$	$(J,M) \to (J,M+1)$ $(J,M) \to (J-1,M+1)$ $(J,M) \to (J+1,M+1)$
Individual dephasing	$\frac{1}{T_2}$	$\frac{1}{2}\hat{\sigma}_z^{(n)}$	$(J,M) \to (J,M)$ $(J,M) \to (J-1,M)$ $(J,M) \to (J+1,M)$

Table 5.1: Source: Ref. [154]. Table of quantum jumps resulting from the jump operator associated for the different dissipative processes we consider.

two separate time intervals $P_1(t)$. We express this as the second-order correlation function, given by [60]

$$g^{(2)}(t,\tau) = \frac{P_2(t,t+\tau)\mathit{\Delta} t\mathit{\Delta}\tau}{P_1(t)\mathit{\Delta} t P_1(t+\tau)\mathit{\Delta}\tau} = \frac{\langle \hat{a}^\dagger(t)\hat{a}^\dagger(t+\tau)\hat{a}(t+\tau)\hat{a}(t)\rangle}{\langle \hat{a}^\dagger(t)\hat{a}(t)\rangle\langle \hat{a}^\dagger(t+\tau)\hat{a}(t+\tau)\rangle}, \tag{5.26}$$

which is a measure of detecting a photon both in a time interval $\mathit{\Delta} t$ at time t and $\mathit{\Delta}\tau$ at time $t+\tau$. In steady-state, this does not depend on t [90], so we simply write $g^{(2)}(\tau)$. In Fig. 5.6, we plot the second-order correlation function as a function of repump rate at zero time delay, which is related to fluctuations of the photon flux $\hat{I}$:

$$\mathit{\Delta} I^2 = \langle \hat{I}^2\rangle - \langle \hat{I}\rangle^2 = \langle \hat{I}\rangle^2 \left[g^{(2)}(0) - 1\right] + B\langle \hat{I}\rangle \tag{5.27}$$

for detection bandwidth B. Here, we are able to write

$$g^{(2)}(0) = \frac{\langle \hat{J}_+\hat{J}_+\hat{J}_-\hat{J}_-\rangle}{\langle \hat{J}_+\hat{J}_-\rangle^2}, \tag{5.28}$$

as, in the bad-cavity limit Eq. (5.23), the cavity field is slaved to the atomic dipoles [90]:

$$\hat{a} \cong \frac{g}{i\kappa}\hat{J}_-. \tag{5.29}$$

When $g^{(2)}(0) = 1$ (blue dotted line), the field is in a coherent state and photons have a mean rate of arrival of $\langle \hat{I}\rangle$ which is often a sign of lasing. A large second-order correlation function $g^{(2)}(0) > 1$ has super-Poissonian properties, which indicates that photons will arrive in bunches. For a thermal state, which occurs in the limit of very strong pumping $w \gg \mathit{\Gamma}_c$, this behavior reaches a maximum of $g^{(2)}(0) = 2$ (dotted orange line). In contrast, the second-order correlation function can reach higher values in the weak pumping regime $w \leq \mathit{\Gamma}_c$. As discussed in the next subsection, this is because the system has evolved into near subradiant, collective dark states [17, 106] in which the emission of photons is highly suppressed.

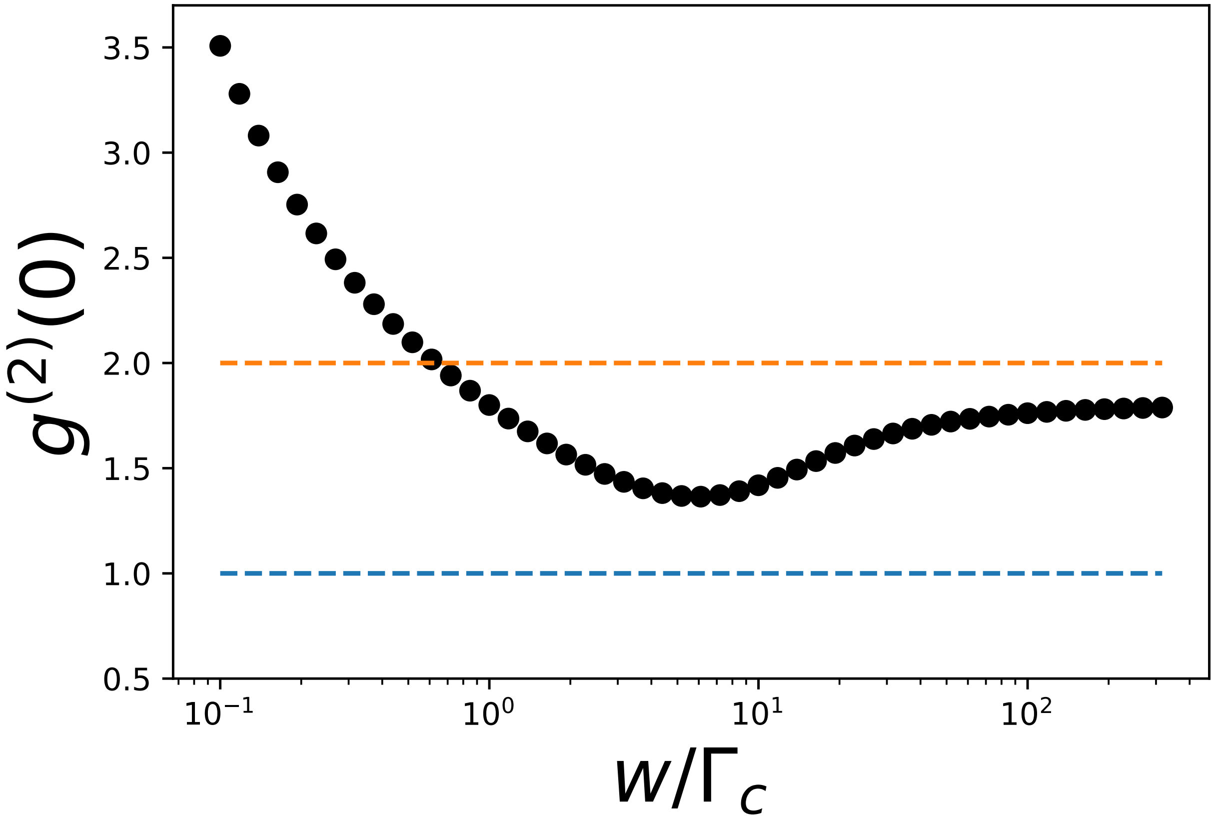

Figure 5.6: Source: Ref. [90]. Second-order intensity correlation function $g^{(2)}(0)$ as a function of repump rate for $N = 10$. Results were calculated using Eq. (5.28) and the dissipative picture master equation Eq. (5.24).

5.2.2 Subradiant State Enhancement

5.2.2.1 $N = 2$ Case

We first simulate the case of two atoms ($N = 2$) so that we may use the singlet-triplet spin language. Throughout this subsection, our simulations initialize the state along the diagonal in the $J = N/2$ manifold, which we demonstrate in Fig. 5.7(a) by initializing it in the excited state $|1,1\rangle$. No matter the choice, the system reaches a unique steady-state, which we investigate in the weak pumping regime. Fig. 5.7(b) demonstrates the final state $\hat{\rho}_{ss}$ of the system for the choice $w = 0.1\mathit{\Gamma}_c$. Here, almost all of the population ends in the $|1,-1\rangle$ and $|0,0\rangle$ states, both of which have final populations of 0.464. This is a slight enhancement over the $2^{-2} = 0.25$ population in the $J = 0$ state for the infinite temperature state $\hat{\rho}_{T\to\infty}$ [see Eq. (5.19)]. We study this enhancement further in the next subsubsection.

First, we can now discuss the significance of a large $g^{(2)}(0)$ function in the weak pumping regime. Let us take the limit that $w/\mathit{\Gamma}_c \to 0$ [138, 91, 90]. Here, the population is pumped entirely into the $|1,-1\rangle$ and $|0,0\rangle$ states. Fig. 5.5 demonstrates that this state may only be pumped into the $|1,1\rangle$ state (as collective decay dominates the $|1,-1\rangle \leftrightarrow |1,0\rangle$ transition when $w/\mathit{\Gamma}_c \approx 0$). From $|1,1\rangle$, the atoms collectively decay back to the $|1,-1\rangle$ state by way of a quick photon cascade on a time scale $\mathcal{O}(\mathit{\Gamma}_c^{-1})$. This in itself has potential quantum metrological applications as one would expect this collective dark state is robust to perturbations of the system. In particular, when the system is perturbed, such as a single atom dephasing event, there is an avalanche of photons until the system finds its way back to the collective dark state, suggesting that there can be a large output signal from a small perturbation. However, we do not pursue this potential project here.

5.2.2.2 Many-body Case

Having now demonstrated the subradiant state enhancement in the weak pumping limit with two atoms, let us explore how the subradiant population changes as a function of atom number. We choose to set the repump rate to be $w = \mathit{\Gamma}_c/N$. As demonstrated in Fig. 5.8, the steady-

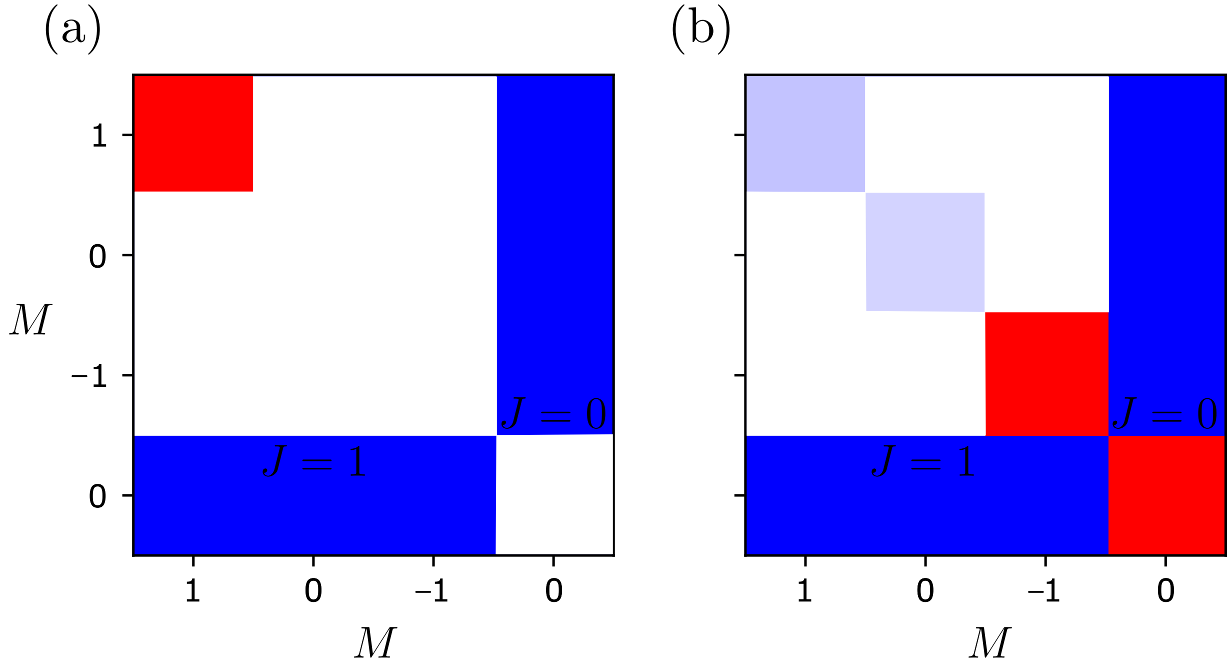

Figure 5.7: Example of the time evolution of the density matrix in the superradiant lasing model with $N = 2$ and repump rate $w = 0.1\Gamma_c$. The red areas indicate highly populated states. (a) The system may, for example, begin in the excited state $\hat{\rho}(0) = |1,1\rangle\langle 1,1|$. (b) No matter the initial state, the system evolves under Eq. (5.24) to a unique steady-state $\hat{\rho}_{ss}$. Also displayed is the block diagonal form of the density matrix in the Dicke basis where the different blocks represent different J manifolds.

Dissipation	Jump	Jump Probability
Collective decay	$(J,M) \to (J,M-1)$	$\mathit{\Gamma}_c(J+M)(J-M+1)d_N^J\delta t$
Individual pumping	$(J,M) \to (J,M+1)$	$w\frac{(2+N)(J-M)(J+M+1)}{4J(J+1)}d_N^J\delta t$
	$(J,M) \to (J-1,M+1)$	$w\frac{(N+2J+2)(J-M)(J-M-1)}{4J(J+1)}d_N^J\delta t$
	$(J,M) \to (J+1,M+1)$	$w\frac{(N-2J)(J+M+1)(J+M+2)}{4(J+1)(2J+1)}d_N^J\delta t$

Table 5.2: Source: Ref. [154]. Table of the transition probabilities in a short time interval δt associated with the quantum jumps involved in the superradiant lasing model. Here, d_N^J is the degeneracy of the specific J manifold, given by Eq. (5.18).

state value of the $J = 0$ state population in the infinite temperature case (red dots) scales like a polynomial of N. Meanwhile, the subradiant population in the superradiant lasing scheme (black dots) approximately saturates at around $N = 10$. This leads to an order of magnitude improvement using the superradiant lasing model for the case of $N = 20$.

We preform a more thorough investigation into the system's parameter space in the contour plot presented in Fig. 5.9. This confirms the manifestation of an apparent "enhancement threshold" in the weak pumping regime at which the steady-state $J = 0$ state population significantly falls off. Fig. 5.9 also suggests that the threshold value is approximately linear with N and that, for a given N, the subradiant state overlap does not vary much with N below this threshold.

Expanding on the idea of a threshold approximately linear with N, we look at the transition rates for each jump associated with collective decay and individual pumping. Table 5.2 displays the jump probabilities of each jump in a short time interval δt for a $|J,M\rangle$ state with degeneracy d_N^J given by Eq. (5.18). Interestingly, the transition rates for the individual repumping jumps increase with N while the collective decay probability does not. This suggests that the enhancement threshold value occurs at

$$w \approx \mathit{\Gamma}_c/N. \tag{5.30}$$

This motivated our choice of repump rate in Fig. 5.8 as $w/(\mathit{\Gamma}_c/N)$ seems to be the natural scaling

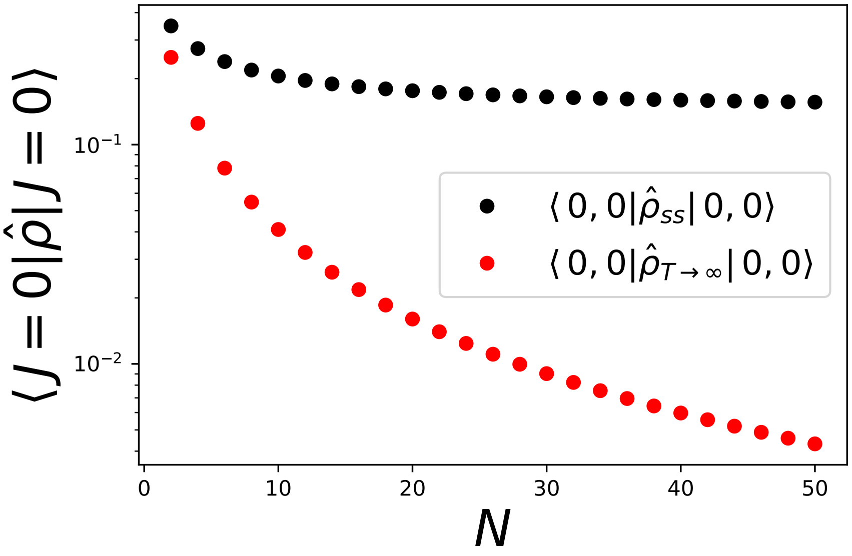

Figure 5.8: The population of the $J = 0$ state as a function of the atom number. The values of the superradiant lasing scheme (black dots) are given by the steady-state of Eq. (5.24), while the infinite temperature state values (red dots) are calculated by Eq. (5.19). The repump rate for each N is given by $w = \Gamma_c/N$.

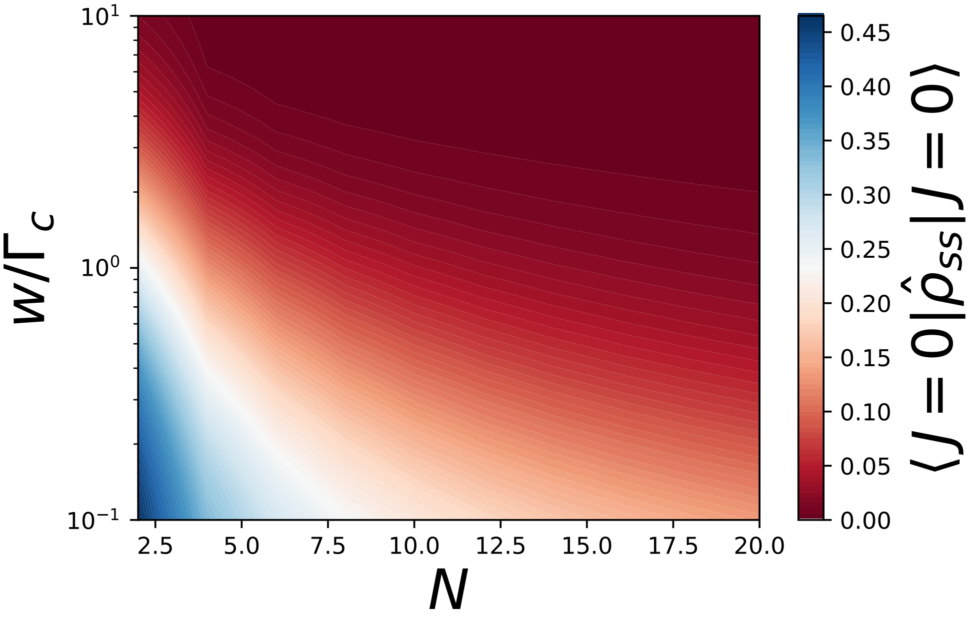

Figure 5.9: Contour plot of the steady-state subradiant state population as a function of atom number N and repump rate w.

for the repump strength in the subradiant regime, similar to $w/(N\mathit{\Gamma}_c)$ in the superradiant regime. We test this conclusion by plotting the steady-state $J = 0$ population as a function of $w/(\mathit{\Gamma}_c/N)$ in Fig. 5.10(a). It is clear that the steady-state subradiant state population begins to sharply decrease for every N value at the enhancement threshold predicted in Eq. (5.30), while the value for a given N remains approximately constant below the threshold. Moreover, Fig. 5.10(c) shows that the population below threshold ends up almost entirely in the lowest M value of each Dicke block. We investigate this point further in Fig. 5.10(d). Here, we demonstrate that the population not only evolves to the lowest M value in each block, but that the population head towards lower J values as well, ending up almost entirely in the $|0, 0\rangle$ and $|1, -1\rangle$ states. This is because, for $M < 0$ in the weak pumping limit, the repumping predominantly drives $J \to J - 1$ transitions rather than $J \to J + 1$ transitions [91], as is demonstrated by the darker arrows towards lower J values in Fig. 5.5(c).

We also show in Fig. 5.10(b) that the expectation value $\langle \hat{J}_+ \hat{J}_- \rangle$ becomes $\mathcal{O}(1)$ at the enhancement threshold. This offers significant insight into the dynamics of the system, as this is related to $\langle \hat{a}^\dagger \hat{a} \rangle$ [see Eq. (5.29)]. As displayed in Fig. 5.5(c), the repump couples the states with the lowest M values in each Dicke block to higher M values in the same J manifold. However, these states decay too fast in the weak pumping limit as $\mathit{\Gamma}_c$ dominates over w. When the repump rate becomes large enough to put at least one atom in the excited state in the timescale $1/\mathit{\Gamma}_c$, one excitation in the field becomes possible. Since the probability of finding an atom in the excited state is $\sim w/\mathit{\Gamma}_c$, we see that the total excited state population for N atoms becomes $Nw/\mathit{\Gamma}_c$. Therefore, the system will begin to leave the collective dark state when $Nw/\mathit{\Gamma}_c \approx 1$, which is consistent with our enhancement threshold.

The upside of the enhancement of the subradiant state in the weak pumping limit is best understood in the language of Monte Carlo wave functions [see Appendix C.2]. In the infinite temperature case and for $N = 50$, only one out of $1/(d^0_{50} 2^{-50}) \approx 231$ trajectories will result in the $J = 0$ state at the end of a stochastic shot. On the contrary, one out of every five trajectories end in the subradiant state in the the superradiant lasing model which is now an experimentally

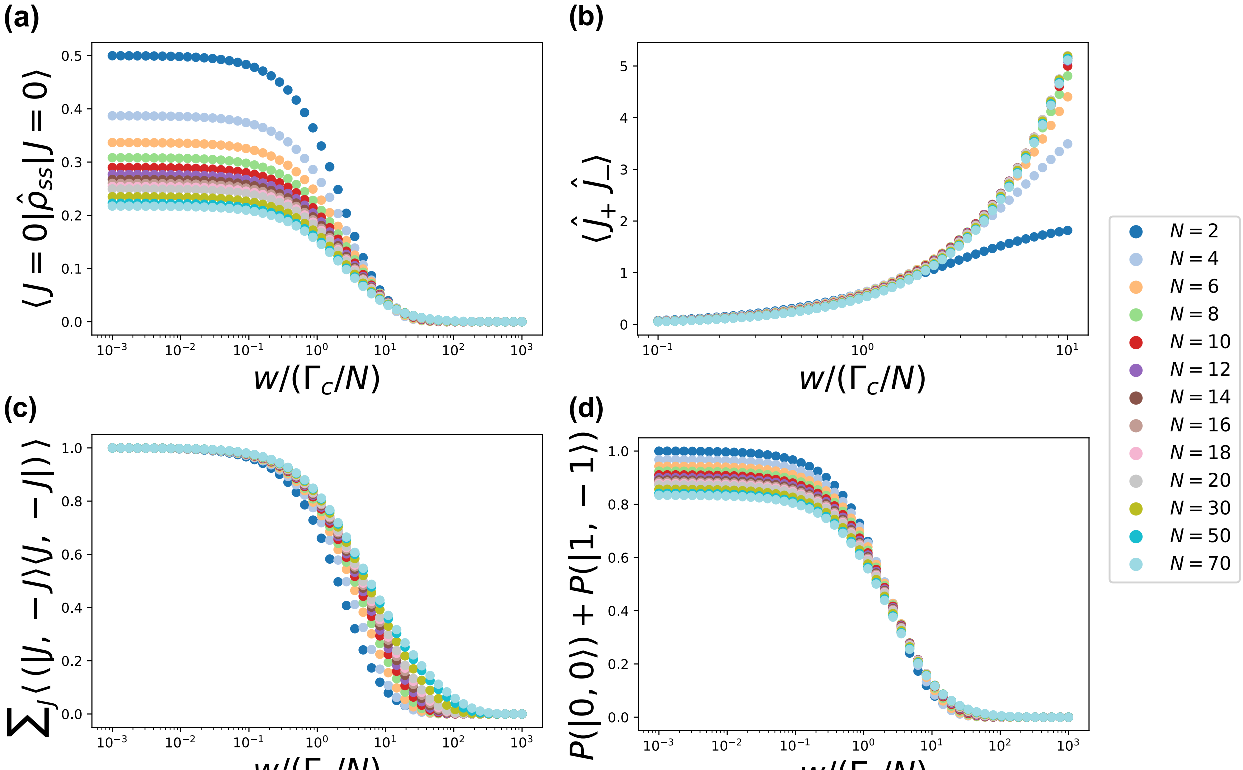

Figure 5.10: Verification of an "enhancement threshold" near $w = \Gamma_c/N$, as displayed by the significant change of behavior in steady-state near this region. Each subfigure contains plots for N values in the set $\{2, 4, 6, \ldots, 18, 20, 30, 50, 70\}$. (a) Steady-state population in the $J = 0$, subradiant state. (b) Expectation value $\langle \hat{J}_+\hat{J}_-\rangle$ in steady-state near the threshold, which is related to $\langle \hat{a}^\dagger \hat{a}\rangle$. (c) Sum of the steady-state probabilities in the states with the lowest M value of each Dicke block. (d) Sum of the steady-state probabilities in the $|0, 0\rangle$ and $|1, -1\rangle$ states.

viable proposal. Thus, this enhancement is necessary for the subradiant state selection by photon detection protocol that we present in the next subsection.

5.2.3 Detection Phase

We can now present a novel protocol that can extract the subradiant state from the atomic mixture. For simplicity, we consider the $N = 2$ case, but the conclusions drawn extends to higher atom numbers. To differentiate between the $J = 0$ and $J = 1$ manifolds, we introduce a coherent drive

$$\hat{H}_d = \hbar \mathit{\Omega} \hat{J}_x = \frac{\hbar \mathit{\Omega}}{2} \left(\hat{J}_+ + \hat{J}_- \right). \tag{5.31}$$

Therefore, the subradiant state will remain unchanged [see Eq. (5.16)] by the system's coherent dynamics, in the dissipation picture. We, once again, turn our attention to Fig. 5.5 to determine the necessary incoherent dynamics. Since we want a scheme that does not affect the subradiant state population, we only allow for collective emission through the cavity, and therefore turn the repumping laser off ($\mathit{\Omega}_p = 0$). The detection-phase master equation, in the dissipation picture, is thus

$$\frac{\partial \tilde{\hat{\rho}}}{\partial t} = \frac{1}{i\hbar} \left[\hat{H}_d, \tilde{\hat{\rho}} \right] + \mathit{\Gamma}_c \left(\hat{J}_- \tilde{\hat{\rho}} \hat{J}_+ - \frac{1}{2} \{ \hat{J}_+ \hat{J}_-, \tilde{\hat{\rho}} \} \right). \tag{5.32}$$

Here, $\tilde{\hat{\rho}}$ is initialized as the steady-state density matrix $\hat{\rho}_{ss}$ of the superradiant lasing scheme. Numerical results for this interaction are presented in Fig. 5.11 with total time $t_f = 10/\mathit{\Gamma}_c$, $N = 2$, and $\mathit{\Omega} = \mathit{\Gamma}_c$. It is clear that the $J = 0$ state population has remained constant during the process, while the populations in the $J > 0$ manifolds are displaced from their steady-state values in the superradiant lasing model $\hat{\rho}_{ss}$.

Let us again frame our discussion in a quantum trajectories picture. If a single emitted photon is detected, the prescribed system dynamics indicates that the state was in a $J > 0$ manifold and that run is removed. However, in the limit $t \to \infty$, a system that does not emit a photon is necessarily in the subradient state. Since the $J = 0$ state population does not change during the interaction, the absence of any photodetection events should occur $n_{\text{trj}} \langle 0, 0 | \hat{\rho}_{ss} | 0, 0 \rangle$ times in n_{trj}

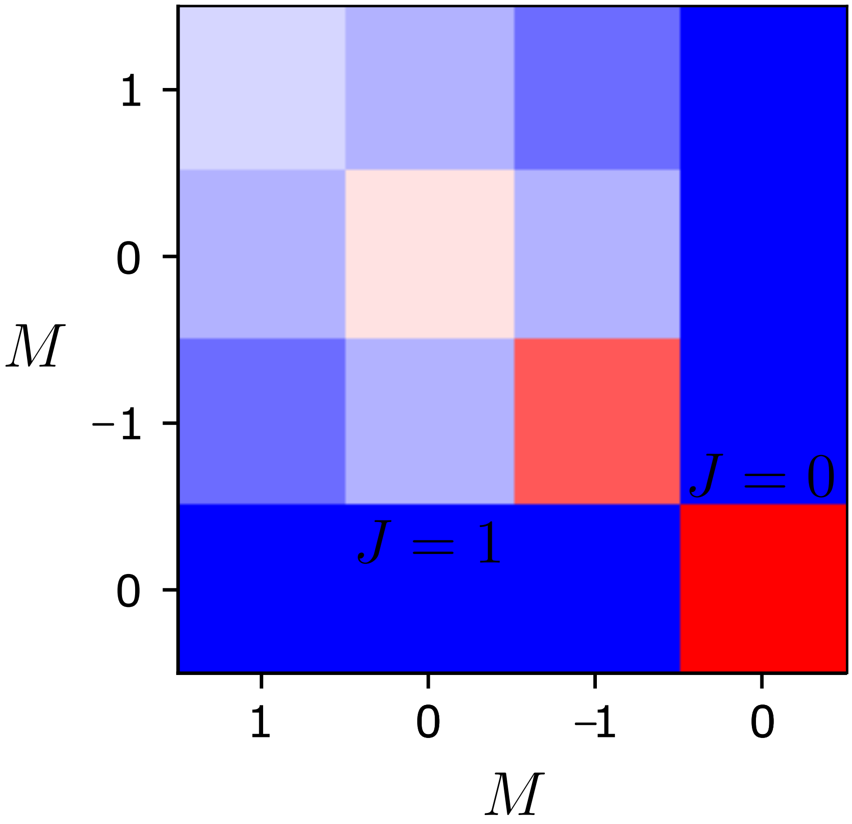

Figure 5.11: Density matrix after the detection phase for $N = 2$, $\Omega = \Gamma_c$, and $w = 0$. The system is initialed in the steady-state of the superradiant lasing model from Fig. 5.7 and evolved under the detection phase master equation Eq. (5.32) for a total time $t_f = 10/\Gamma_c$. The red areas indicate highly populated states.

trajectories. This demonstrates why we first drive the system in the weak pumping limit with the superradiant lasing model to enhance the initial $J = 0$ value for our proposed detection scheme.

5.3 Outlook

We have therefore shown that by first enhancing the subradiant state population in the weak pumping regime, a photodetection test can be used to isolate this $J = 0$ state in an experimentally viable number of iterations. We can now relate our proposed scheme to the idea of entropy reduction as we are driving the system toward a pure state, up to the subradiant state degeneracy. Furthermore, we can create an analogue to evaporative cooling as the incoherent pumping in the initial phase plays the role of atomic collisions, leading to compression towards lower J and M values. Meanwhile, the detection phase is analogous to lowering the trap depth to allow hot atoms to escape, as trajectories with one or more photodetection events are disregarded and only trajectories in the $J = 0$ state are keep.

While these preliminary results suggest the $J = 0$ state may be isolated in an experimental setting, what we have presented is just the tip of the iceberg. There are two possible avenues to pursue with this project. One route is to present our work as the first detailed exploration of the subradiant regime. We could, for instance, investigate how the slopes in Fig. 5.10 vary as we change N. We are also studying an analytical solution for the steady-state $J = 0$ population in the limit $w/(\mathit{\Gamma}_c/N) \to 0$. The other approach is to present our work as an experimental proposal. In this case, future work will be dedicated mostly to the detection phase where we would optimize the time for each trajectory. Furthermore, a proposal to test experimentally if the acquired trajectory is truly in $J = 0$ would most likely be needed.

For both approaches, it is thought-provoking to try and enhance the subradiant state further by including more incoherent processes. For example, keeping the incoherent pump on during the detection phase would allow population to exit the $J = 0$ manifold. However, the fact that transition rates towards lower J values are dominant in the weak pumping regime suggests that compression towards $J = 0$ might allow for a even larger subradiant state population. We can then look for entanglement [143] in the system as well as applications of the subradiant state in quantum metrology [56].

Chapter 6

Conclusion

In Chapter 1, we listed three areas of study for the dynamics of cooling particle ensembles. As a precursor to laser cooling, we presented a novel scheme in Chapter 3 to create nearly-coherent laser slowing protocols utilizing adiabatic shortcuts. We were therefore able to create slowing techniques with scattered photon numbers on the order of unity for a large amount of momentum removal. We demonstrated in Chapter 4 that in the laser cooling stage, contrary to popular belief, the laser fields are able to remove part of the entropy initially in the atomic system. In doing so, we directly demonstrated the creation of a low entropy, near-pure atomic state during the cooling process. We created another low entropy state in Chapter 5, this time by driving the system in the weak pumping limit of the steady-state superradiance model. Furthermore, we demonstrated that the population of the subradiant state in greatly enhanced and may be separated from the remainder of the ensemble in an experimentally viable number of stochastic shots. We hope that the creation of many-spin dark states will allow for an improvement on quantum control during quantum metrological investigations.

Bibliography

[1] Obinna Abah, Ricardo Puebla, Anthony Kiely, Gabriele De Chiara, Mauro Paternostro, and Steve Campbell. Energetic cost of quantum control protocols. New Journal of Physics, 21(10):103048, oct 2019.

[2] C. Adami and N. J. Cerf. von neumann capacity of noisy quantum channels. Phys. Rev. A, 56:3470–3483, Nov 1997.

[3] G. S. Agarwal and K. Tara. Nonclassical properties of states generated by the excitations on a coherent state. Phys. Rev. A, 43:492–497, Jan 1991.

[4] G.S. Agarwal. Quantum Optics. Quantum Optics. Cambridge University Press, 2013.

[5] Y. Aharonov and D. Bohm. Significance of electromagnetic potentials in the quantum theory. Phys. Rev., 115:485–491, Aug 1959.

[6] Nitzan Akerman, Michael Karpov, Liron David, Etay Lavert-Ofir, Julia Narevicius, and Edvardas Narevicius. Simultaneous deceleration of atoms and molecules in a supersonic beam. New Journal of Physics, 17(6):065015, jun 2015.

[7] Leslie Allen and Joseph H. Eberly. Optical Resonance and Two-level Atoms. Dover, 1987.

[8] M. H. Anderson, J. R. Ensher, M. R. Matthews, C. E. Wieman, and E. A. Cornell. Observation of bose-einstein condensation in a dilute atomic vapor. Science, 269(5221):198–201, 1995.

[9] F. T. Arecchi, Eric Courtens, Robert Gilmore, and Harry Thomas. Atomic coherent states in quantum optics. Phys. Rev. A, 6:2211–2237, Dec 1972.

[10] G.B. Arfken and H.J. Weber. Mathematical Methods for Physicists. Academic Press, 1985.

[11] M. Arnal, V. Brunaud, G. Chatelain, C. Cabrera-Gutiérrez, E. Michon, P. Cheiney, J. Billy, and D. Guéry-Odelin. Evidence for cooling in an optical lattice by amplitude modulation. Phys. Rev. A, 100:013416, Jul 2019.

[12] S. Balasubramanian, Shuyang Han, B. T. Yoshimura, and J. K. Freericks. Bang-bang shortcut to adiabaticity in trapped-ion quantum simulators. Phys. Rev. A, 97:022313, Feb 2018.

[13] John P. Bartolotta and Murray J. Holland. Sawtooth-wave adiabatic passage in a magneto-optical trap. Phys. Rev. A, 101:053434, May 2020.

[14] John P. Bartolotta, Matthew A. Norcia, Julia R. K. Cline, James K. Thompson, and Murray J. Holland. Laser cooling by sawtooth-wave adiabatic passage. Physical Review A, 98(2), Aug 2018.

[15] John P. Bartolotta, Jarrod T. Reilly, and Murray J. Holland. Speeding up particle slowing using shortcuts to adiabaticity. Phys. Rev. A, 102:043107, Oct 2020.

[16] Mark G. Bason, Matthieu Viteau, Nicola Malossi, Paul Huillery, Ennio Arimondo, Donatella Ciampini, Rosario Fazio, Vittorio Giovannetti, Riccardo Mannella, and Oliver Morsch. High-fidelity quantum driving. Nature Physics, 8(2):147–152, Feb 2012.

[17] G. Benivegna and A. Messina. Sub-radiant states of a spatially extended system of n two-level atoms. Journal of Modern Optics, 36(9):1205–1211, 1989.

[18] M. V. Berry. Quantal phase factors accompanying adiabatic changes. Proc. R. Soc. Lond. A, 392(1802):45–57, March 1984.

[19] M V Berry. Transitionless quantum driving. Journal of Physics A: Mathematical and Theoretical, 42(36):365303, 2009.

[20] Richard A. Beth. Mechanical detection and measurement of the angular momentum of light. Phys. Rev., 50:115–125, Jul 1936.

[21] Hendrick L. Bethlem, Giel Berden, Floris M. H. Crompvoets, Rienk T. Jongma, André J. A. van Roij, and Gerard Meijer. Electrostatic trapping of ammonia molecules. Nature, 406(6795):491–494, August 2000.

[22] Immanuel Bloch. Ultracold quantum gases in optical lattices. Nature Physics, 1(1):23–30, Oct 2005.

[23] Justin G. Bohnet, Zilong Chen, Joshua M. Weiner, Dominic Meiser, Murray J. Holland, and James K. Thompson. A steady-state superradiant laser with less than one intracavity photon. Nature, 484(7392):78–81, Apr 2012.

[24] R. Bonifacio, P. Schwendimann, and Fritz Haake. Quantum statistical theory of superradiance. i. Phys. Rev. A, 4:302–313, Jul 1971.

[25] E. Boukobza and D. J. Tannor. Entropy exchange and entanglement in the jaynes-cummings model. Phys. Rev. A, 71:063821, Jun 2005.

[26] Steve Campbell and Sebastian Deffner. Trade-off between speed and cost in shortcuts to adiabaticity. Phys. Rev. Lett., 118:100601, Mar 2017.

[27] T. Caneva, M. Murphy, T. Calarco, R. Fazio, S. Montangero, V. Giovannetti, and G. E. Santoro. Optimal control at the quantum speed limit. Phys. Rev. Lett., 103:240501, Dec 2009.

[28] M. T. Cashen and H. Metcalf. Bichromatic force on helium. Phys. Rev. A, 63:025406, Jan 2001.

[29] Thierry Chanelière, Daniel Comparat, and Hans Lignier. Phase-space-density limitation in laser cooling without spontaneous emission. Phys. Rev. A, 98:063432, Dec 2018.

[30] Xi Chen, I. Lizuain, A. Ruschhaupt, D. Guéry-Odelin, and J. G. Muga. Shortcut to adiabatic passage in two- and three-level atoms. Phys. Rev. Lett., 105:123003, Sep 2010.

[31] Xi Chen, A. Ruschhaupt, S. Schmidt, A. del Campo, D. Guéry-Odelin, and J. G. Muga. Fast optimal frictionless atom cooling in harmonic traps: Shortcut to adiabaticity. Phys. Rev. Lett., 104:063002, Feb 2010.

[32] Xi Chen, E. Torrontegui, and J. G. Muga. Lewis-riesenfeld invariants and transitionless quantum driving. Phys. Rev. A, 83:062116, Jun 2011.

[33] Ye-Hong Chen, Yan Xia, Qing-Qin Chen, and Jie Song. Shortcuts to adiabatic passage for multiparticles in distant cavities: applications to fast and noise-resistant quantum population transfer, entangled states' preparation and transition. Laser Physics Letters, 11(11):115201, sep 2014.

[34] S. Chervenkov, X. Wu, J. Bayerl, A. Rohlfes, T. Gantner, M. Zeppenfeld, and G. Rempe. Continuous centrifuge decelerator for polar molecules. Phys. Rev. Lett., 112:013001, Jan 2014.

[35] Steven Chu. Nobel lecture: The manipulation of neutral particles. Rev. Mod. Phys., 70:685–706, Jul 1998.

[36] J. I. Cirac. Interaction of a two-level atom with a cavity mode in the bad-cavity limit. Phys. Rev. A, 46:4354–4362, Oct 1992.

[37] Claude N. Cohen-Tannoudji. Nobel lecture: Manipulating atoms with photons. Rev. Mod. Phys., 70:707–719, Jul 1998.

[38] J Cohn, A Safavi-Naini, R J Lewis-Swan, J G Bohnet, M Gärttner, K A Gilmore, J E Jordan, A M Rey, J J Bollinger, and J K Freericks. Bang-bang shortcut to adiabaticity in the dicke model as realized in a penning trap experiment. New Journal of Physics, 20(5):055013, May 2018.

[39] Alejandra L Collopy, Matthew T Hummon, Mark Yeo, Bo Yan, and Jun Ye. Prospects for a narrow line MOT in YO. New Journal of Physics, 17(5):055008, may 2015.

[40] Christopher Corder, Brian Arnold, Xiang Hua, and Harold Metcalf. Laser cooling without spontaneous emission using the bichromatic force. J. Opt. Soc. Am. B, 32(5):B75–B83, May 2015.

[41] Ivan B. Coulamy, Alan C. Santos, Itay Hen, and Marcelo S. Sarandy. Energetic Cost of Superadiabatic Quantum Computation. Frontiers in ICT, 3, 2016.

[42] J Dalibard and C Cohen-Tannoudji. Atomic motion in laser light: connection between semi-classical and quantum descriptions. Journal of Physics B: Atomic and Molecular Physics, 18(8):1661–1683, apr 1985.

[43] M. A. de Ponte, P. M. Cônsoli, and M. H. Y. Moussa. Method for the construction of the lewis-riesenfeld time-dependent invariants and their eigenvalue equations. Phys. Rev. A, 98:032102, Sep 2018.

[44] Sebastian Deffner. Shortcuts to adiabaticity: suppression of pair production in driven dirac dynamics. New Journal of Physics, 18(1):012001, Dec 2015.

[45] Mustafa Demirplak and Stuart A. Rice. Adiabatic population transfer with control fields. The Journal of Physical Chemistry A, 107(46):9937–9945, 2003.

[46] R. H. Dicke. Coherence in spontaneous radiation processes. Phys. Rev., 93:99–110, Jan 1954.

[47] Yan-Xiong Du, Xian-Xian Yue, Zhen-Tao Liang, Jia-Zhen Li, Hui Yan, and Shi-Liang Zhu. Geometric atom interferometry with shortcuts to adiabaticity. Phys. Rev. A, 95:043608, Apr 2017.

[48] Albert Einstein. Zur Quantentheorie der Strahlung. Phys. Z., 18:121–128, 1917.

[49] Ethan R. Elliott, Markus C. Krutzik, Jason R. Williams, Robert J. Thompson, and David C. Aveline. NASA's Cold Atom Lab (CAL): system development and ground test status. npj Microgravity, 4(1):16, August 2018.

[50] Massimiliano Esposito, Katja Lindenberg, and Christian Van den Broeck. Entropy production as correlation between system and reservoir. New Journal of Physics, 12(1):013013, jan 2010.

[51] Alessandro Ferraro and Matteo G. A. Paris. Nonclassicality criteria from phase-space representations and information-theoretical constraints are maximally inequivalent. Phys. Rev. Lett., 108:260403, Jun 2012.

[52] Richard P. Feynman, Frank L. Vernon, and Robert W. Hellwarth. Geometrical representation of the schrödinger equation for solving maser problems. Journal of Applied Physics, 28(1):49–52, 1957.

[53] Z. Ficek and R. Tanaś. Entangled states and collective nonclassical effects in two-atom systems. Physics Reports, 372(5):369 – 443, 2002.

[54] Alexander Friedland. Evolution of the neutrino state inside the sun. Phys. Rev. D, 64:013008, May 2001.

[55] Xiao-Chun Gao, Jing-Bo Xu, and Tie-Zheng Qian. Geometric phase and the generalized invariant formulation. Phys. Rev. A, 44:7016–7021, Dec 1991.

[56] Michael Gegg, Alexander Carmele, Andreas Knorr, and Marten Richter. Superradiant to subradiant phase transition in the open system dicke model: dark state cascades. New Journal of Physics, 20(1):013006, jan 2018.

[57] Vittorio Giovannetti, Seth Lloyd, and Lorenzo Maccone. Advances in quantum metrology. Nature Photonics, 5(4):222–229, Apr 2011.

[58] Steffen J. Glaser, Ugo Boscain, Tommaso Calarco, Christiane P. Koch, Walter Köckenberger, Ronnie Kosloff, Ilya Kuprov, Burkhard Luy, Sophie Schirmer, Thomas Schulte-Herbrüggen, Dominique Sugny, and Frank K. Wilhelm. Training Schrödinger's cat: quantum optimal control. Strategic report on current status, visions and goals for research in Europe. European Physical Journal D, 69(12):279, December 2015.

[59] S. Glasgow, P. Meystre, M. Wilkens, and E. M. Wright. Theory of an atomic beam splitter based on velocity-tuned resonances. Phys. Rev. A, 43:2455–2463, Mar 1991.

[60] Roy J. Glauber. Coherent and incoherent states of the radiation field. Phys. Rev., 131:2766–2788, Sep 1963.

[61] Yiyang Gong, Maria Makarova, Selçuk Yerci, Rui Li, Martin J. Stevens, Burm Baek, Sae Woo Nam, Robert H. Hadfield, Sander N. Dorenbos, Val Zwiller, Jelena Vučković, and Luca Dal Negro. Linewidth narrowing and purcell enhancement in photonic crystal cavities on an er-doped silicon nitride platform. Opt. Express, 18(3):2601–2612, Feb 2010.

[62] G P Greve, B Wu, and J K Thompson. Laser cooling with adiabatic transfer on a raman transition. New Journal of Physics, 21(7):073045, jul 2019.

[63] M. Gross and S. Haroche. Superradiance: An essay on the theory of collective spontaneous emission. Physics Reports, 93(5):301 – 396, 1982.

[64] D. Guéry-Odelin, A. Ruschhaupt, A. Kiely, E. Torrontegui, S. Martínez-Garaot, and J. G. Muga. Shortcuts to adiabaticity: Concepts, methods, and applications. Rev. Mod. Phys., 91:045001, Oct 2019.

[65] Utkan Güngördü, Yidun Wan, Mohammad Ali Fasihi, and Mikio Nakahara. Dynamical invariants for quantum control of four-level systems. Phys. Rev. A, 86:062312, Dec 2012.

[66] Boerge Hemmerling, Eunmi Chae, Aakash Ravi, Loic Anderegg, Garrett K Drayna, Nicholas R Hutzler, Alejandra L Collopy, Jun Ye, Wolfgang Ketterle, and John M Doyle. Laser slowing of CaF molecules to near the capture velocity of a molecular MOT. Journal of Physics B: Atomic, Molecular and Optical Physics, 49(17):174001, aug 2016.

[67] S. D. Hogan, A. W. Wiederkehr, H. Schmutz, and F. Merkt. Magnetic trapping of hydrogen after multistage zeeman deceleration. Phys. Rev. Lett., 101:143001, Sep 2008.

[68] M. J. Holland and K. Burnett. Interferometric detection of optical phase shifts at the heisenberg limit. Phys. Rev. Lett., 71:1355–1358, Aug 1993.

[69] Gerald Holton and Yehuda Elkana, editors. Albert Einstein, Historical and Cultural Perspectives: The Centennial Symposium in Jerusalem. Princeton University Press, 1982.

[70] Lev B. Ioffe, Vadim B. Geshkenbein, Mikhail V. Feigel'man, Alban L. Fauchère, and Gianni Blatter. Environmentally decoupled sds -wave josephson junctions for quantum computing. Nature, 398(6729):679–681, Apr 1999.

[71] E. T. Jaynes and F. W. Cummings. Comparison of quantum and semiclassical radiation theories with application to the beam maser. Proceedings of the IEEE, 51(1):89–109, 1963.

[72] Wolfgang Ketterle. Nobel lecture: When atoms behave as waves: Bose-einstein condensation and the atom laser. Rev. Mod. Phys., 74:1131–1151, Nov 2002.

[73] K. Kim, M.-S. Chang, S. Korenblit, R. Islam, E. E. Edwards, J. K. Freericks, G.-D. Lin, L.-M. Duan, and C. Monroe. Quantum simulation of frustrated ising spins with trapped ions. Nature, 465(7298):590–593, Jun 2010.

[74] S.P Kim, A.E Santana, and F.C Khanna. Generalized invariants and quantum evolution of open fermionic systems. Physics Letters A, 272(1):46 – 52, 2000.

[75] H. J. Kimble. Strong interactions of single atoms and photons in cavity QED. Physica Scripta, T76(1):127, 1998.

[76] E. Korsunsky. Laser cooling during velocity-selective adiabatic population transfer. Phys. Rev. A, 54:R1773–R1776, Sep 1996.

[77] Sebastian Krämer, David Plankensteiner, Laurin Ostermann, and Helmut Ritsch. Quantumoptics.jl: A julia framework for simulating open quantum systems. Computer Physics Communications, 227:109 – 116, 2018.

[78] Y.-Z. Lai, J.-Q. Liang, H. J. W. Müller-Kirsten, and J.-G. Zhou. Time-dependent quantum systems and the invariant hermitian operator. Phys. Rev. A, 53:3691–3693, May 1996.

[79] R. H. Lehmberg. Radiation from an n-atom system. i. general formalism. Phys. Rev. A, 2:883–888, Sep 1970.

[80] H. R. Lewis and W. B. Riesenfeld. An exact quantum theory of the time-dependent harmonic oscillator and of a charged particle in a time-dependent electromagnetic field. Journal of Mathematical Physics, 10(8):1458–1473, 1969.

[81] Yi-Chao Li and Xi Chen. Shortcut to adiabatic population transfer in quantum three-level systems: Effective two-level problems and feasible counterdiabatic driving. Phys. Rev. A, 94:063411, Dec 2016.

[82] G. Lindblad. On the generators of quantum dynamical semigroups. Communications in Mathematical Physics, 48(2):119–130, 1976.

[83] T. Lu, X. Miao, and H. Metcalf. Nonadiabatic transitions in finite-time adiabatic rapid passage. Phys. Rev. A, 75:063422, Jun 2007.

[84] William Lunden, Li Du, Michael Cantara, Pierre Barral, Alan O. Jamison, and Wolfgang Ketterle. Enhancing the capture velocity of a Dy magneto-optical trap with two-stage slowing. arXiv e-prints, page arXiv:1908.10433, Aug 2019.

[85] S. Martínez-Garaot, A. Ruschhaupt, J. Gillet, Th. Busch, and J. G. Muga. Fast quasiadiabatic dynamics. Phys. Rev. A, 92:043406, Oct 2015.

[86] S. Martínez-Garaot, E. Torrontegui, Xi Chen, and J. G. Muga. Shortcuts to adiabaticity in three-level systems using lie transforms. Phys. Rev. A, 89:053408, May 2014.

[87] Shumpei Masuda and Katsuhiro Nakamura. Fast-forward problem in quantum mechanics. Phys. Rev. A, 78:062108, Dec 2008.

[88] Shumpei Masuda and Katsuhiro Nakamura. Fast-forward of adiabatic dynamics in quantum mechanics. Proceedings of the Royal Society A: Mathematical, Physical and Engineering Sciences, 466(2116):1135–1154, 2010.

[89] Shumpei Masuda and Stuart A. Rice. Fast-forward assisted stirap. The Journal of Physical Chemistry A, 119(14):3479–3487, 2015. PMID: 25775133.

[90] D. Meiser and M. J. Holland. Intensity fluctuations in steady-state superradiance. Phys. Rev. A, 81:063827, Jun 2010.

[91] D. Meiser and M. J. Holland. Steady-state superradiance with alkaline-earth-metal atoms. Phys. Rev. A, 81:033847, Mar 2010.

[92] D. Meiser, Jun Ye, D. R. Carlson, and M. J. Holland. Prospects for a millihertz-linewidth laser. Phys. Rev. Lett., 102:163601, Apr 2009.

[93] A. Messiah. Quantum Mechanics. Number v. 2 in Dover books on physics. Dover Publications, 1999.

[94] Harold Metcalf. Entropy exchange in laser cooling. Phys. Rev. A, 77:061401, Jun 2008.

[95] Harold Metcalf. Colloquium: Strong optical forces on atoms in multifrequency light. Rev. Mod. Phys., 89:041001, Oct 2017.

[96] Harold J. Metcalf and Peter van der. Straten. Laser cooling and trapping. Springer, 2002.

[97] Robert Meyers. Encyclopedia of Physical Science and Technology. Academic Press, 3 edition, 2001.

[98] Pierre Meystre and Murray Sargent. Elements of Quantum Optics. Springer, 2007.

[99] Jian-Guo Miao, Chun-Wang Wu, Wei Wu, and Ping-Xing Chen. Entropy exchange and thermodynamic properties of the single ion cooling process. Entropy, 21(7):650, Jul 2019.

[100] X. Miao, E. Wertz, M. G. Cohen, and H. Metcalf. Strong optical forces from adiabatic rapid passage. Phys. Rev. A, 75:011402, Jan 2007.

[101] V.g. Minogin and O.t. Serimaa. Resonant light pressure forces in a strong standing laser wave. Optics Communications, 30(3):373–379, 1979.

[102] Klaus Mølmer, Yvan Castin, and Jean Dalibard. Monte carlo wave-function method in quantum optics. J. Opt. Soc. Am. B, 10(3):524–538, Mar 1993.

[103] Henrik Lund Mortensen, Jens Jakob W. H. Sørensen, Klaus Mølmer, and Jacob Friis Sherson. Fast state transfer in a $\{upLambda\}$-system: a shortcut-to-adiabaticity approach to robust and resource optimized control. New Journal of Physics, 20(2):025009, feb 2018.

[104] Juan A. Muniz, Matthew A. Norcia, Julia R. K. Cline, and James K. Thompson. A Robust Narrow-Line Magneto-Optical Trap using Adiabatic Transfer. arXiv e-prints, page arXiv:1806.00838, Jun 2018.

[105] Edvardas Narevicius, Adam Libson, Christian G. Parthey, Isaac Chavez, Julia Narevicius, Uzi Even, and Mark G. Raizen. Stopping supersonic beams with a series of pulsed electromagnetic coils: An atomic coilgun. Phys. Rev. Lett., 100:093003, Mar 2008.

[106] S. Nicolosi, A. Napoli, and A. Messina. Loss induced collective subradiant dicke behaviour in a multiatom sample. The European Physical Journal D - Atomic, Molecular, Optical and Plasma Physics, 33(1):113–121, Apr 2005.

[107] Michael A. Nielsen and Isaac L. Chuang. Quantum Computation and Quantum Information: 10th Anniversary Edition. Cambridge University Press, USA, 10th edition, 2011.

[108] Matthew A Norcia, Julia R K Cline, John P Bartolotta, Murray J Holland, and James K Thompson. Narrow-line laser cooling by adiabatic transfer. New Journal of Physics, 20(2):023021, Feb 2018.

[109] Matthew A. Norcia and James K. Thompson. Cold-strontium laser in the superradiant crossover regime. Phys. Rev. X, 6:011025, Mar 2016.

[110] Ian Norris. Laser cooling and trapping of neutral calcium atoms. PhD thesis, University of Strathclyde, 2009.

[111] Laurin Ostermann, Helmut Ritsch, and Claudiu Genes. Protected state enhanced quantum metrology with interacting two-level ensembles. Phys. Rev. Lett., 111:123601, Sep 2013.

[112] Francesco Petiziol, Benjamin Dive, Florian Mintert, and Sandro Wimberger. Fast adiabatic evolution by oscillating initial hamiltonians. Phys. Rev. A, 98:043436, Oct 2018.

[113] M Petzold, P Kaebert, P Gersema, M Siercke, and S Ospelkaus. A zeeman slower for diatomic molecules. New Journal of Physics, 20(4):042001, apr 2018.

[114] William D. Phillips. Nobel lecture: Laser cooling and trapping of neutral atoms. Rev. Mod. Phys., 70:721–741, Jul 1998.

[115] Krzysztof Ptaszyński and Massimiliano Esposito. Entropy production in open systems: The predominant role of intraenvironment correlations. Phys. Rev. Lett., 123:200603, Nov 2019.

[116] N. Ramsey and Oxford University Press. Molecular Beams. International series of monographs on physics. OUP Oxford, 1956.

[117] C. A. Regal, M. Greiner, and D. S. Jin. Observation of resonance condensation of fermionic atom pairs. Phys. Rev. Lett., 92:040403, Jan 2004.

[118] A Ruschhaupt, Xi Chen, D Alonso, and J G Muga. Optimally robust shortcuts to population inversion in two-level quantum systems. New Journal of Physics, 14(9):093040, sep 2012.

[119] A. Ruschhaupt and J.G. Muga. Shortcuts to adiabaticity in two-level systems: control and optimization. Journal of Modern Optics, 61(10):828–832, 2014.

[120] M. S. Safronova, D. Budker, D. DeMille, Derek F. Jackson Kimball, A. Derevianko, and Charles W. Clark. Search for new physics with atoms and molecules. Rev. Mod. Phys., 90:025008, Jun 2018.

[121] J.J. Sakurai and J. Napolitano. Modern Quantum Mechanics. Cambridge University Press, 2017.

[122] R. Sala, S. Brouard, and J. G. Muga. Wigner trajectories and liouville's theorem. The Journal of Chemical Physics, 99(4):2708–2714, 1993.

[123] M. S. Sarandy, E. I. Duzzioni, and R. M. Serra. Quantum computation in continuous time using dynamic invariants. Physics Letters A, 375(38):3343–3347, Sep 2011.

[124] Denise Sawicki and J.H. Eberly. Perfect following in the diabatic limit. Opt. Express, 4(7):217–222, Mar 1999.

[125] Dries Sels. Stochastic gradient ascent outperforms gamers in the quantum moves game. Phys. Rev. A, 97:040302, Apr 2018.

[126] Nathan Shammah, Shahnawaz Ahmed, Neill Lambert, Simone De Liberato, and Franco Nori. Open quantum systems with local and collective incoherent processes: Efficient numerical simulations using permutational invariance. Phys. Rev. A, 98:063815, Dec 2018.

[127] S. Snigirev, A. J. Park, A. Heinz, I. Bloch, and S. Blatt. Fast and dense magneto-optical traps for strontium. Phys. Rev. A, 99:063421, Jun 2019.

[128] J. Söding, R. Grimm, Yu. B. Ovchinnikov, Ph. Bouyer, and Ch. Salomon. Short-distance atomic beam deceleration with a stimulated light force. Phys. Rev. Lett., 78:1420–1423, Feb 1997.

[129] Daniel Stack, John Elgin, Petr M. Anisimov, and Harold Metcalf. Numerical studies of optical forces from adiabatic rapid passage. Phys. Rev. A, 84:013420, Jul 2011.

[130] Daniel A. Steck. Quantum and atom optics, 2007.

[131] Dionisis Stefanatos, Justin Ruths, and Jr-Shin Li. Frictionless atom cooling in harmonic traps: A time-optimal approach. Phys. Rev. A, 82:063422, Dec 2010.

[132] Simon Stellmer, Benjamin Pasquiou, Rudolf Grimm, and Florian Schreck. Laser cooling to quantum degeneracy. Phys. Rev. Lett., 110:263003, Jun 2013.

[133] C. R. Stroud, J. H. Eberly, W. L. Lama, and L. Mandel. Superradiant effects in systems of two-level atoms. Phys. Rev. A, 5:1094–1104, Mar 1972.

[134] Benjamin K. Stuhl, Matthew T. Hummon, Mark Yeo, Goulven Quéméner, John L. Bohn, and Jun Ye. Evaporative cooling of the dipolar hydroxyl radical. Nature, 492(7429):396–400, December 2012.

[135] Kazutaka Takahashi. Hamiltonian engineering for adiabatic quantum computation: Lessons from shortcuts to adiabaticity. Journal of the Physical Society of Japan, 88(6):061002, 2019.

[136] Masao Takamoto, Feng-Lei Hong, Ryoichi Higashi, and Hidetoshi Katori. An optical lattice clock. Nature, 435(7040):321–324, May 2005.

[137] M. G. Tarallo, G. Z. Iwata, and T. Zelevinsky. Bah molecular spectroscopy with relevance to laser cooling. Phys. Rev. A, 93:032509, Mar 2016.

[138] Vasily V. Temnov and Ulrike Woggon. Photon statistics in the cooperative spontaneous emission. Opt. Express, 17(7):5774–5782, Mar 2009.

[139] D. Tieri. Open Quantum Systems with Applications to Precision Measurements. PhD thesis, University of Colorado Boulder, Boulder, CO, 12-2015 2015.

[140] D. A. Tieri, Minghui Xu, D. Meiser, J. Cooper, and M. J. Holland. Theory of the crossover from lasing to steady state superradiance, 2017.

[141] E. Torrontegui, S. Martínez-Garaot, and J. G. Muga. Hamiltonian engineering via invariants and dynamical algebra. Phys. Rev. A, 89:043408, Apr 2014.

[142] E. Torrontegui, S. Martínez-Garaot, A. Ruschhaupt, and J. G. Muga. Shortcuts to adiabaticity: Fast-forward approach. Phys. Rev. A, 86:013601, Jul 2012.

[143] Géza Tóth, Christian Knapp, Otfried Gühne, and Hans J. Briegel. Optimal spin squeezing inequalities detect bound entanglement in spin models. Phys. Rev. Lett., 99:250405, Dec 2007.

[144] S Truppe, H J Williams, N J Fitch, M Hambach, T E Wall, E A Hinds, B E Sauer, and M R Tarbutt. An intense, cold, velocity-controlled molecular beam by frequency-chirped laser slowing. New Journal of Physics, 19(2):022001, Feb 2017.

[145] Alban Urvoy, Zachary Vendeiro, Joshua Ramette, Albert Adiyatullin, and Vladan Vuletić. Direct laser cooling to bose-einstein condensation in a dipole trap. Phys. Rev. Lett., 122:203202, May 2019.

[146] Lorenza Viola and Seth Lloyd. Dynamical suppression of decoherence in two-state quantum systems. Phys. Rev. A, 58:2733–2744, Oct 1998.

[147] N. V. Vitanov. Transition times in the landau-zener model. Phys. Rev. A, 59:988–994, Feb 1999.

[148] V.S. Voitsekhovich, M.V. Danileiko, A.M Negriiko, V.I Romanenko, and L.P. Yatsenko. Stimulated light pressure on atoms in counterpropagating amplitude-modulated waves. JETP, 72:219–227, Feb 1991.

[149] R Wynands and S Weyers. Atomic fountain clocks. Metrologia, 42(3):S64–S79, jun 2005.

[150] Minghui Xu. Theory of Steady-State Superradiance. PhD thesis, University of Colorado Boulder, Boulder, CO, 04-2016 2016.

[151] Minghui Xu, D. A. Tieri, and M. J. Holland. Simulating open quantum systems by applying su(4) to quantum master equations. Phys. Rev. A, 87:062101, Jun 2013.

[152] Ryuta Yamamoto, Jun Kobayashi, Takuma Kuno, Kohei Kato, and Yoshiro Takahashi. An ytterbium quantum gas microscope with narrow-line laser cooling. New Journal of Physics, 18(2):023016, feb 2016.

[153] Clarence Zener. Non-adiabatic crossing of energy levels. Proceedings of the Royal Society of London. Series A, Containing Papers of a Mathematical and Physical Character, 137(833):696–702, 1932.

[154] Yuan Zhang, Yu-Xiang Zhang, and Klaus Mølmer. Monte-carlo simulations of superradiant lasing. New Journal of Physics, 20(11):112001, nov 2018.

Appendix A

Two-Level Hamiltonian Derivation

This appendix is dedicated to the derivation of the Hamiltonian of a two-level atom in a classical electric field Eq. (2.9). It follows a similar format as [130, Chapter 5].

A.1 Atom-Field Interaction

If we assume a monochromatic field, with angular frequency ω, to model a laser, we see that the elctric field operator can be written as

$$\hat{\boldsymbol{E}}(t) = \hat{\boldsymbol{\varepsilon}} E_0 \cos(\omega t)\,, \tag{A.1}$$

where $\hat{\boldsymbol{\varepsilon}}$ is the unit polarization vector of the field. Note we have made the diople approximation, which assumes the wavelength of the field is much longer than the particle's size so that we may neglect the spatial dependence of the field. This is appropriate for most optical transitions that are $\mathcal{O}(10^{-7}\text{m})$ while the inter-atomic distances are on the scale of ångströms ($\text{Å} = 10^{-10}\,\text{m}$). It is convenient to decompose the field into oppositely rotating components

$$\hat{\boldsymbol{E}}(t) = \hat{\boldsymbol{\varepsilon}} \frac{E_0}{2}\left(e^{-i\omega t} + e^{i\omega t}\right) = \hat{\boldsymbol{E}}^{(+)}(t) + \hat{\boldsymbol{E}}^{(-)}(t). \tag{A.2}$$

We then makes the two-level atom approximation where we consider ground $|g\rangle$ and excited state $|e\rangle$, and assume that transitions to all other levels are negligible. If the energy difference between the states is $\mathit{\Delta} E = E_e - E_g$, the de Broglie relation gives us the tranisition frequency $\mathit{\Delta} E = \hbar\omega_a$. With the definition of zero energy to be halfway between the states, the atomic free-evolution

Hamiltonian is

$$\hat{H}_A = \frac{\hbar\omega_a}{2}\left(|e\rangle\langle e| - |g\rangle\langle g|\right). \tag{A.3}$$

The atom-field interaction Hamiltonian, under the dipole approximation, is [98, Chapter 3]

$$\hat{H}_{\text{int}} = -\hat{\boldsymbol{d}} \cdot \hat{\boldsymbol{E}}, \tag{A.4}$$

where $\hat{\boldsymbol{d}}$ is the atomic dipole operator.

A.2 Dipole Operator in the Energy Basis

Let us consider an interaction with a single electron, such that the dipole operator can be written in terms of the electron's position $\hat{\boldsymbol{r}}$ and charge $q = -e$ as

$$\hat{\boldsymbol{d}} \equiv q\hat{\boldsymbol{r}} = -e\hat{\boldsymbol{r}}. \tag{A.5}$$

We then us a parity argument to get the dipole operator in a more convenient form.

We define the unitary parity operator as

$$\hat{\mathit{\Pi}}\hat{\boldsymbol{r}}\hat{\mathit{\Pi}}^{\dagger} = -\hat{\boldsymbol{r}}, \tag{A.6}$$

so that $\hat{\mathit{\Pi}}\hat{\boldsymbol{r}} = -\hat{\boldsymbol{r}}\hat{\mathit{\Pi}}$. We can thus write

$$\{\hat{\mathit{\Pi}}, \hat{\boldsymbol{r}}\} = 0 \rightarrow \langle a| \{\hat{\mathit{\Pi}}, \hat{\boldsymbol{r}}\} |b\rangle = 0. \tag{A.7}$$

Using the energy basis, we see

$$(\pi_a + \pi_b) \langle a| \hat{\boldsymbol{r}} |b\rangle = 0, \tag{A.8}$$

for $a, b \in \{g, e\}$ and parity eigenvalues π_a and π_b. Since the parity operation has the involution property[1] , these eigenvector must correspond to ±1 which corresponds to even and odd parity, respectively. This suggests that either $(\pi_a + \pi_b) = 0$ or $\langle a| \hat{\boldsymbol{r}} |b\rangle = 0$. For the diagonal elements, the latter must be true as the eigenvalues are equal:

$$\langle g| \hat{\boldsymbol{d}} |g\rangle = \langle e| \hat{\boldsymbol{d}} |e\rangle = 0. \tag{A.9}$$

---

[1] $\hat{\mathit{\Pi}} = \hat{\mathit{\Pi}}^{-1} \rightarrow \hat{\mathit{\Pi}}^2 = \hat{\mathbb{I}}$

However, this need not be the case for the off diagonal terms provided that the states have opposite parity and thus,

$$\langle g|\,\hat{\boldsymbol{d}}\,|e\rangle = \langle e|\,\hat{\boldsymbol{d}}\,|g\rangle^{*}\,. \tag{A.10}$$

This expresses that the dipole operator may couple the ground and excited states, but it does not produce any first-order energy shifts of the individual states. Applying the identity operator on both sides of $\hat{\boldsymbol{d}}$, we find

$$\hat{\boldsymbol{d}} = \langle g|\,\hat{\boldsymbol{d}}\,|e\rangle\,|g\rangle\langle e| + \langle e|\,\hat{\boldsymbol{d}}\,|g\rangle\,|e\rangle\langle g|\,. \tag{A.11}$$

Let us suppose, by choice of phase, that the dipole matrix elements are real, which allows us to write the dipole operator as

$$\hat{\boldsymbol{d}} = \langle g|\,\hat{\boldsymbol{d}}\,|e\rangle\,(|g\rangle\langle e| + |e\rangle\langle g|)\,, \tag{A.12}$$

and thus,

$$\hat{H}_{\text{int}} = \langle g|\,\hat{\boldsymbol{d}}\,|e\rangle\cdot\hat{\boldsymbol{E}}\,(|g\rangle\langle e| + |e\rangle\langle g|) = \langle g|\,\hat{\boldsymbol{d}}\,|e\rangle\cdot\hat{\boldsymbol{E}}\left(\hat{\sigma}^{-}+\hat{\sigma}^{+}\right), \tag{A.13}$$

with lowering operator $\hat{\sigma}^{-} = |g\rangle\langle e|$.

A.3 Rotating-Wave Approximation

We now can decompose the dipole operator into positive- and negative-rotating parts as the expectation value of $\hat{\sigma}^{-}$ has time dependence of $e^{-i\omega_a t}$ [130, Chapter 5]. We find

$$\hat{\boldsymbol{d}} = \langle g|\,\hat{\boldsymbol{d}}\,|e\rangle\left(\hat{\sigma}^{-}+\hat{\sigma}^{+}\right) = \hat{\boldsymbol{d}}^{(+)} + \hat{\boldsymbol{d}}^{(-)}, \tag{A.14}$$

with $\hat{\boldsymbol{d}}^{(+)} \sim \hat{\sigma}^{-}$ and $\hat{\boldsymbol{d}}^{(-)} \sim \hat{\sigma}^{+}$. Therefore, the atom-field interaction Hamiltonian becomes

$$\begin{aligned}\hat{H}_{\text{int}} &= -\left(\hat{\boldsymbol{d}}^{(+)} + \hat{\boldsymbol{d}}^{(-)}\right)\cdot\left(\hat{\boldsymbol{E}}^{(+)} + \hat{\boldsymbol{E}}^{(-)}\right)\\ &= -\hat{\boldsymbol{d}}^{(+)}\cdot\hat{\boldsymbol{E}}^{(+)} - \hat{\boldsymbol{d}}^{(-)}\cdot\hat{\boldsymbol{E}}^{(-)} - \hat{\boldsymbol{d}}^{(+)}\cdot\hat{\boldsymbol{E}}^{(-)} - \hat{\boldsymbol{d}}^{(-)}\cdot\hat{\boldsymbol{E}}^{(+)} \qquad (A.15)\\ &= -\left[e^{-i(\omega+\omega_a)t} + e^{i(\omega+\omega_a)t} + e^{-i(\omega-\omega_a)t} + e^{i(\omega-\omega_a)t}\right].\end{aligned}$$

Here, we find that the leading two terms oscillate rapidly, while the cross terms evolve slowly. This prompts us to make the rotating-wave approximation (RWA):

$$|\omega-\omega_a| \ll \omega+\omega_a. \tag{A.16}$$

This allows us to replace the fast oscillating terms by their average value. We are thus able to focus on the slow dynamics of the system:

$$\hat{H}_{\text{int}} = -\hat{\boldsymbol{d}}^{(+)} \cdot \hat{\boldsymbol{E}}^{(-)} - \hat{\boldsymbol{d}}^{(-)} \cdot \hat{\boldsymbol{E}}^{(+)}. \tag{A.17}$$

As pointed out in [130], the RWA approximation and the two-level approximation are at the same level of accuracy as they both amount to disregarding interaction that are far off resonance. If the detuning is large enough that the counter-rotating terms are not negligible, than the coupling to other energy levels is not negligible either.

A.4 Rabi Frequency

We can now write Eq. (A.17) out explicitly,

$$\hat{H}_{\text{int}} = -\langle g|\, \hat{\boldsymbol{\varepsilon}} \cdot \hat{\boldsymbol{d}}\, |e\rangle \left(E_0^{(-)} \hat{\sigma}^- e^{i\omega t} + E_0^{(+)} \hat{\sigma}^+ e^{-i\omega t} \right), \tag{A.18}$$

which becomes

$$\hat{H}_{\text{int}} = \frac{\hbar \varOmega}{2} \left(\hat{\sigma}^- e^{i\omega t} + \hat{\sigma}^+ e^{-i\omega t} \right). \tag{A.19}$$

Here, we have defined the Rabi frequency as

$$\varOmega = -\frac{2 \langle g|\, \hat{\boldsymbol{\varepsilon}} \cdot \hat{\boldsymbol{d}}\, |e\rangle\, E_0^{(+)}}{\hbar} = -\frac{\langle g|\, \hat{\boldsymbol{\varepsilon}} \cdot \hat{\boldsymbol{d}}\, |e\rangle\, E_0}{\hbar}, \tag{A.20}$$

where we have assumed $E_0^{(+)}$ is real. In the case of a linearly polarized field[2] , this simplifies to

$$\varOmega = -\frac{\langle g|\, d_z \,|e\rangle\, E_0}{\hbar}. \tag{A.21}$$

We see that the Rabi frequency characterizes the strength of the atom-field coupling.

A.5 Time-Dependent Detuning

We now generalize to a chirped field in which the frequency ω is now the rate at which the phase accumulates, $e^{-i\eta(t)}$ with $\omega = \frac{d\eta(t)}{dt}$. This leads to the replacements

$$e^{i\omega t} \to \exp\left[i \int_{t_0}^{t} \omega(t')dt' \right], \qquad e^{-i\omega t} \to \exp\left[-i \int_{t_0}^{t} \omega(t')dt' \right], \tag{A.22}$$

---

[2] We make the arbitrary choice of $\hat{\boldsymbol{\varepsilon}} = \hat{z}$.

where $\omega(t')$ is the laser's instantaneous frequency. Further assuming a time-dependent Rabi frequency gives the final, desired form of the Hamiltonian [Eq. (2.9)]:

$$\hat{H} = \hat{H}_A + \hat{H}_{\text{int}} = \frac{\hbar\omega_a}{2}\left(|e\rangle\langle e| - |g\rangle\langle g|\right) + \frac{\hbar\Omega(t)}{2}\left(|g\rangle\langle e|\, e^{i\int_{t_0}^{t}\omega(t')dt'} + \text{H.c.}\right). \tag{A.23}$$

Appendix B

Interaction Picture

This appendix provides some basic background of the quantum interaction picture. I then provide two specific examples that occur commonly throughout the thesis. I refer the reader to [121, Chapter 5, §5] for a more detailed discussion on the interaction picture.

B.1 Background

We consider a time-dependent Hamiltonian, which we can split into two separate part,

$$\hat{H}_{\text{tot}} = \hat{H}_0 + \hat{H} \tag{B.1}$$

Let us denote a state vector in the *Schrödinger picture* as $|\rangle_S$. We now define a state vector $|\rangle_I$ in the so-called *interaction picture*, or *Dirac picture*, as

$$|\psi(t)\rangle_I \equiv e^{\frac{i\hat{H}_0 t}{\hbar}} |\psi(t)\rangle_S \,, \tag{B.2}$$

so that an observable in the interaction picture $\tilde{\hat{A}}$ is given by

$$\tilde{\hat{A}} \equiv e^{\frac{i\hat{H}_0 t}{\hbar}} \hat{A} e^{-\frac{i\hat{H}_0 t}{\hbar}} , \tag{B.3}$$

where $\hat{A}$ is an observable in the Schrödinger picture. Note that this is different than the third picture in quantum mechanics, the *Heisenberg picture*, where one has time-independent state ket and time-dependent observable defined by

$$|\psi\rangle_H \equiv e^{\frac{i\hat{H}_{\text{tot}} t}{\hbar}} |\psi(t)\rangle_S \,, \qquad \hat{A}_H \equiv e^{\frac{i\hat{H}_{\text{tot}} t}{\hbar}} \hat{A} e^{-\frac{i\hat{H}_{\text{tot}} t}{\hbar}} , \tag{B.4}$$

	Schrödinger picture	Interaction picture	Heisenberg picture
State ket	Evolution determined by $\hat{H}_{\text{tot}}$	Evolution determined by $\tilde{\hat{H}}$	No change
Observable	No change	Evolution determined by $\hat{H}_0$	Evolution determined by $\hat{H}_{\text{tot}}$

Table B.1: Source: Ref. [121]. Table of the three main pictures used to determine the time evolution of a quantum system.

that satisfies the Heisenberg equation of motion:

$$\frac{d\hat{A}_H}{dt} = \frac{1}{i\hbar}\left[\hat{A}_H, \hat{H}_{\text{tot}}\right]. \tag{B.5}$$

Using Eqs. (B.2) and (B.3) along with the Schödinger equation Eq. (2.2), one finds the equations of motion in the interaction picture [121, Chapter 5, §5]:

$$\begin{aligned} i\hbar\partial_t \left|\psi(t)\right\rangle_I &= i\hbar\frac{\partial}{\partial t}\left(e^{\frac{i\hat{H}_0 t}{\hbar}}\left|\psi(t)\right\rangle_S\right) \\ &= -\hat{H}_0 e^{\frac{i\hat{H}_0 t}{\hbar}}\left|\psi(t)\right\rangle_S + e^{\frac{i\hat{H}_0 t}{\hbar}}\left(\hat{H}_0 + \hat{H}\right)\left|\psi(t)\right\rangle_S \\ &= e^{\frac{i\hat{H}_0 t}{\hbar}}\hat{H}e^{\frac{-i\hat{H}_0 t}{\hbar}}e^{\frac{i\hat{H}_0 t}{\hbar}}\left|\psi(t)\right\rangle_S \\ &= \tilde{\hat{H}}\left|\psi(t)\right\rangle_I, \end{aligned} \tag{B.6}$$

which is a Schrödinger-like equation. Furthermore, using Eq. (B.3) it can be shown that the Heisenberg-like equation,

$$\frac{d\tilde{\hat{A}}}{dt} = \frac{1}{i\hbar}\left[\tilde{\hat{A}}, \hat{H}_0\right], \tag{B.7}$$

is satisfied with the evolution determined by $\hat{H}_0$. The interaction picture is therefore a sort of intermediate picture that connects the Schrödinger and Heisenberg pictures, as displayed in Table B.1.

B.2 Laser Frame

Let us now consider an illustrative example. We begin with Eq. (2.9),

$$\hat{H}_{\text{tot}} = \frac{\hbar\omega_a}{2}\left(|e\rangle\langle e| - |g\rangle\langle g|\right) + \frac{\hbar\Omega(t)}{2}\left(\hat{\sigma}^- e^{i\int_{t_0}^{t}\omega(t')dt'} + \text{H.c.}\right), \tag{B.8}$$

and move into the frame rotating with the laser frequency,

$$\hat{H}_0 = \frac{\hbar\omega(t)}{2}\left(|e\rangle\langle e| - |g\rangle\langle g|\right). \tag{B.9}$$

Here, we write

$$\begin{aligned}\tilde{\hat{H}} &= e^{\frac{i\hat{H}_0 t}{\hbar}}\left(\hat{H}_{\text{tot}} - \hat{H}_0\right)e^{\frac{-i\hat{H}_0 t}{\hbar}} \\ &= -\frac{\hbar\delta(t)}{2}\left(|e\rangle\langle e| - |g\rangle\langle g|\right) + \frac{\hbar\mathit{\Omega}(t)}{2}\left(e^{\frac{i\hat{H}_0 t}{\hbar}}\hat{\sigma}^- e^{\frac{-i\hat{H}_0 t}{\hbar}} e^{i\int_{t_0}^{t}\omega(t')dt'} + \text{H.c.}\right),\end{aligned} \tag{B.10}$$

where we have defined the detuning $\delta(t) = \omega(t) - \omega_a$.

We now calculate the lowering operator transformed into the laser frame,

$$\tilde{\hat{\sigma}}^- = e^{\frac{i\hat{H}_0 t}{\hbar}}\hat{\sigma}^- e^{\frac{-i\hat{H}_0 t}{\hbar}}. \tag{B.11}$$

Taking a time derivative, denoted by a dot, we see

$$\dot{\tilde{\hat{\sigma}}}^- = \frac{i\hat{H}_0}{\hbar}\tilde{\hat{\sigma}}^- + e^{\frac{i\hat{H}_0 t}{\hbar}}\hat{\sigma}^-\left(-\frac{i\hat{H}_0}{\hbar}\right)e^{\frac{-i\hat{H}_0 t}{\hbar}}, \tag{B.12}$$

which we can, noting that $\hat{H}_0$ commutes with itself, write as

$$\dot{\tilde{\hat{\sigma}}}^- = \frac{i}{\hbar}\left(\hat{H}_0\tilde{\hat{\sigma}}^- - \tilde{\hat{\sigma}}^-\hat{H}_0\right) = \frac{i}{\hbar}\left[\hat{H}_0, \tilde{\hat{\sigma}}^-\right] = \frac{i}{\hbar}\left(e^{\frac{i\hat{H}_0 t}{\hbar}}\left[\hat{H}_0, \hat{\sigma}^-\right]e^{\frac{-i\hat{H}_0 t}{\hbar}}\right) \tag{B.13}$$

Plugging in for $\hat{H}_0$ and $\hat{\sigma}^-$, we find

$$\begin{aligned}\dot{\tilde{\hat{\sigma}}}^- &= \frac{i\omega(t)}{2}e^{\frac{i\hat{H}_0 t}{\hbar}}\left(\left[|e\rangle\langle e|, |g\rangle\langle e|\right] - \left[|g\rangle\langle g|, |g\rangle\langle e|\right]\right)e^{\frac{-i\hat{H}_0 t}{\hbar}} \\ &= \frac{i\omega(t)}{2}e^{\frac{i\hat{H}_0 t}{\hbar}}\left(-2\,|g\rangle\langle e|\right)e^{\frac{-i\hat{H}_0 t}{\hbar}} = -i\omega(t)\tilde{\hat{\sigma}}^-.\end{aligned} \tag{B.14}$$

This differential equation is solved by separation of variables,

$$\frac{d\tilde{\hat{\sigma}}^-}{\tilde{\hat{\sigma}}^-} = -i\omega(t)dt \longrightarrow \int\frac{d\tilde{\hat{\sigma}}^-}{\tilde{\hat{\sigma}}^-} = \int_{t_0}^{t} -i\omega(t)dt', \tag{B.15}$$

which yields

$$\ln\tilde{\hat{\sigma}}^- = \int_{t_0}^{t} -i\omega(t')dt' \longrightarrow \tilde{\hat{\sigma}} = \hat{\sigma}^- e^{-i\int_{t_0}^{t}\omega(t')dt'}, \tag{B.16}$$

where we have used $\tilde{\hat{\sigma}}^-(t=0) = \hat{\sigma}^-$. The same process gives its Hermitian conjugate,

$$\tilde{\hat{\sigma}}^+ = \hat{\sigma}^+ e^{i\int_{t_0}^{t}\omega(t')dt'}. \tag{B.17}$$

We plug these back into Eq. (B.10) and see that the laser phases now cancel out and thus, we arrive at Eq. (2.11):

$$\tilde{\hat{H}} = \frac{\hbar\delta(t)}{2}\left(|g\rangle\langle g| - |e\rangle\langle e|\right) + \frac{\hbar\mathit{\Omega}(t)}{2}\left(\hat{\sigma}^- + \hat{\sigma}^+\right), \tag{B.18}$$

B.3 Particle Frame

Here, we present a general approach to move into a particle's frame, i.e.,

$$\hat{H}_0 = \frac{\hat{p}^2}{2m}. \tag{B.19}$$

We consider how the momentum-shift operator transforms into this frame:

$$\left(e^{ik\hat{z}}\right)_I = e^{\frac{i\hat{H}_0 t}{\hbar}} e^{ik\hat{z}} e^{\frac{-i\hat{H}_0 t}{\hbar}}, \tag{B.20}$$

which we expand via Taylor series[1] as

$$\left(e^{ik\hat{z}}\right)_I = e^{\frac{i\hat{H}_0 t}{\hbar}} \left[\sum_{n=0}^{\infty} \frac{(ik\hat{z})^n}{n!}\right] e^{\frac{-i\hat{H}_0 t}{\hbar}} = \sum_{n=0}^{\infty} \frac{(ik)^n}{n!} e^{\frac{i\hat{H}_0 t}{\hbar}} \hat{z}^n e^{\frac{-i\hat{H}_0 t}{\hbar}}, \tag{B.21}$$

and noting $\exp\left[i\hat{H}_0 t/\hbar\right] \exp\left[-i\hat{H}_0 t/\hbar\right] = \hat{\mathbb{I}}$, we can write

$$\left(e^{ik\hat{z}}\right)_I = \sum_{n=0}^{\infty} \frac{(ik)^n}{n!} \underbrace{e^{\frac{i\hat{H}_0 t}{\hbar}} \hat{z} e^{\frac{-i\hat{H}_0 t}{\hbar}} e^{\frac{i\hat{H}_0 t}{\hbar}} \hat{z} e^{\frac{-i\hat{H}_0 t}{\hbar}} \ldots e^{\frac{i\hat{H}_0 t}{\hbar}} \hat{z} e^{\frac{-i\hat{H}_0 t}{\hbar}}}_{n \text{ terms}} = \sum_{n=0}^{\infty} \frac{(ik)^n}{n!} \left(e^{\frac{i\hat{H}_0 t}{\hbar}} \hat{z} e^{\frac{-i\hat{H}_0 t}{\hbar}}\right)^n. \tag{B.22}$$

We can expand the term in the parenthesis using the Baker-Hausdorff lemma (see [121, Chapter 2, §3]):

$$\begin{aligned} e^{i\hat{B}\lambda} \hat{A} e^{-i\hat{B}\lambda} =& \hat{A} + i\lambda \left[\hat{B}, \hat{A}\right] + \frac{(i\lambda)^2}{2!} \left[\hat{B}, \left[\hat{B}, \hat{A}\right]\right] \\ & + \cdots + \frac{(i\lambda)^n}{n!} \left[\hat{B}, \left[\hat{B}, \left[\hat{B}, \ldots \left[\hat{B}, \hat{A}\right]\right]\right] \ldots\right] + \cdots , \end{aligned} \tag{B.23}$$

with real parameter λ, so that

$$e^{\frac{i\hat{H}_0 t}{\hbar}} \hat{z} e^{\frac{-i\hat{H}_0 t}{\hbar}} = \hat{z} + \frac{it}{\hbar} \left[\hat{H}_0, \hat{z}\right] - \frac{t^2}{2\hbar^2} \left[\hat{H}_0, \left[\hat{H}_0, \hat{z}\right]\right] + \cdots . \tag{B.24}$$

Focusing on the commutator, we expand

$$\left[\hat{H}_0, \hat{z}\right] = -\frac{1}{2m} \left[\hat{z}, \hat{p}^2\right] = -\frac{i\hbar}{2m} \frac{\partial}{\partial \hat{p}} \left(\hat{p}^2\right) = -\frac{i\hbar \hat{p}}{m}, \tag{B.25}$$

where we have used [121, Chapter 2, §2]

$$\left[\hat{x}_i, f(\hat{p}_i)\right] = i\hbar \frac{\partial f}{\partial \hat{p}_i}. \tag{B.26}$$

---

[1] $e^x = \sum_{n=0}^{\infty} x^n/n!$

We see from Eq. (B.25) that

$$\left[\hat{H}_0, \left[\hat{H}_0, \hat{z}\right]\right] = 0, \tag{B.27}$$

and therefore

$$e^{\frac{i\hat{H}_0 t}{\hbar}} \hat{z} e^{\frac{-i\hat{H}_0 t}{\hbar}} = \hat{z} + \frac{\hat{p}t}{m}. \tag{B.28}$$

Plugging this into Eq. (B.24), we find the momentum-shift operator in the atomic frame:

$$\left(e^{ik\hat{z}}\right)_I = \sum_{n=0}^{\infty} \frac{(ik)^n}{n!} \left(\hat{z} + \frac{\hat{p}t}{m}\right)^n = \exp\left[ik\left(\hat{z} + \frac{\hat{p}t}{m}\right)\right]. \tag{B.29}$$

Appendix C

Open Quantum Systems

This appendix is dedicated to study of a system's interaction with its environment, which we label as an external *reservoir*. Here, we are describing a coupling between a small system and a large "bath" system, such as a continuum of modes of the electromagnetic field. Typically, however, one is only concerned with the time evolution of the small system and only wishes to describe the effects of the bath on the system. This results, under the Weisskopf-Wigner approximation (see [98, Chapter 15]), in an irreversible decay of the populations of non-stable states. Therefore, information contained in the system can be lost to its environment which motivates the labeling of an "open system." We first present the derivation of the Lindblad form of the quantum master equation. Then, we introduce the "quantum jumps" picture which is both a convenient numerical tool, as well as a picture that provides considerable insight into the way a system behaves during a single experiment.

C.1 Quantum Master Equation in Lindblad Form

This section uses results from in [130, Chapter 4, §5] and follows its presentation. The goal is find the equations of motion of the system alone, after taking a partial trace over the reservoir states:

$$\hat{\rho}(t) \equiv \hat{\rho}_S(t) = \mathrm{Tr}_B[\hat{\rho}_{SB}(t)]. \tag{C.1}$$

We first use the density matrix of a mixed ensemble,

$$\hat{\rho}(t) = \sum_j w_j \left|\psi^{(j)}\middle\rangle\middle\langle\psi^{(j)}\right|, \tag{C.2}$$

along with the Schrödinger equation Eq. (2.2) to derive the unitary time evolution of the density matrix in the Schrödinger equation:

$$\begin{aligned} i\hbar\frac{\partial\hat{\rho}}{\partial t} &= \sum_j w_j \left[\left(\partial_t \left|\psi^{(j)}\right\rangle\right)\left\langle\psi^{(j)}\right| + \left|\psi^{(j)}\right\rangle\left(\partial_t\left\langle\psi^{(j)}\right|\right)\right] \\ &= \sum_j w_j \left(\hat{H}\left|\psi^{(j)}\middle\rangle\middle\langle\psi^{(j)}\right| - \left|\psi^{(j)}\middle\rangle\middle\langle\psi^{(j)}\right|\hat{H}\right) = \left[\hat{H}, \hat{\rho}\right], \end{aligned} \tag{C.3}$$

which is reminiscent of the Heisenberg equation of motion Eq. (B.5), but with the opposite sign. For a typical quantum system, the density matrix that undergoes the unitary, reversible dynamics is the composite density matrix of both the system and the environment,

$$\frac{\partial\hat{\rho}_{SB}}{\partial t} = \frac{1}{i\hbar}\left[\hat{H}_{\text{tot}}, \hat{\rho}_{SB}\right], \tag{C.4}$$

where S denotes the system, B denotes the bath, and $\hat{H}_{\text{tot}}$ is the total Hamiltonian:

$$\hat{H}_{\text{tot}} = \hat{H}_S + \hat{H}_B + \hat{H}_{SB}. \tag{C.5}$$

To rotate out the fast dynamics of the uncoupled subsystems, we move into an interaction picture defined by

$$\hat{H}_0 = \hat{H}_S + \hat{H}_B, \tag{C.6}$$

so that

$$\frac{\partial\tilde{\hat{\rho}}_{SB}}{\partial t} = \frac{1}{i\hbar}\left[\tilde{\hat{H}}_{SB}, \tilde{\hat{\rho}}_{SB}\right]. \tag{C.7}$$

Formally integrating for a time Δt,

$$\tilde{\hat{\rho}}_{SB}(t+\Delta t) = \tilde{\hat{\rho}}_{SB}(t) + \frac{1}{i\hbar}\int_t^{t+\Delta t}\left[\tilde{\hat{H}}_{SB}(t'), \tilde{\hat{\rho}}_{SB}(t')\right]dt', \tag{C.8}$$

and then using this equation in an iterative manner, we find

$$\begin{aligned} \Delta\tilde{\hat{\rho}}_{SB}(t) &= \tilde{\hat{\rho}}_{SB}(t+\Delta t) - \tilde{\hat{\rho}}_{SB}(t) \\ &= \frac{1}{i\hbar}\int_t^{t+\Delta t} dt'\left[\tilde{\hat{H}}_{SB}(t'), \tilde{\hat{\rho}}_{SB}(t')\right] - \frac{1}{\hbar^2}\int_t^{t+\Delta t} dt'\int_t^{t'} dt''\left[\tilde{\hat{H}}_{SB}(t'), \left[\tilde{\hat{H}}_{SB}(t''), \tilde{\hat{\rho}}_{SB}(t'')\right]\right]. \end{aligned} \tag{C.9}$$

We now take a partial trace over the reservoir degrees of freedom to derive the time evolution of the reduced density matrix,

$$\mathit{\Delta}\tilde{\hat{\rho}}(t) \equiv \mathit{\Delta}\tilde{\hat{\rho}}_S(t) = \mathrm{Tr}_B\left[\mathit{\Delta}\tilde{\hat{\rho}}_{SB}(t)\right]. \tag{C.10}$$

Furthermore, we make the *Born approximation*,

$$\tilde{\hat{\rho}}_{SB}(t) \approx \tilde{\hat{\rho}}(t) \otimes \tilde{\hat{\rho}}_B, \tag{C.11}$$

where we have assumed a stationary state of the reservoir $\tilde{\hat{\rho}}_B(t) = \tilde{\hat{\rho}}_B$, so that

$$\mathrm{Tr}_B\left[\tilde{\hat{H}}_{SB}(t'), \tilde{\hat{\rho}}_B\right] = 0 \longrightarrow \mathrm{Tr}_B\left[\tilde{\hat{H}}_{SB}(t'), \tilde{\hat{\rho}}_{SB}(t)\right] = 0. \tag{C.12}$$

This approximation is a statement that the reservoir is large and that its coupling to the system is weak [130, Chapter 4, §5], and Eq. (C.9) reduces to

$$\mathit{\Delta}\tilde{\hat{\rho}}(t) \approx -\frac{1}{\hbar^2}\int_t^{t+\mathit{\Delta}t} dt' \int_t^{t'} dt''\, \mathrm{Tr}_B\left[\tilde{\hat{H}}_{SB}(t'), \left[\tilde{\hat{H}}_{SB}(t''), \tilde{\hat{\rho}}_{SB}(t'')\right]\right]. \tag{C.13}$$

We now assume that the evolution of the density operator only depends on $\tilde{\hat{\rho}}(t)$ and not its past history. This is the *Markov approximation*,

$$\tilde{\hat{\rho}}(t'') = \tilde{\hat{\rho}}(t), \tag{C.14}$$

and the *Born-Markov approximation* can now be written as

$$\tilde{\hat{\rho}}_{SB}(t'') \approx \tilde{\hat{\rho}}(t) \otimes \tilde{\hat{\rho}}_B. \tag{C.15}$$

One further approximation is that the interaction Hamiltonian can be written as a product of system and reservoir operators,

$$\tilde{\hat{H}}_{SB} = \hbar \sum_j \tilde{\hat{C}}_j \tilde{\hat{R}}_j, \tag{C.16}$$

where $\tilde{\hat{C}}_j$ and $\tilde{\hat{R}}_j$ are operators in the system and reservoir subspaces, respectively, that need not be Hermitian. When the operators on the right-hand side are non-Hermitian, such that $\tilde{\hat{H}}_{SB} = \tilde{\hat{C}}\tilde{\hat{R}}^\dagger + \tilde{\hat{C}}^\dagger\tilde{\hat{R}}$, there can be exchange of quantized energy between the system and reservoir. This thus represents dissipation from a system to a reservoir, such as spontaneous emission.

Using these approximations and changing variables, $\tau \equiv t' - t''$, Eq. (C.13) becomes

$$\begin{aligned}\varDelta\tilde{\hat{\rho}}(t) \approx -\int_0^\infty d\tau \int_t^{t+\varDelta t} dt' \Big(&\left[\tilde{\hat{C}}_i(t')\tilde{\hat{C}}_j(t'-\tau)\tilde{\hat{\rho}}(t) - \tilde{\hat{C}}_j(t'-\tau)\tilde{\hat{\rho}}(t)\tilde{\hat{C}}_i(t')\right] G\left[\tilde{\hat{R}}_i\tilde{\hat{R}}_j\right](\tau) \\ &+ \left[\tilde{\hat{\rho}}(t)\tilde{\hat{C}}_j(t'-\tau)\tilde{\hat{C}}_i(t') - \tilde{\hat{C}}_i(t')\tilde{\hat{\rho}}(t)\tilde{\hat{C}}_j(t'-\tau)\right] G\left[\tilde{\hat{R}}_j\tilde{\hat{R}}_i\right](-\tau)\Big),\end{aligned} \tag{C.17}$$

where the reservoir correlation function is

$$G\left[\tilde{\hat{R}}_i\tilde{\hat{R}}_j\right](\tau) = \mathrm{Tr}_B\left[\tilde{\hat{R}}_i(t')\tilde{\hat{R}}_j(t'-\tau)\tilde{\hat{\rho}}_B\right] = \langle\tilde{\hat{R}}_i(t')\tilde{\hat{R}}_j(t'-\tau)\rangle_B = \langle\tilde{\hat{R}}_i(\tau)\tilde{\hat{R}}_j(0)\rangle_B, \tag{C.18}$$

and we have used Eq. (2.32). Assuming that $\tilde{\hat{H}}_{SB}$ is Hermitian, we take the limit $\varDelta t \to 0$ so that this reduces to [121, Chapter 4, §5]

$$\begin{aligned}\frac{\partial\hat{\rho}(t)}{\partial t} = \frac{1}{i\hbar}\left[\hat{H}_S, \hat{\rho}(t)\right] + \sum_j \Big(&\left[\hat{C}_j\hat{\rho}(t)\hat{C}_j^\dagger - \hat{C}_j^\dagger\hat{C}_j\hat{\rho}(t)\right]\int_0^\infty d\tau e^{-i\omega_j\tau}\langle\tilde{\hat{R}}_j^\dagger(\tau)\tilde{\hat{R}}_j(0)\rangle_B \\ &+ \left[\hat{C}_j\hat{\rho}(t)\hat{C}_j^\dagger - \hat{\rho}(t)\hat{C}_j^\dagger\hat{C}_j\right]\int_0^\infty d\tau e^{i\omega_j\tau}\langle\tilde{\hat{R}}_j^\dagger(0)\tilde{\hat{R}}_j(\tau)\rangle_B\Big)\end{aligned} \tag{C.19}$$

where we have transformed out of the interaction picture and assumed

$$\tilde{\hat{C}}_j(t) = e^{\frac{i\hat{H}_S t}{\hbar}}\hat{C}_j e^{\frac{-i\hat{H}_S t}{\hbar}} = \hat{C}_j e^{i\omega_j t}. \tag{C.20}$$

Defining

$$\omega_j^+ = \int_0^\infty d\tau e^{-i\omega_j\tau}\langle\tilde{\hat{R}}_j^\dagger(\tau)\tilde{\hat{R}}_j(0)\rangle_B, \tag{C.21}$$

we now separate the density matrix time evolution into real and imaginary parts:

$$\frac{\partial\hat{\rho}(t)}{\partial t} = \frac{1}{i\hbar}\left[\hat{H}_S, \hat{\rho}(t)\right] + \sum_j 2\,\mathrm{Re}\left[\omega_j^+\right]\left(\hat{C}_j\hat{\rho}(t)\hat{C}_j^\dagger - \frac{1}{2}\{\hat{C}_j^\dagger\hat{C}_j, \hat{\rho}(t)\}\right) - i\sum_j \mathrm{Im}\left[\omega_j^+\right]\left[\hat{C}_j^\dagger\hat{C}_j, \hat{\rho}(t)\right]. \tag{C.22}$$

The last term is an effective Hamiltonian term generated by the reservoir interaction, called the *generalized Lamb shift*, so that the Hamiltonian becomes

$$\hat{H} = \hat{H}_S + \hbar\sum_j \mathrm{Im}\left[\omega_j^+\right]\hat{C}_j^\dagger\hat{C}_j. \tag{C.23}$$

We now associate the non-commutator term with the irreversible dynamics of the system by defining the Lindblad superoperator [82]:

$$\hat{\mathcal{L}}(\hat{\rho}) = \sum_j \varGamma_j\hat{\mathcal{D}}[\hat{C}_j]\hat{\rho} = \sum_j \varGamma_j\left(\hat{C}_j\hat{\rho}\hat{C}_j^\dagger - \frac{1}{2}\{\hat{C}_j^\dagger\hat{C}_j, \hat{\rho}\}\right). \tag{C.24}$$

The $\hat{C}_j$ are called the system's jump operators and the decay rate of the j^{th} jump operator is given by $\mathit{\Gamma}_j \equiv 2\,\mathrm{Re}\left[\omega_j^+\right]$. These effective decay channels, in general, cause non-unitary dynamics of the system, and we therefore have captured the system's coupling to the reservoir in an effective master equation of an open quantum system:

$$\frac{\partial \hat{\rho}}{\partial t} = \frac{1}{i\hbar}\left[\hat{H}, \hat{\rho}\right] + \hat{\mathcal{L}}(\hat{\rho}). \tag{C.25}$$

C.2 Monte Carlo Wave Functions

This section is dedicated to the method of Monte Carlo wave functions to study open quantum systems. This involves unraveling the master equation into trajectories based on, for example, stochastic simulation of spontaneously emitted photons. I follow the presentation in [98, Chapter 15, §4]. As hinted at in Chapters 4 and 5, there is a useful connection between the quantum jumps picture presented here and the quantum theory of measurement.

We rewrite the quantum master equation Eq. (C.25) in terms of a non-Hermitian effective Hamiltonian,

$$\hat{H}_{\text{eff}} \equiv \hat{H} - \frac{i\hbar}{2}\sum_k \hat{C}_k^\dagger \hat{C}_k, \tag{C.26}$$

and a "jump" superoperator,

$$\hat{\mathcal{L}}_{\text{jump}}\left(\hat{\rho}\right) = \sum_k \hat{C}_k \hat{\rho} \hat{C}_k^\dagger, \tag{C.27}$$

so that

$$\frac{\partial \hat{\rho}}{\partial t} = \frac{1}{i\hbar}\left(\hat{H}_{\text{eff}}\hat{\rho} - \hat{\rho}\hat{H}_{\text{eff}}^\dagger\right) + \hat{\mathcal{L}}_{\text{jump}}\left(\hat{\rho}\right). \tag{C.28}$$

We now reintroduce a state vector description of the system often referred to as the *quantum jumps* picture. However, the spontaneity of the dissipative effects of the system resulting from Eq. (C.27) cause the evolution to no longer be Schödinger-like, nor deterministic. Instead, the method of Monte Carlo wave functions evolves pure states of the system under Schrödinger-like evolution governed by Eq. (C.26) with random quantum jumps, and then takes a statistical average over them in the end. The quantum jumps picture is therefore intrinsically stochastic.

Plugging the general form of a mixed state's density matrix,

$$\hat{\rho} = \sum_j w_j \left|\psi_j\middle\rangle\middle\langle\psi_j\right| , \tag{C.29}$$

into the master equation in the form of Eq. (C.28) results in

$$\sum_j w_j \left[\left(\partial_t \left|\psi_j\right\rangle\right) \left\langle\psi_j\right| + \left|\psi_j\right\rangle \left(\partial_t \left\langle\psi_j\right|\right) = \frac{1}{i\hbar} \left(\hat{H}_{\text{eff}} \left|\psi_j\middle\rangle\middle\langle\psi_j\right| - \left|\psi_j\middle\rangle\middle\langle\psi_j\right| \hat{H}_{\text{eff}}^{\dagger} \right) + \sum_k \hat{C}_k \left|\psi_j\middle\rangle\middle\langle\psi_j\right| \hat{C}_k^{\dagger} \right] . \tag{C.30}$$

We restict our discussion to a single state ket $|\psi\rangle$ in the mixture and note that the first term on the right-hand side is a the Schrödinger-like evolution with a non-Hermitian Hamiltonian:

$$i\hbar\partial_t \left|\psi\right\rangle = \hat{H}_{\text{eff}} \left|\psi\right\rangle . \tag{C.31}$$

However, the second term results in a discontinuous evolution in which the state is incoherently projected onto another state:

$$\left|\psi\right\rangle \to \left|\Psi_k\right\rangle = \hat{C}_k \left|\psi\right\rangle , \tag{C.32}$$

which motivates the labeling of a "jump" superoperator in the effective Liouvillian.

We now evolve Eq. (C.31) for a short time δt,

$$\left|\tilde{\psi}(t+\delta t)\right\rangle = \left(1 - \frac{i\hat{H}_{\text{eff}}}{\hbar}\right) \left|\psi(t)\right\rangle , \tag{C.33}$$

such that the state ket no longer remains normalized:

$$\left|\tilde{\psi}(t+\delta t)\middle\rangle\middle\langle\tilde{\psi}(t+\delta t)\right| = \left\langle\psi(t)\right| \left(1 + \frac{i\hat{H}_{\text{eff}}^{\dagger}}{\hbar}\right) \left(1 - \frac{i\hat{H}_{\text{eff}}}{\hbar}\right) \left|\psi(t)\right\rangle = 1 - \delta P, \tag{C.34}$$

where δP is the "missing norm,"

$$\delta P = \frac{i}{\hbar}\delta t \left\langle\psi(t)\right| \hat{H}_{\text{eff}} - \hat{H}_{\text{eff}}^{\dagger} \left|\psi(t)\right\rangle = \delta t \sum_k \left\langle\psi(t)\right| \hat{C}_k^{\dagger}\hat{C}_k \left|\psi(t)\right\rangle \equiv \sum_k \delta P_k. \tag{C.35}$$

The full master equation Eq. (C.28) preserves the norm of the density matrix, so the missing norm must be a result from the quantum jumps portion $\hat{\mathcal{L}}_{\text{jump}}$ that projects the system into state $|\Psi_k\rangle$ with probability δP_k.

We now must determine whether of not a jump occurred in time δt. This is achieved numerically by choosing a random number $0 \leq r \leq 1$ and comparing its value to δP. If $r > \delta P$, we say that no jump occurred, normalize the state vector

$$|\psi(t+\delta t)\rangle = \frac{\left|\tilde{\psi}(t+\delta t)\right\rangle}{\left|\left|\tilde{\psi}(t+\delta t)\right\rangle\right|}, \tag{C.36}$$

and now proceed with the next integration step. However, if $r \leq \delta P$, we say a jump occurred and project the state vector onto the new normalized state

$$|\psi(t+\delta t)\rangle = \frac{|\Psi_k\rangle}{||\Psi_k\rangle|} = \sqrt{\frac{\delta t}{\delta P_k}}\,|\Psi_k\rangle \tag{C.37}$$

with probability $\delta P_k/\delta P$. This state is then the initial condition for the next integration step.

This procedure is then repeated for many integration steps which yields a possible time evolution of the initial state, as shown in Fig. C.1. This is what is meant by a *quantum trajectory.* Each run results in a different result, so the trajectories are averaged over at the end of the simulation. In the limit that the number of trajectories n_{trj} becomes large $n_{\mathrm{trj}} \to \infty$, we recover the results that would occur under the evolution of the density matrix. The advantage of the Monte Carlo wave function approach is in simulations that in involve a large number of states N, as the state vector scale as N, while the density matrix scaling is N^2.

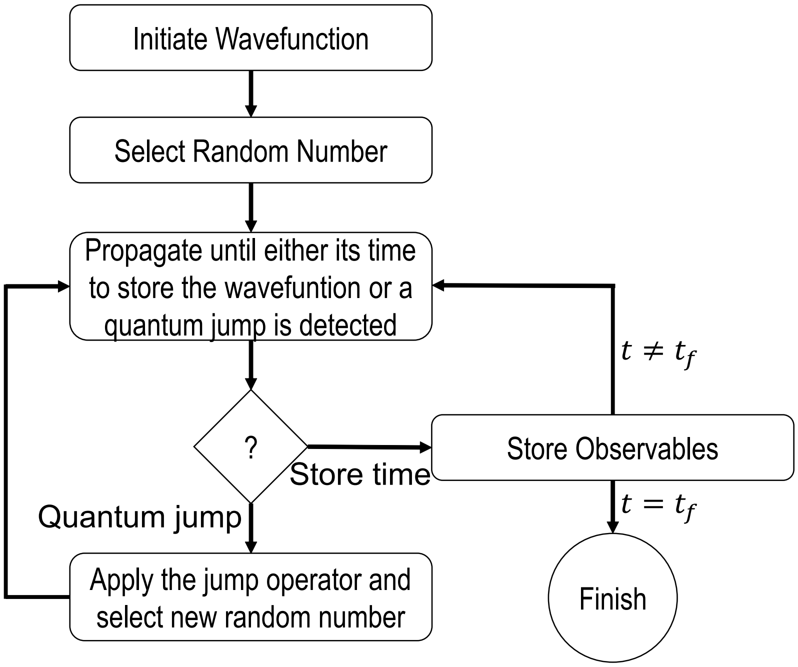

Figure C.1: Algorithm for implementing the Monte Carlo wave function formalism into our simulations of open quantum systems.